

Destructive and Ultrasonic Characterization of Adhesive Joint Durability Using Open-faced Specimens

by

Abduljaleel Kadiri Moidu

A thesis submitted in conformity with the requirements
of the degree of Doctor of Philosophy
Graduate Department of Mechanical and Industrial Engineering
University of Toronto

© Copyright by Abduljaleel Kadiri Moidu 1998



National Library
of Canada

Acquisitions and
Bibliographic Services

395 Wellington Street
Ottawa ON K1A 0N4
Canada

Bibliothèque nationale
du Canada

Acquisitions et
services bibliographiques

395, rue Wellington
Ottawa ON K1A 0N4
Canada

Your file Votre référence

Our file Notre référence

The author has granted a non-exclusive licence allowing the National Library of Canada to reproduce, loan, distribute or sell copies of this thesis in microform, paper or electronic formats.

The author retains ownership of the copyright in this thesis. Neither the thesis nor substantial extracts from it may be printed or otherwise reproduced without the author's permission.

L'auteur a accordé une licence non exclusive permettant à la Bibliothèque nationale du Canada de reproduire, prêter, distribuer ou vendre des copies de cette thèse sous la forme de microfiche/film, de reproduction sur papier ou sur format électronique.

L'auteur conserve la propriété du droit d'auteur qui protège cette thèse. Ni la thèse ni des extraits substantiels de celle-ci ne doivent être imprimés ou autrement reproduits sans son autorisation.

0-612-35256-0

Abstract

Destructive and Ultrasonic Characterization of Adhesive Joint Durability Using Open-faced Specimens

Doctor of Philosophy 1998

Abduljaleel Kadiri Moidu

Department of Mechanical and Industrial Engineering

University of Toronto

A major concern in the use of adhesive joints is their durability when exposed to a moist environment. This thesis investigated the durability of two typical commercial adhesives, Permabond E04 and Hysol EA9346, using the peel test and ultrasonic reflection measurements, employing a novel open-faced specimen. The new specimen geometry overcame the drawbacks of the conventional closed adhesive sandwich, resulting in accelerated degradation in a uniform manner. In addition, it facilitated the testing of the joint in a wet (along with the absorbed water) and dry (after drying out the absorbed water) condition.

An analytical approach was developed and experimentally verified, to predict the adherend plastic dissipation in the peel test, allowing the determination of the critical fracture energy, G_c , from peel data. The model was used to calculate G_c values for the two adhesive systems as a function of the duration of exposure to water at $67^\circ C$. The durability studies showed that for the E04 adhesive, the peeling should be performed in a dry state to assess interfacial weakening, whereas for the EA9346 adhesive, both wet and dry tests revealed interfacial weakening. Failure analysis showed that the degradation for the E04 adhesive was associated with the formation of micro-defects at the interface.

Durability of the two adhesive systems was characterized ultrasonically using open-faced

specimens. It was found that ultrasound can detect the interfacial degradation of the E04 adhesive, but did not show any significant change in response with degradation of the EA9346 adhesive. Measured values of normal-incidence, longitudinal and shear reflection coefficients were in good agreement with a spring model of the interfacial region for the E04 adhesive, enabling the determination of the spring constants as a function of degradation. An oblique-incidence shear-wave measurement system was developed for the inspection of the interfacial region, and implemented using a novel transducer. An efficient angular spectrum approach was developed to model the oblique measurement system, and the experiments were in good agreement with theory.

Dedicated to my late Mother

Acknowledgments

First and foremost, I thank my thesis supervisors, Dr. Jan Spelt and Dr. Anthony Sinclair, for their guidance and support throughout the course of this work. Without a doubt, the past five years have been the greatest learning experience of my life; Jan and Tony played significant roles in that.

I can not possibly thank my wife, Sabeena, for all the sacrifices she made during my Ph.D. My little girl, Fatima, was always there to entertain me during difficult times. I am also indebted to my extended family for their constant encouragement in my pursuit of knowledge.

Thanks are also due to all my colleagues and friends who made my stay here thoroughly fruitful and enjoyable. Each one of you helped me, one way or another, and I will always remember that. I specially thank Safavi, from whom I learned a great deal.

I acknowledge Dexter Aerospace Corporation who supplied the adhesive samples used in this thesis. I am also obliged to the staff in the machine shop, who built most of the fixtures used in this work. Last, but not least, I am grateful to the University of Toronto, and the Manufacturing Research Corporation of Ontario for their financial support.

Contents

Abstract	ii
Acknowledgments	v
Contents	vi
List of Tables	x
List of Figures	xi
Nomenclature	xviii
1 Introduction	1
1.1 Motivation	2
1.2 Thesis objectives	3
1.3 Thesis organization	4
2 Background	5
2.1 Fundamentals of adhesive joints	5
2.1.1 Adhesion	5
2.1.2 Adherend surface preparation	6
2.1.3 The interfacial region	6
2.2 Durability of adhesive joints	7
2.2.1 Water uptake	7
2.2.2 Effects of water	8
2.3 Destructive testing: the peel test	10
2.4 Ultrasonic NDE of adhesive joints	13
2.4.1 Introduction	13
2.4.2 Ultrasonic Methods for the NDE of the interfacial region	14
2.4.3 Characterization of interfacial weakening due to water	17

2.4.4 Theory of wave propagation in adhesive joints	18
2.4.4.1 Plane-harmonic wave theory	18
2.4.4.2 Finite-beam theory.	21
2.4.4.3 Models for the interfacial region	22
3 Analysis of the Peel Test	25
3.1 Energy balance in steady-state peeling	25
3.2 Adherend plastic dissipation in steady-state peeling.	26
3.3 Moment-curvature relations for a bi-linear material	28
3.4 Analysis of the detached part of the flexible adherend	32
3.5 Analysis of the attached part of the adherend	33
3.6 Numerical results.	41
3.7 Experimental validation of the model.	45
3.7.1 The peel data.	45
3.7.2 Results and discussion	47
4 Ultrasonic Nondestructive Evaluation: Theoretical Aspects	51
4.1 Plane-wave reflection coefficients of the interfacial region	51
4.1.1 Normal incidence	51
4.1.2 Oblique incidence	55
4.2 Oblique-incidence, focused wave measurement system.	57
4.2.1 Measurement system	57
4.2.2 Angular spectrum model for the measurement system.	58
4.2.2.1 Emitted field	59
4.2.2.2 Reflected field	60
4.2.2.3 Signal spectrum at the receiver	62
4.2.2.4 Normalization spectrum	63
4.2.2.5 Time domain echoes	64

4.2.2.6 Attenuation	64
4.2.3 Numerical implementation	65
4.2.4 Numerical simulations	66
4.2.4.1 Comparison of resolved and multi-layered approaches	66
4.2.4.2 Focused-beam interaction with the interfacial region	68
4.2.4.3 Sensitivity to adhesive and adherend properties	70
5 Experimental Methods	73
5.1 Durability experiments	73
5.1.1 The open-faced specimen	73
5.1.2 Materials and specimen preparation	74
5.1.2.1 Materials	74
5.1.2.2 Specimen preparation	75
5.1.3 Aging: wet and dry specimens	75
5.2 Destructive testing	76
5.2.1 Peel tests	76
5.2.2 Failure surface analysis	77
5.2.3 Tensile tests	77
5.3 Ultrasonic experiments	78
5.3.1 Normal-incidence shear reflection coefficient	78
5.3.1.1 Principle	78
5.3.1.2 Implementation	80
5.3.2 Normal-incidence longitudinal reflection coefficient	81
5.3.3 Oblique incidence measurements	82
5.3.3.1 Transducer design and construction	82
5.3.3.2 Experimental set up	84
6 Results and Discussion	87
6.1 Water diffusion studies	87

6.2 Destructive test results	90
6.2.1 Two-part adhesive system (AA1100-O - Permabond E04)	90
6.2.2 One-part adhesive system (AA1100-O - Hysol EA9346)	96
6.3 Ultrasonic Test Results	100
6.3.1 Two-part system (AA1100-O alloy - Permabond E04 adhesive).....	100
6.3.1.1 Normal-incidence measurements.....	100
6.3.1.2 Oblique-incidence shear wave measurements.....	108
6.3.2 One-part system	113
6.3.2.1 Normal-incidence shear wave measurements	113
7 Conclusions and Recommendations	115
7.1 Conclusions.....	115
7.1.1 Peel analysis	115
7.1.2 Open-faced specimen for the assessment of durability	116
7.1.3 Ultrasonic NDE of interfacial degradation.....	116
7.2 Contributions.....	117
7.3 Recommendations for future work	118
References	120
A Governing Equations for the Attached Adherend	130
B Oblique Reflection and Transmission Coefficients	133
B.1 Reflection and transmission coefficients of the interfacial region	133
B.2 Transmission coefficients at the front-wall	135
C Water Diffusion Equations	137

List of Tables

Table 3.1	Analysis of data set I	48
Table 3.2	Analysis of data set II	49
Table 4.1	Material properties used in the simulations	53
Table 6.1	Tensile test results for the two-part (Permabond E04) system in dry state .	92
Table 6.2	Material properties used in the calculations	103
Table 6.3	Spring constants for various levels of degradation for the two-part (Permabond E04) adhesive system	103
Table 6.4	95% confidence intervals for the spring constants for the two-part (Permabond E04) adhesive system	106

List of Figures

Figure 2.1:	Schematic of the adhesive/adherend interfacial region	7
Figure 2.2:	Moisture diffusion in a closed adhesive sandwich	10
Figure 2.3:	Configuration of a typical peel test	11
Figure 2.4:	Ultrasonic methods for interfacial characterization, involving, (a) the entire adherend-adhesive-adherend sandwich, (b) the adhesive layer, (c) the interfacial region. The multiple echoes are not shown for the sake of clarity.	15
Figure 2.5:	Schematic of plane-wave interaction with an adhesive joint.	20
Figure 3.1	(a) Steady-state peel configuration, (b) Corresponding moment-curvature diagram	27
Figure 3.2	Bi-linear stress-strain diagram	28
Figure 3.3	Stress distribution of the adherend cross-section, (a) elastic loading, (b) plastic loading, (c) elastic unloading, (d) reverse plastic loading	30
Figure 3.4	Linear approximation to the M-K relation for elastic-plastic loading	34
Figure 3.5	Free body diagram of a differential element on the attached part of the flexible adherend.	37
Figure 3.6	Effect of adherend properties on plastic dissipation: W_{ext}/G_c versus G_c for adherends of different thickness and yield stress; the joint parameters used are: $f = 90^\circ$, $E_a = 2.5$ GPa and $t_a = 0.4$ mm.	42
Figure 3.7	Existence of a critical adherend thickness: W_{ext}/G_c versus h for various values of G and s_y ; the joint parameters used are: $f = 90^\circ$, $E_a = 2.5$ GPa and $t_a = 0.4$ mm.	43

Figure 3.8	Effect of adhesive properties on plastic dissipation: W_{ext}/G_c versus G_c for various values of the normal adhesive foundation constant (l_{sads}); the joint parameters used are: $f = 90^\circ$, $\sigma_y = 300$ MPa and $h = 0.3$ mm.	44
Figure 3.9	Effect of peel angle on plastic dissipation: W_{ext}/G_c versus f ; the joint parameters used are: $\sigma_y = 250$ MPa, $h = 0.5$ mm, $E_a = 2.5$ GPa and $t_a = 0.4$ mm and $G_c = 1000$ J/m ²	45
Figure 3.10	Stress-Strain diagrams; (a) AA1100-O alloy, (b) AA3004-H19 alloy, (c) AA1100-H16 alloy, (d) Hysol EA9346 adhesive	46
Figure 4.1:	Schematic of a plane wave normally incident at the interfacial region; ‘L’ represents longitudinal wave and ‘S’ represents shear wave.	52
Figure 4.2:	Normal-incidence shear-wave reflection coefficient spectra for various values of the tangential spring constant, K_t	53
Figure 4.3:	Normal-incidence reflection coefficient versus spring constant; (a) shear wave, (b) longitudinal wave.	54
Figure 4.4:	Schematic of the oblique-incidence, shear wave reflection from the interfacial region.	55
Figure 4.5:	Oblique shear reflection coefficient versus angle of incidence for various values of the spring constants. The ratio of normal to tangential spring constant, K_n/K_t , is fixed at 4.	56
Figure 4.6:	Oblique incidence, focused ultrasonic measurement system; (a) Front-wall focused configuration, (b) A configuration where the probe-pair is moved down to receive interfacial reflections.	58
Figure 4.7:	Predicted time domain echoes when the shear-shear (SS) reflection is focused at the interfacial region, using, (a) the new resolved approach, and (b) the conventional multi-layered approach. A perfect interface was assumed in the calculations.	67

Figure 4.8: Normalized amplitude spectra of shear-shear (SS) reflection from the interfacial region for various values of the spring constants, at, (a) focused position, $d = 4.5$ mm, (b) de-focused position, $d = 6.0$ mm. It has been assumed that the ratio, K_n/K_t , is fixed at 4.0.....	69
Figure 4.9: Effect of a 10% change in the adhesive longitudinal wave velocity on the amplitude spectrum of SS reflection at focused position.	71
Figure 4.10: Effect of a 1% change in the adherend shear wave velocity on the amplitude spectrum of the SS reflection, at (a) focused position ($d = 4.5$ mm) and (b) De-focused position ($d = 6.0$ mm).	72
Figure 5.1: Schematic of moisture diffusion into, (a) the traditional geometry, and (b) the open-faced geometry.....	73
Figure 5.2: Schematic of the specimens for, (a) peel tests, (b) ultrasonic tests, and, (c) tensile tests and moisture diffusion studies.	74
Figure 5.3: Secondary bonding of the open-faced peel specimen	76
Figure 5.4: Peel test apparatus	77
Figure 5.5: Typical peel trace for a fresh specimen	78
Figure 5.6: Measurement of the plane wave reflection coefficient of normal shear waves: configuration for (a) open-faced specimen, and (b) free plate.	79
Figure 5.7: Experimental set-up for the measurement of plane-wave reflection coefficient of normal shear waves	80
Figure 5.8: Measurement of the plane-wave reflection coefficient of normal longitudinal waves; (a) open-faced joint, (b) free-plate.	82
Figure 5.9: Pattern etched on the PVDF film.	83
Figure 5.10: Construction of the oblique-incidence transducer	84

Figure 5.11: Typical signal recorded by the oblique-incidence transducer when focused on an aluminum reflector; (a) time-domain echo, and (b) corresponding frequency spectrum.	85
Figure 5.12: Schematic of the experimental set-up for oblique-incidence measurements.	86
Figure 6.1: Moisture diffusion curve for the two-part (Permabond E04) system; t is the time of exposure, and $h = 0.518$ mm is the adhesive thickness. Each data point corresponds to the average of ten specimens.	88
Figure 6.2: Moisture diffusion curve for the one-part (Hysol EA9346) system; t is the time of exposure, and $h = 0.578$ mm, is the adhesive thickness. Diffusion coefficient, D , is determined from Fick's model. Each data point corresponds to the average of six points.	88
Figure 6.3: Calculated moisture diffusion curve for open-faced joint of the Hysol EA 9346 system. The adhesive thickness was 0.6 mm.	89
Figure 6.4: Peel force vs. exposure time for two-part (Permabond E04) wet case. The error bars represent one standard deviation each on both sides of the mean value. The curve is a quadratic fit ($r^2 = 0.81$).	91
Figure 6.5: Peel force vs. exposure time for two-part (Permabond E04) dry case. The error bars represent one standard deviation each on both sides of the mean value. The curve is a quadratic fit ($r^2 = 0.76$).	91
Figure 6.6: Tensile test results for cast two-part adhesive (Permabond E04) tested in three conditions: (i) freshly cured (ii) immersed for 100 days and then tested wet, (iii) immersed for 100 days and then tested dry.	92
Figure 6.7: Critical fracture energy vs. exposure time for the two-part dry case (peel data of Fig. 6.5). The error bars represent one standard deviation each on both sides of the mean value. The curve is a quadratic fit ($r^2 = 0.72$)	93
Figure 6.8: SEM micrographs of a fresh specimen of the two-part adhesive at magnifications; (a) 35 times, (b) 500 times.	94

Figure 6.9: SEM micrographs of a degraded specimen (376 days) of the two-part adhesive at magnifications; (a) 35 times, (b) 500 times	94
Figure 6.10: X-ray spectrum at, (a) a micro-defect site, and (b) a defect-free site of the specimen in Fig. 6.9.	95
Figure 6.11: Peel force vs. exposure time for the one-part (Hysol EA9346) adhesive, both in wet and dry conditions. The error bars represent one standard deviation each on both sides of the mean value. The curves are quadratic fits ($r^2 = 0.95$ for dry and $r^2 = 0.99$ for wet).	97
Figure 6.12: Tensile test results for cast one-part adhesive (Hysol EA9346) tested in three conditions: i) freshly cured, ii) immersed for 100 days and then tested wet, iii) immersed for 100 days and then tested dry.	97
Figure 6.13: Fracture energy vs. exposure time for one-part wet and dry cases (peel data of Fig. 6.11). The error bars represent one standard deviation each on both sides of the mean value. The curves are quadratic fit ($r^2 = 0.97$ for dry and $r^2 = 0.99$ for wet).	98
Figure 6.14: SEM micrographs of (a) a fresh specimen, and (b) a degraded (60 days) specimen of the one-part adhesive system (Hysol EA9346).	99
Figure 6.15: Measured normal shear-wave reflection coefficient spectra of the interfacial region, corresponding to various levels of degradation of the two-part (Permabond E04) system; 'M' indicates months of degradation.	101
Figure 6.16: Measured reflection coefficients at 15 MHz of normal-incidence shear waves, as a function of duration of exposure for the two-part (Permabond E04) system. The error bars correspond to one standard deviation each on both sides of the mean value.	101
Figure 6.17: Measured normal longitudinal-wave reflection coefficient spectra of the interfacial region, corresponding to various levels of degradation of the two-part (Permabond E04) system; 'M' indicates months of degradation.	102

- Figure 6.18: Measured reflection coefficients at 20 MHz of normal-incidence longitudinal waves, as a function of duration of exposure for the two-part (Permabond E04) system. The error bars correspond to one standard deviation each on both sides of the mean value. 102
- Figure 6.19: Comparison of theoretical and experimental reflection coefficient spectra of normal-incidence shear waves for the two-part (Permabond E04) system; (a) fresh, (b) 2-month, (c) 8-month, (d) 10-month, (e) 12-month and (f) 15.5-month exposure levels. 104
- Figure 6.20: Comparison of theoretical and experimental reflection coefficient spectra of normal-incidence longitudinal waves for the two-part (Permabond E04) system; (a) fresh, (b) 2-month, (c) 8-month, (d) 10-month, (e) 12-month and (f) 15.5-month exposure levels. 105
- Figure 6.21: Comparison of theory and experiments for the 15.5-month data of the two-part system (Permabond E04). The dashed lines are calculated spectra corresponding to two different values of adhesive density (1360 and 1100 kg/m³), and the solid line is the experimental spectrum. 108
- Figure 6.22: Measured oblique-incidence shear-shear (SS) reflection spectra for the two-part (Permabond E04) system at various levels of degradation. The shear wave was focused ($d = 4.5$ mm) at the interfacial region, and normalized with respect to the front-wall signal; 'M' indicates months of exposure. 109
- Figure 6.23: Comparison of theory and experiments for obliquely incident shear waves (SS) under focused condition, for different levels of degradation of the two-part (Permabond E04) system; (a) Fresh, (b) 10 months, (c) 12 months, (d) 15.5 months. The solid line is experimental and the dashed line is theoretical. ... 110
- Figure 6.24: Oblique-incidence SS reflection spectra for various levels of degradation under the de-focused ($d = 6.0$ mm) condition; the solid lines are measured spectra and the line with symbol is the predicted spectrum for the fresh case. 112

Figure 6.25: Normal-incidence shear wave reflection coefficients at 15 MHz for the one-part (Hysol EA9346) adhesive system as a function of duration of exposure. The error bars correspond to one standard deviation on each side of the mean value. . 113

Figure A.1 Free body diagram of a differential element on the attached part of the flexible adherend. 130

Figure B.2: Schematic of oblique-incidence shear wave reflection from the interfacial region. 134

Figure C.3: Schematic of water diffusion into, (a) cast adhesive sample, (b) open-faced specimen. 138

Nomenclature

A	Constant
A_e	Angular spectrum of the emitter
A_r	Angular spectrum of the receiver
a	Aperture of the active elements of the oblique-incidence transducer
a_4, a_5	Constants
B	Constant
b	Width of the peel specimen
b_4, b_5	Constants
C	Moisture concentration
C_0	Moisture concentration at sample surface
C_1 to C_7	Integration constants
c_l	Longitudinal wave velocity
c_t	Shear wave velocity
D	Diffusion coefficient
D_{ll}	Longitudinal-longitudinal transmission coefficient of the adhesive/ adherend interfacial region
D_{ls}	Longitudinal-shear transmission coefficient of the adhesive/adherend interfacial region.
D_{sl}	Shear-longitudinal transmission coefficient of the adhesive/adherend interfacial region
D_{ss}	Shear-shear transmission coefficient of the adhesive/adherend interfacial region
d	Vertical distance by which the probe-pair is moved down from a front-wall focused position

d_4, d_5	Constants
E_a	Young's modulus of the adhesive
E	Young's modulus of the adherend
E_p	Slope of the strain hardening part of the stress-strain diagram
E_s	Secant modulus of the adherend
F	Focal length
F_e	Focal length of the emitter
F_r	Focal length of the receiver
f	Frequency in Hz
G_c	Critical fracture energy
G_I	Mode I component of G_c
G_{II}	Mode II component of G_c
H	Transfer function of the transducer
h	Adherend thickness
I_f	Signal spectrum from the buffer rod - free-plate interface
I_s	Signal spectrum from the buffer rod - specimen interface
J_f	Signal spectrum from the backwall of the free-plate
J_s	Signal spectrum from the backwall of the adherend of the open-faced joint
K	Curvature of the centroidal axis of the adherend
K_e	Elastic limit curvature of the adherend
K_0	Curvature at the root of the adherend
K_n	Normal spring constant

K_t	Tangential spring constant
k	Normalized curvature
k_C	Normalized curvature at point C in the moment-curvature diagram
k_1	Normalized curvature at elastic limit in the approximate m-k diagram
k_i	Imaginary part of the wave number (attenuation coefficient)
k_l	Longitudinal wave number
\vec{k}_l	Longitudinal wave vector
k_o	Normalized curvature at the root of the adherend
k_r	Real part of the wave number
k_s	Shear wave number
\vec{k}_s	Shear wave vector
k_w	Wave number
L_h	Absolute value of the horizontal position of the probe-pair in specimen coordinates
L_v	Absolute value of the vertical position of the probe-pair in specimen coordinates
l	Distance between the center of the active element, and the center of the entire film in the oblique-incidence transducer
M	Moment per unit width
M_p	Ultimate plastic moment per unit width
M_t	Amount of water absorbed at time, t
M_∞	Equilibrium water content
m	Normalized moment

m_o	Normalized moment at the root of the adherend
m_1	Normalized moment at elastic limit in the approximate m-k diagram
N_f	Ratio of the back-wall to the front-wall spectrum of the free-plate
N_s	Ratio of the back-wall to the front-wall spectrum of the open-faced joint
O	Objective function in the least-square optimization
P_e	Pupil function of the emitter
P_r	Pupil function of the receiver
P	Peel force
Q	A matrix in terms of ultrasonic and material parameters
Q_1 to Q_5 . .	Parameters in terms of adherend properties and foundation constants
q	A vector in terms of ultrasonic and material parameters
R_{ex}	Experimental reflection coefficient spectra
R_{fw}	Reflection coefficient at the water/adherend interface
R_{ll}	Longitudinal-longitudinal reflection coefficient of the interfacial region
R_{ls}	Longitudinal-shear reflection coefficient of the interfacial region
R_{sl}	Shear-longitudinal reflection coefficient of the interfacial region
R_{ss}	Shear-shear reflection coefficient of the interfacial region
R_{th}	Theoretical reflection coefficient spectra
R_1	Reflection coefficient at the transducer - buffer rod interface
R_2	Reflection coefficient at the buffer rod - adherend interface
S	Signal spectrum captured by the receiver
S_{fw}	Front-wall signal spectrum

T_{ll}	Longitudinal-longitudinal transmission coefficient at water-adherend interface
T_{ls}	Longitudinal-shear transmission coefficient at water-adherend interface
T'_{ll}	Longitudinal-longitudinal transmission coefficient at adherend-water interface
T'_{sl}	Shear-longitudinal transmission coefficient at adherend-water interface
T	Axial force; Temperature
t	Time
t_a	Adhesive thickness
\vec{u}	Displacement vector
u	Horizontal deflection of attached part of the adherend; x-component of the displacement vector at the adhesive/adherend interfacial region.
v	Vertical deflection of attached part of the adherend
V	Shear force
w	z-component of the displacement vector at the adhesive/adherend interfacial region
W_{ext}	External work per unit area
W_{et}	Stored elastic energy per unit area in tension
W_{pt}	Energy per unit area dissipated plastically in tension
W_{pb}	Energy per unit area dissipated plastically in bending
X	A parameter defined for diffraction and attenuation effects in the buffer rod and the adherend
\vec{x}	Position vector
x_e	x - coordinate attached to the emitter
x_r	x - coordinate attached to the receiver

x x - coordinate attached to the specimen
 y Distance of a point on the adherend cross-section from the neutral axis,
 y - coordinate common to the emitter, receiver and the specimen.
 \bar{y} Normalized distance of a point on the adherend cross-section from the
neutral axis
 \bar{y}_1 \bar{y} corresponding to the elastic-plastic interface in plastic bending
 \bar{y}_2 \bar{y} corresponding to the elastic-plastic interface in reverse plastic bending
 Z Specific acoustic impedance
 z_e z - coordinate attached to the emitter
 z_r z - coordinate attached to the receiver
 z z - coordinate attached to the specimen

Greek Symbols

α Vertical wave number of longitudinal waves in the specimen coordinates
 α_e Vertical wave number of longitudinal waves in the emitter coordinates.
 α_w Vertical wave number in water, in specimen coordinates
 β Vertical wave number of shear waves in the specimen coordinates
 Γ_{ll} A parameter defined for longitudinal-longitudinal reflection
 Γ_{ls} A parameter defined for longitudinal-shear, and shear-longitudinal
reflections
 Γ_{ss} A parameter defined for shear-shear reflection
 γ A parameter in terms of k_o and δ
 δ Ratio of E_p to E
 ε Strain

$\bar{\varepsilon}$	Normalized strain
ε_e	Effective strain
ε_t	Tensile strain in the detached part of the flexible adherend
ε_t^{adh}	Average transverse strain in the adherend
ε_t^{ads}	Average transverse strain in the adhesive
ε_y	Adherend yield strain
ζ	y -component of the horizontal wave number
η_r	Real part of the complex root of the characteristic equation of the differential equation governing the foundation shear stress
η_i	Imaginary part of the complex root of the characteristic equation of the differential equation governing the foundation shear stress
θ	Nominal incident angle
θ_a	Aperture angle of the active elements in the oblique-incidence transducer
θ_{cr}	First critical angle at the water-adherend interface
θ_o	Root rotation of the adherend
κ	Real root of the characteristic equation of the differential equation governing the foundation shear stress
λ	Lame's constant
λ_σ	Total normal foundation constant
λ_τ	Total shear foundation constant
λ_σ^{adh}	Adherend normal foundation constant
λ_τ^{adh}	Adherend shear foundation constant

λ_{σ}^{ads}	Adhesive normal foundation constant
λ_{τ}^{ads}	Adhesive shear foundation constant
μ	Modulus of rigidity
μ_a	Modulus of rigidity of the adhesive
ν	Poisson ratio
ξ	x -component of the horizontal wave number in specimen coordinates
ξ_e	x -component of the horizontal wave number in emitter coordinates
ρ	Density
ρ_w	Density of water
σ	Normal (axial) stress
$\bar{\sigma}$	Normalized axial stress
σ_y	Adherend yield stress
σ_{yy}	Foundation normal (transverse) stress in the peel joint
σ_{zz}	Normal stress at the adhesive/adherend interfacial region
ζ	Slope of the elastic-plastic loading section of the approximate m-k diagram
τ_{xz}	Shear stress at the adhesive/adherend interfacial region
τ_{xy}	Foundation shear stress in the peel joint
ϕ	Longitudinal wave potential; Peel angle
ϕ_e	Emitted longitudinal wave potential
ϕ_r	Reflected longitudinal wave potential
φ	Phase angle
χ	A parameter in terms of k_s and ξ

$\vec{\psi}$ Vector potential for shear waves

ψ_y y - component of the vector potential

ω Circular frequency

Acronym

CAA Chromic acid anodization

EDS Energy dispersive spectroscopy

FPL Forest products laboratory

LL Longitudinal-longitudinal

LS. Longitudinal-shear

NDE. Nondestructive evaluation

PAA Phosphoric acid anodization

PVDF Polyvinylidene fluoride

SEM Scanning electron microscopy

SL. Shear-longitudinal

SS. Shear-Shear

XPS X-ray photoelectron spectroscopy

Structural adhesive joining is becoming increasingly popular as an alternative to traditional methods of fastening materials such as welding and riveting. Adhesive joints reduce stress concentrations, transmitting loads more uniformly from one member to another, thereby reducing the weight and improving the fatigue resistance of the finished component. Adhesives can be used to join a wide variety of materials such as metals, plastics and composites, and are suitable to join dissimilar materials. Recent developments in adhesive formulations have resulted in adhesives with excellent strength and stiffness properties, providing further impetus to the use of structural adhesives in high-strength applications. In particular, adhesive bonding of aluminum structures has received considerable attention in the aerospace industry and, more recently, in the automotive sector.

A major concern in the use of the adhesives is durability. It is well established that adhesive joints may undergo a progressive, permanent degradation in strength when exposed to certain service environments. Moisture has been found to be one of the most harmful substances which affect the joint strength, and unfortunately the most commonly encountered. A well-prepared, fresh joint fails by fracture within the adhesive layer, a phenomenon termed a *cohesive* failure. However, on prolonged exposure to moist environment, it is found that the locus of failure often shifts to the interface between the adhesive and adherend, and the failure load is significantly lower. This is termed an *adhesive* failure, implying interfacial weakening.

Moisture may enter a joint by diffusion through the adhesive layer (for metal-metal joints). Generally, moisture affects the *cohesive* as well as *adhesive* (interfacial) properties, and may be reversible or irreversible. It is the permanent effects of the moisture on the stability of the interfacial region of an adhesive joint which can reduce the strength drastically.

1.1 Motivation

An understanding of the interfacial degradation of adhesive joints, exposed to a moist environment, is of great practical importance in order to utilize the full potential of adhesive joining technology. The present work is motivated by the following three issues in the interfacial characterization of adhesive joints exposed to a moist environment:

i) *Experimental assessment of durability*: In order to assess the durability of adhesive joints, it is standard practice to expose the joint to a specified environment (typically an elevated humidity/temperature), and record the strength drop as a function of the time of exposure. Although there have been numerous such durability studies, they have suffered from the drawback that the moisture uptake is relatively slow, and the moisture concentration and the level of degradation are spatially nonuniform within the joint. This makes it difficult to study the variables affecting the time-dependant degradation of the joint corresponding to a specific exposure condition. It is also very difficult to isolate the permanent and reversible effects of moisture on the joint. There is a need to develop an alternative durability experimental method.

ii) *Destructive testing*: After exposure to a given environment for a specified duration, the joint strength may be assessed destructively using the peel test for adhesive joints. In a typical peel test, a flexible adherend, which is bonded to a rigid adherend by means of an adhesive, is peeled at a specified angle at constant rate. Compared to other test methods for adhesive joints, the peel test has the advantage that the crack path is very close to the interface between the flexible adherend and the adhesive, which makes it attractive for interfacial characterization.

The steady-state peel force obtained is a measure of the adhesion strength between the adhesive and the adherend. However, there is a great deal of uncertainty regarding the fraction of the work of peeling that is expended in the plastic deformation of the flexible adherend, which undergoes severe bending at the peel front. It is of interest to develop a model for the peel test in order to predict the plastic dissipation in the flexible adherend, thereby enabling the determination of the critical fracture energy from the overall peel energy.

iii) *Nondestructive Testing*: The nondestructive testing of in-service adhesive joints is of great practical importance. Ultrasonic methods have long been identified as the most suitable means for this purpose. They have been successfully implemented to evaluate cohesive properties, and to detect voids, disbonds etc. However, at the present time there does not exist any method to nondestructively assess the interfacial properties of an adhesive joint. It is well known that this is an extremely difficult task because it involves the detection of subtle changes in a very thin region which lies beneath a relatively thick adherend.

Ultrasonic reflection measurements from the adhesive/adherend interfacial region is one of the techniques which has the potential to evaluate the integrity of the interfacial region. However, to date there has been no conclusive evidence for correlations between ultrasonic reflection measurements and level of interfacial degradation in adhesive joints subjected to a moist environment.

1.2 Thesis objectives

This thesis investigated the durability of aluminum-epoxy structural adhesive joints, both destructively and nondestructively, using the peel test and ultrasonic reflection measurements from the adhesive/adherend interfacial region. An important aspect of the present work was the use of an open-faced specimen geometry, thereby overcoming the difficulties associated with traditional geometries. The specific objectives of the thesis were:

- To conduct durability experiments using open-faced specimens, both destructively and nondestructively. Attention was given to both the permanent and reversible effects of moisture.
- To develop an analytical model for predicting the plastic work within the flexible adherend in the peel test, thereby allowing the determination of the critical fracture energy from peel test data. The model was used to analyze the peel durability data.
- To investigate, both theoretically and experimentally, the potential of ultrasonic reflection measurements from the adhesive/adherend interfacial region to detect interfacial weakening.
- To analyze of the peel failure surfaces in order to understand the nature of degradation.

1.3 Thesis organization

The thesis is divided into seven chapters. Chapter 2 discusses the necessary background information and the relevant literature.

In Chapter 3, a theoretical model for the analysis of the peel test is developed. Numerical results are presented to understand the effects of various material properties on the adherend plastic dissipation. Experimental verification of the model is also given.

The theoretical investigation of ultrasonic reflection from the adhesive/adherend interfacial region is the subject of Chapter 4. The reflection characteristics of normal-incidence longitudinal and shear waves are analyzed, using a spring model to describe the interfacial region. An angular spectrum approach is developed to model an oblique-incidence, shear wave measurement system for the examination of the interfacial region of adhesive joints. Numerical simulations are carried out using the model.

Chapter 5 outlines the details of the various experimental methods and procedures employed in the work. The open-faced specimen is introduced, and the various destructive test methods are described. Methods for the measurement of normal shear and longitudinal reflection coefficients of the interfacial region are given. The design and construction of a novel transducer for oblique-incidence measurements is described.

Chapter 6 gives the results and analysis of the destructive and nondestructive evaluation of the durability of two commercial adhesive systems. The critical fracture energies are determined as a function of degradation, from the peel durability data and the model developed in Chapter 3. The interfacial spring constants are determined as a function of degradation, from the normal-incidence ultrasonic measurements. The oblique-incidence ultrasonic measurements are compared with the angular spectrum model developed in Chapter 4.

Finally, Chapter 7 summarizes the conclusions and the major contributions of the present work. Possible topics for future work are also identified.

This chapter gives the necessary background information and reviews the relevant literature. First, a brief review of the fundamentals of adhesive joints will be given, followed by a discussion of their durability. The peel test for adhesive joints will be discussed next. Finally, the various ultrasonic methods and associated theoretical tools for the interfacial characterization of adhesive joints will be reviewed in detail.

2.1 Fundamentals of adhesive joints

2.1.1 Adhesion

The first step in the formation of a strong adhesive joint is the establishment of intimate molecular contact at the interface between the adhesive and the adherends. This requirement is usually referred to as wetting [1]. Good wetting requires that the adhesive be able to flow and spread over the adherend surfaces and be able to displace the air and any contamination. The wetting phenomenon is strongly influenced by the surface thermodynamics of the adherend and adhesive [1]. It is also recognized that adhesion depends on the kinetics of the wetting, which in turn is largely determined by the viscosity of the adhesive during bond formation, and the topography of the adherend surface [1].

Once proper wetting has been achieved between the adhesive and the adherends, then the adhesive is cured, or hardened, so that it can transmit load from one adherend to the other. The mechanisms of adhesion between the adhesive and the adherend are still not fully understood, and many theories are to be found in the literature [1]. Two of these mechanisms are presently believed to be operative in the case of metal-to-metal adhesive joints. First is the *adsorption theory*, which is the most widely accepted theory of adhesion. According to this

theory, materials adhere together because of the interatomic forces acting between the two surfaces; the most common forces are Van Der Waals forces (referred to as secondary bonds). In addition, chemisorption may occur in the form of ionic, covalent and metallic bonds operating across the interface (referred to as primary bonds). A second mechanism, namely, *mechanical interlocking* is also considered to contribute to the measured strength. According to this theory, the adhesive interlocks into the irregularities on the adherend surface, thereby resisting separation.

2.1.2 Adherend surface preparation

The nature of an adherend surface prior to bonding is one of the most important factors which determines the adhesion strength of a joint. The adherend surface should be free from any contamination such as oil, grease etc. For general engineering applications, simple degreasing and roughening of the adherend surface, for example by grit-blasting, may be sufficient [1, 2]. However, for critical situations such as aerospace applications, chemical pretreatment of the adherend surface is required [1, 2] for good initial joint strength as well as durability. Such pretreatment methods produce adherend surfaces which are rough on a micro-scale [1-3]. It is thought that the chemical pretreatments improve the mechanical interlocking and the kinetics of wetting, thereby improving the adhesion [1]. It is also postulated that pretreated joints show higher strength because of the increased energy dissipation effects during fracture [1, 2]

For aluminum adherends, there are three major pretreatment methods available, namely, sulfuric acid etching (also known as the FPL etch procedure, after Forest Products Laboratory), Phosphoric Acid Anodization (PAA) and Chromic Acid Anodization (CAA) [1, 2]. These techniques produce an oxide-layer on the adherend surface, which has varying degrees of rough microscopic features, depending on the specific method of pretreatment [4].

2.1.3 The interfacial region

It is now well accepted that the adhesive/adherend interface is not a plane boundary, but a three dimensional, multilayered structure (Fig. 2.1), that may be denoted as the interfacial

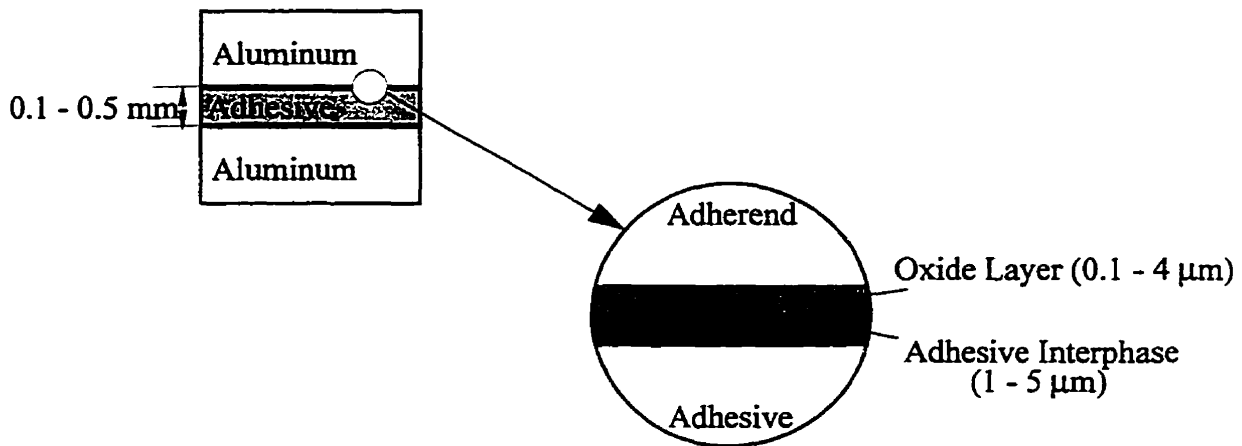


Figure 2.1: Schematic of the adhesive/adherend interfacial region

region. For aluminum-to-aluminum joints, the interfacial region includes an oxide layer, which is $0.1 - 4 \mu\text{m}$ in thickness, depending on the pretreatment method [4]. Recently, there has been evidence [5-8] of an *adhesive interphase* in the vicinity of the oxide layer (Fig. 2.1), with possibly different physical and chemical properties compared to the bulk adherend. This subject is not well understood, and is a subject of active research [8].

2.2 Durability of adhesive joints

A key requirement of a structural adhesive joint is to retain a significant proportion of its initial strength upon exposure to its service environment. Unfortunately, it is well documented that adhesive joints may undergo significant weakening. Water, in liquid or vapor form, has been found to be the most hostile environment for adhesive joints, particularly those featuring metal adherends [1, 2].

2.2.1 Water uptake

Water may enter a joint by diffusion through the exposed edges of the adhesive, transportation along the adhesive/adherend interface, diffusion through the adherend if it is permeable, and by capillary action through cracks and crazes in the adhesive [9]. For most metal-to-metal adhesive joints, it is established that diffusion through the exposed edges of the

adhesive is the major mechanism of water uptake. Several authors, e.g. [9-14], have studied the diffusion characteristic of common adhesives by measuring the mass increase of a thin film of adhesive, exposed to a specified humidity and temperature, as a function of time. In most cases, the water uptake curves showed the characteristics of Fickian diffusion [15], and the diffusion coefficient could be found by fitting a Fickian model to the measured absorption curve. The diffusion coefficient thus measured may be used to predict the water distribution in practical adhesive joints operating in the same environment [11].

2.2.2 Effects of water

Water may affect both cohesive and interfacial properties of a joint, as described below:

(i) Plasticization and swelling of the adhesive: As a result of the water absorption, the glass transition temperature of the adhesive drops, reducing its modulus and strength [2]. This is termed plasticization, and is a reversible phenomenon. One study [16] found that plasticization is a major factor in degradation for certain types of adhesives. It was also found that the plasticization causes the fracture toughness of adhesive joints to increase [1]. The higher glass transition temperature of heat-cured, one-part adhesives makes them less susceptible to plasticization than room-temperature cured two-part adhesives [2].

Another reversible effect of water is the swelling of the adhesive, a phenomenon which introduces stresses into the joint. There have been some investigations of the swelling stresses [9], which concluded that they are unlikely to be a major factor affecting the long-term durability of joints. It was also suggested that adhesive swelling may help to relieve the residual stresses set up in the adhesive layer due to shrinkage while curing [3].

(ii) Hydrolysis, cracks and crazes: The chemical reaction between water and the adhesive (hydrolysis) may alter the mechanical properties of the adhesive. Another permanent effect of water on adhesives is the leaching of unreacted components [9]. The water uptake plot of an adhesive fails to reach equilibrium in the presence of such permanent effects.

Cracking or crazing of the adhesive as a result of prolonged exposure to water is another factor which must be considered when assessing the durability of adhesive joints. This is particularly important for service at elevated or widely fluctuating temperatures [17].

(iii) Interfacial weakening: Although water may affect the cohesive properties of an adhesive, there is a consensus that it is the effects of water on the interfacial properties of the joint which are responsible for its decrease in strength on exposure to water [1]. A well-prepared fresh joint invariably fails cohesively, while the locus of failure of an aged joint is observed to shift to the interfacial region. This suggests that any study aimed at characterizing the environmental degradation of adhesive joints should concentrate on the interfacial region.

The mechanism(s) by which water attacks the interfacial region is not well understood. Several theories have been advanced, but none of them are universally accepted [1-3]. One such theory is that water causes the rupture of secondary bonds across the adhesive/adherend interfacial region, thereby displacing the adhesive [3]. The rupture of the secondary bonds in the presence of water can be predicted from surface thermodynamics [1, 3]. A second theory is that the adhesive interphase (Fig. 2.1) may be more susceptible to hydrolysis than the bulk adhesive [3]. A third proposition is the weakening of the oxide layer in a metallic joint, due to hydration [4]. However, more recent evidence suggests that such hydration may be a post-failure phenomenon [5].

For a given adhesive/adherend system, the rate and extent of interfacial weakening depend on various parameters such as humidity, temperature, duration of exposure, adherend surface preparation and the applied stress. There have been numerous experimental studies, e.g. [16-23], to understand the effects of various parameters on degradation using closed adhesive sandwiches (Fig. 2.2). In such a geometry, the water enters the joint by diffusion through the exposed edges of the adhesive, and hence the water concentration within the joint is nonuniform. This causes the degradation of the interfacial region to proceed in a slow and nonuniform manner, making it difficult to study the interfacial weakening corresponding to a

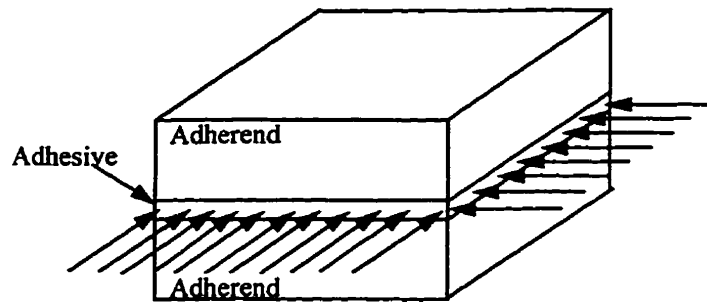


Figure 2.2: Moisture diffusion in a closed adhesive sandwich

specific exposure condition, i.e., humidity and temperature. It is also difficult to isolate the permanent (as opposed to reversible) interfacial effects of water by using this traditional joint geometry. The present work addressed these important issues in the experimental assessment of durability by the use of a specimen geometry that promoted uniform and accelerated degradation. Very recently, after this work began, others [24, 25] have reported similar specimen geometry; however they did not address the time-dependent degradation corresponding to a specific exposure condition, and the effects of wet and dry testing; i.e. testing the joint along with the water absorbed during the environmental conditioning (a “wet” test) or testing it after drying out the absorbed water.

2.3 Destructive testing: the peel test

After exposure to a specific environment for a fixed duration, the durability of a joint is usually assessed by common destructive test methods such as the single or double lap shear test, peel test etc. The peel test (Fig. 2.3) was chosen as the destructive test method for the present work, because the crack path in a peel test is close to the interfacial region and hence it is attractive to characterize the adhesion strength. In fact, for the same reason, the peel test is used widely for the mechanical characterization of adhesion phenomenon in a variety of adhesion applications [2].

There are a variety of peel tests, and the American Society of Testing Materials (ASTM) has issued four different standards [2]. Essentially, they all consist of a flexible adherend,

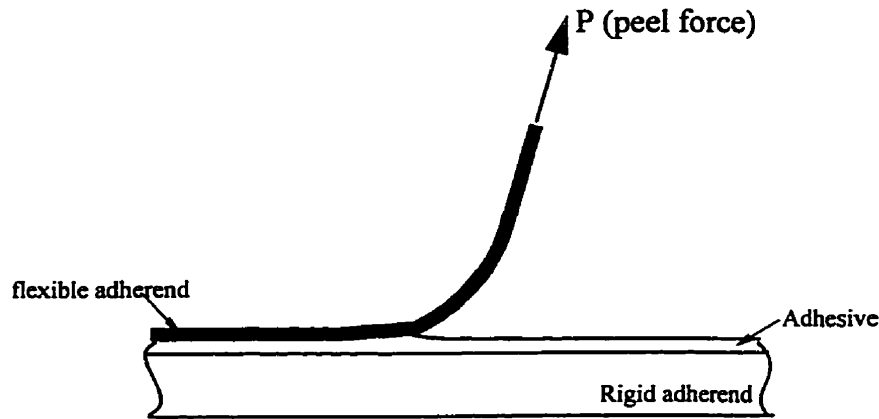


Figure 2.3: Configuration of a typical peel test

which is peeled at a constant angle and rate, from a rigid adherend to which it is bonded using an adhesive (Fig. 2.3). The test reaches a steady-state condition after the initial crack extension, and the steady-state peel force is a measure of the adhesion between the flexible adherend and the adhesive. However, there is a great deal of uncertainty regarding the fraction of the work of peeling that is expended in the plastic deformation of the flexible adherend which undergoes severe bending at the peel front. Without adequate models to account for such plastic dissipation effects, the peel test is at best qualitative.

The classical model for peel analysis attempts to predict the transverse tensile stresses set up in the adhesive layer in terms of the measured peel force and material properties. Following this approach, Spies [26] analyzed elastic peeling by considering the still-attached part of the flexible adherend as an elastic beam on an elastic (Winkler) foundation, and the detached part of the flexible adherend as an elastic beam under large displacement. Several such elastic models have been derived by others [27-33]. A finite element analysis of elastic peeling was presented by Crocombe and Adams [34].

Alternatively, there has been an energy approach to elastic peeling [2, 35], which equates the work done by the test machine (external work) to the work done on the sample, and expresses the peel energy as the difference between the external work and the stored elastic

energy in the flexible adherend. The peel energy includes plastic dissipation in the flexible adherend, the plastic and viscoelastic dissipation in the adhesive, and a surface energy term (work of adhesion or work of cohesion, depending on whether failure is *interfacial* or *cohesive*) [2]. The latter two terms (surface energy and adhesive dissipation) constitute the critical fracture energy, which is a measure of the strength of the joint, while the flexible adherend plastic dissipation is an artifact of the test method. The evaluation of the adherend plastic dissipation is not a trivial task because it depends on several parameters such as the material (adhesive/adherend) properties, peel angle and the fracture energy itself. A useful peel model should estimate the adherend plastic dissipation from knowledge of the peel force, the peel angle and the adhesive/adherend properties.

Early attempts to account for the effects of adherend plasticity, which used elementary beam theory [36, 37], are inadequate to predict the adherend plastic dissipation from peel test data. A finite-element analysis of elasto-plastic peeling was given by Crocombe and Adams [38]. Significant progress in peel analysis was achieved with the development of a large displacement, elastic-plastic pure bending theory for the flexible adherend advanced by Kim and co-workers [39, 40]. They gave an expression for the plastic dissipation in terms of the peel force, the adherend properties, peel angle and the rotation at the root of the flexible adherend. It was shown that the plastic dissipation is strongly influenced by the root rotation; however, it could not be determined from their analysis. Subsequently, Williams [41] analyzed the root rotation in the peel test, following Kanninen's [42] approach to crack-tip rotation in double cantilever beam (DCB) specimens.

Williams [41] assumed the flexible adherend to be elastic at the root, although the elastic-plastic nature of the adherend was taken into account for the detached portion of the adherend using Kim's approach [39]. Also, the effect of adhesive properties on root rotation was neglected. This thesis addresses these two important issues in the prediction of adherend plastic dissipation in the peel test, by developing a theory for an elastic-plastic beam on an elastic foundation. Further, the present work considers an extension of the elastic-plastic pure bending theory [40, 43] to model a bilinear stress-strain behavior of the flexible adherend.

Once the adherend plastic dissipation is evaluated, the determination of the critical fracture energy from the peel energy is straightforward. The peel test is essentially a mixed-mode (mode I and mode II) fracture test [35]. Although the mode-mix effects in elastic peeling have been analyzed [35], there exists no analytical method to estimate the mode ratio for elastic-plastic peeling. The present work addresses this issue as well.

2.4 Ultrasonic NDE of adhesive joints

2.4.1 Introduction

Nondestructive evaluation (NDE) methods for adhesively-bonded structures are of great practical importance. Although many NDE methods have been investigated in the past to inspect adhesively bonded structures, ultrasonic methods have the greatest potential [2]. This is because ultrasonic waves are sensitive not only to defects such as voids, disbonds etc., but also to elastic and viscoelastic properties of the materials involved.

There are three aspects to the nondestructive evaluation (NDE) of adhesive joints; namely, (a) detection of defects such as voids, disbonds (b) evaluation of the cohesive properties of the adhesive, and (c) evaluation of interfacial properties [2]. The first is relatively straightforward, and conventional ultrasonic methods may be readily employed for that purpose [2]. Considerable progress has been made also in the characterization of the cohesive properties of the adhesive [44-46]. Strong correlations have been found between ultrasonic parameters, such as through-thickness resonance frequencies of the joint, and shear strength of the joint. A number of commercial bond testers based on resonance methods are available, such as the Fokker bond tester [2, 44-46]. Such bond testers can also be used to detect defects such as disbonds.

Currently, there exists no reliable method to characterize the interfacial strength of adhesive joints nondestructively [2, 45-47]. This has been acknowledged to be a very challenging problem, since the task here is to detect subtle changes in a very thin interfacial region (of the order of 1 μm) which lies beneath a relatively thick adherend (of the order of 1 mm, Fig. 2.1). The current practice in industry is to guard against interfacial

failure by strict quality control of the surface preparation of the adherend. However, as discussed earlier, adhesive joints are susceptible to interfacial weakening upon exposure to a moist service environment. Lack of NDE techniques to evaluate such degradation limits the potential applications of adhesive joints, despite their many advantages.

It should be mentioned that strength is a *destructive* parameter; hence, the ultrasonic NDE of strength is based on the hypothesis that a decrease in strength is accompanied by physical changes in the interfacial region, such as a change in the local stiffness. The dependance of these changes in the material properties on ultrasonic wave propagation may be analyzed, thus providing a way to evaluate the interfacial strength nondestructively. The correlations between ultrasonically determined interfacial parameters and the destructive strength must necessarily be empirical.

2.4.2 Ultrasonic Methods for the NDE of the interfacial region

There have been many ultrasonic techniques which have been investigated for the characterization of the interface of an adhesive joint. Cawley [47] gave an excellent review of the major techniques. These fall into three basic categories:

(a) Methods involving the adherend-adhesive-adherend sandwich: This category is based on the interaction of ultrasonic waves with the whole adherend-adhesive-adherend sandwich structure (Fig. 2.4a), and involve relatively low frequencies, of the order of 1 MHz. Since the wavelength at these low frequencies are comparable to the total thickness of a typical joint (Fig. 2.1), the reflected longitudinal and shear waves from the various interfaces superimpose each other to generate the various modes of vibration of the sandwich structure.

Lamb (plate) wave techniques fall into this category. When the sandwich structure is obliquely insonified, the Lamb modes, which propagate along the joint, may be generated. The Lamb waves leak energy into the coupling medium as they propagate, allowing the wave propagation characteristics to be measured. Several research groups investigated the variations in the Lamb wave dispersion (phase velocity of the various Lamb modes vs. frequency) curves with changes in the interfacial properties. Guy et al. [48] showed that the dispersion curves are not highly sensitive to perturbations in interfacial properties. Cawley and

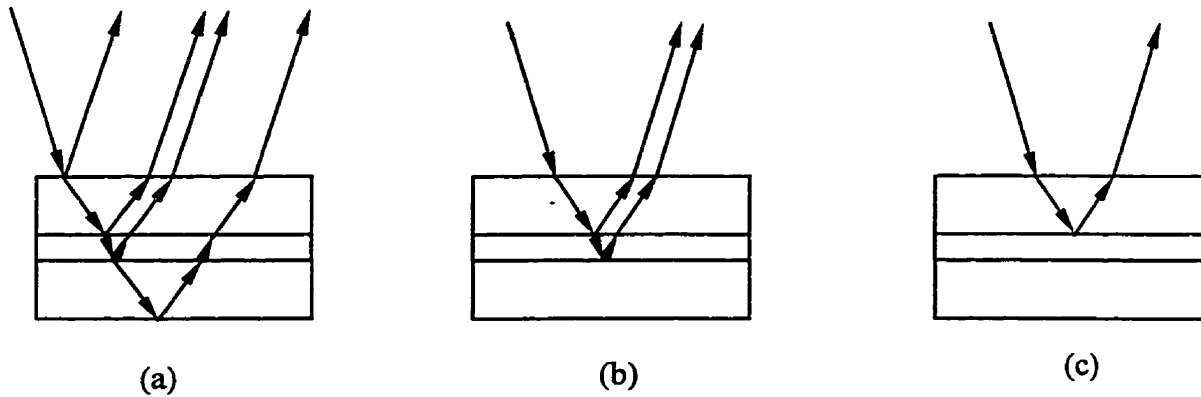


Figure 2.4: Ultrasonic methods for interfacial characterization, involving, (a) the entire adherend-adhesive-adherend sandwich, (b) the adhesive layer, (c) the interfacial region. The multiple echoes are not shown for the sake of clarity.

co-workers [47] have shown that the dispersion curves are primarily sensitive to adherend properties, implying that Lamb waves can not be readily used for interfacial characterization.

Dickstein et al. [49] have investigated the thickness resonances of the sandwich structure along with novel signal processing and pattern recognition methods to evaluate the interfacial region. They were able to classify joints empirically according to their methods of surface preparation using ultrasonic features obtained from signal processing. Levesque et al. [51] have presented a similar technique, which they call as *ultrasonic interferometry*, and report strong sensitivity of the reflection spectra of the sandwich structure to interfacial properties of the joint, both theoretically and experimentally. Thompson and Thompson [50] also reported on the sensitivity of certain thickness vibration modes to the interfacial condition. These results are somewhat surprising since it is widely held that the resonance techniques can indicate only the cohesive properties and gross defects [46].

(b) Guided modes of the adhesive layer: This category of ultrasonic NDE of the interface is based on wave propagation within the adhesive layer, and hence reduces the sensitivity of the results to the adherend properties (Fig. 2.4b). When the adhesive layer is insonified obliquely, the guided modes are formed, for suitable combinations of frequency and adhesive

thickness, due to the superposition of the longitudinal and shear waves reverberating within the adhesive layer. The dispersion characteristics of the guided modes of the adhesive layer depend on the boundary conditions between the adhesive and the adherends. There are two classes in this category, namely, (i) true guided modes of the adhesive layer, i.e., those modes which do not leak back into the adherends, and (ii) leaky guided modes propagating in the adhesive layer.

The true guided modes have been investigated, mostly theoretically, by many authors [52-54], and it has been shown that such modes are sensitive to interfacial properties, in addition to the cohesive properties of the adhesive. However, there are practical difficulties in generating true guided modes of the adhesive layer, since they can not be excited by waves launched from the top adherend. In most engineering structures, ultrasonic waves must be introduced to the bondline via the top adherend from a transducer in contact with the surface or in a liquid medium above the surface.

In contrast, the leaky guided modes of the adhesive layer can be generated readily by waves launched obliquely through the top adherend (Fig. 2.4b). This method requires relatively higher frequency (5-10 MHz) in order to resolve the adhesive echoes from the echoes originating from the outer surfaces of the adherends. Rokhlin and co-workers [55] analyzed this method extensively using theoretical and experimental tools. They found that certain features in the reflection spectrum of the adhesive layer are sensitive to the interfacial condition. Other researchers [56, 57] also investigated this technique. However, the leaky guided modes were shown to be substantially sensitive to the cohesive properties of the adhesive as well [47].

(c) Ultrasonic reflection coefficient of the adhesive/adherend interfacial region: The third major technique for the ultrasonic characterization of the interfacial region is the measurement of its reflection coefficient (Fig. 2.4c). The major advantage of this technique is that the reflection coefficient is primarily sensitive to perturbations in interfacial properties, such as those due to environmental degradation from moisture uptake. Since the echo from the upper surface of the adhesive needs to be resolved from

that originating from the bottom surface, the ultrasonic frequency needs to be much higher for this method than those described earlier; of the order of 25 MHz for a typical adhesive thickness of 0.4 mm. This method was also the natural choice for the present study because it is compatible with the novel specimen geometry selected for the investigation.

Many researchers have investigated the use of reflection coefficient measurements from the interfacial region to characterize its properties. Early investigations used normal-incidence longitudinal waves [58]. However, it was shown that inspection methods which use waves incident obliquely at the interface may be more sensitive to adhesion weakness [59-61]. In particular, it has been theoretically demonstrated that, the reflection mode that is most sensitive to the interfacial condition is the oblique, shear-shear reflection from the interfacial region [59, 60].

2.4.3 Characterization of interfacial weakening due to water

Many of the experiments reported in the literature were carried out on specimens with artificially weakened interface, such as one contaminated with a release agent prior to bonding to create “poor” adhesion. Some authors attempted to discriminate adhesive joints nondestructively according to their different surface pretreatments [49, 51]. There have been few attempts to characterize interfacial weakening as a function of exposure to a moist environment. One of the major objectives of the present work was to ultrasonically characterize the interfacial weakening of adhesive joints on exposure to water.

Early work in the NDE of the interfacial weakening due to moisture attempted to use normally incident ultrasonic compression waves [62]. Dickstein et al. [63] used advanced signal processing techniques to classify joints nondestructively for various levels of moisture content. This work was primarily empirical in nature. Recently Rokhlin and co-workers [64, 66] have investigated environmental degradation of adhesive joints using the leaky guided modes of the adhesive layer. They found correlations between certain features in the frequency spectrum and joint strength as measured by the lap shear test. They also attempted to characterize interfacial degradation by a model of an adhesive joint

with a nonhomogeneous interphase structure [65].

The above works used the traditional joint geometry (Fig. 2.2), which suffers from the drawbacks described in Section 2.2.2, making it impossible to associate nondestructive parameters to a particular level of degradation or water concentration. Also, the research employed ultrasonic methods which have substantial sensitivity to small perturbations in the bulk adhesive properties as well as the interfacial region (methods (a) and (b)). It was noted earlier that water in general affects both cohesive and interfacial properties of a joint. Therefore, there is a degree of uncertainty as to the respective contributions of cohesive and interfacial changes to the perturbations in ultrasonic features; an additional set of experiments may be required to isolate the interfacial effects [66]. The present work tackles these issues by using ultrasonic reflection measurements from the interfacial region, a method of type (c) that is primarily sensitive to interfacial properties, and a new specimen geometry which overcame the difficulties associated with the traditional geometry.

2.4.4 Theory of wave propagation in adhesive joints

2.4.4.1 Plane-harmonic wave theory

The theoretical modelling of ultrasonic plane wave interactions with adhesive joints has received wide attention in the last two decades. General purpose multi-layer modelling tools have been developed using a number of matrix formulations [67]. The matrix methods are quite general, and may be used to model all three major methods for the NDE of adhesive joints described earlier.

The starting point for the modelling of wave propagation in a homogeneous isotropic solid is Navier's equation of motion [69,70] given by, in the absence of body forces,

$$\mu \nabla^2 \vec{u} + (\lambda + \mu) \nabla \nabla \cdot \vec{u} = \rho \frac{\partial^2 \vec{u}}{\partial t^2} \quad (2.1)$$

where λ and μ are the Lamé constants, ρ is the density and \vec{u} is the displacement vector. The displacement field may be decomposed into dilatational and rotational fields by expressing it

as the sum of the gradient of a scalar field, ϕ , and the curl of a vector field $\vec{\psi}$, i.e.,

$$\vec{u} = \nabla\phi + \nabla \times \vec{\psi} \quad (2.2)$$

Combining equations (2.1) and (2.2), the following scalar and vector wave equations describing compression (longitudinal or dilatational) waves and shear (transverse or rotational) waves may be obtained [70]:

$$\nabla^2 \phi = \frac{1}{c_l^2} \frac{\partial^2 \phi}{\partial t^2} \quad (2.3a)$$

$$\nabla^2 \vec{\psi} = \frac{1}{c_t^2} \frac{\partial^2 \vec{\psi}}{\partial t^2} \quad (2.3b)$$

where $c_l = \sqrt{(\lambda + 2\mu)/\rho}$ and $c_t = \sqrt{\mu/\rho}$ are the bulk longitudinal and shear wave velocities in the medium, respectively.

In multi-layered plate problems such as an adhesively-bonded structure, it is usually assumed that the width of the structure is much larger than the ultrasonic wavelength involves, and therefore a two-dimensional (plane strain) analysis is valid [67]. For the plane strain case, the vector wave equation becomes a scalar one, with only the out-of-plane component of the vector potential, ψ_y , being relevant (Fig. 2.5). The plane-harmonic solutions of Eq. 2.3, for compression and shear waves, are:

$$\phi = A e^{i(\vec{k}_l \cdot \vec{x} - \omega t)} \quad \psi_y = B e^{i(\vec{k}_s \cdot \vec{x} - \omega t)} \quad (2.4)$$

where k_l and k_s are the longitudinal and shear wave numbers, respectively, and ω is the circular frequency. The solution for the wave motion in a multi-layered structure is achieved by the superposition of longitudinal and shear bulk waves (Eq. 2.4) in each layer, and the imposition of proper boundary conditions. It is sufficient to consider four waves in each of the

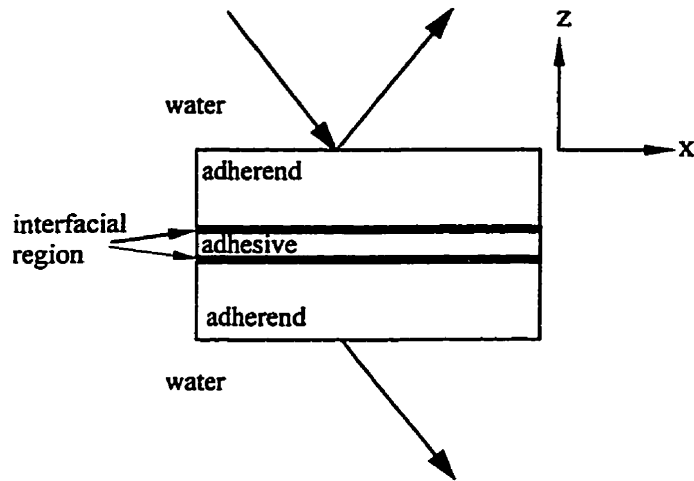


Figure 2.5: Schematic of plane-wave interaction with an adhesive joint

layers, two shear and two longitudinal waves, corresponding to the incident and reflected fields [67].

The most common method to solve the multi-layered problem is the transfer matrix method [67]. The major advantage of the transfer matrix method is relatively small computational effort. However, the method suffers from numerical instability when the ratio of thickness of a layer to the wavelength is much greater than unity. Unfortunately, this situation holds for typical adherend thicknesses and frequencies involved in commercial adhesive joints [67]. Recently Levesque et al. [68] addressed this issue and derived a robust version of the transfer matrix method. An alternative is to use the global matrix method [67], which has been shown to be extremely robust, to calculate the plane wave reflection coefficient from a layered structure. This results in slower computation than the transfer matrix method.

Many of the ultrasonic models [47-60] for adhesive joints used the plane wave theory. For method (a) (Lamb wave and resonance technique) and method (b) (guided modes of adhesive layer), which involve frequency or velocity measurements, the plane wave approximation is

valid provided that the specimens are kept in the far field of the ultrasonic transducers. However, for method (c) (reflection coefficient) this simplification is valid only if the measured reflection spectrum is de-convolved with respect to a reference spectrum to correct for beam divergence and attenuation in the propagating medium [47]. Although this may be achieved in laboratory conditions, such a reference spectrum would not be available for the inspection of industrial adhesive joints. It would be desirable to model the complete measurement system taking into account the detailed structure of the wave field generated by the transmitter, the characteristics of the receiver and the propagation effects in the various media including the coupling medium.

2.4.4.2 Finite-beam theory

In order to model an ultrasonic measurement system, a finite or bounded beam approach based on the angular spectrum or plane-wave decomposition method [71] may be employed. According to the angular spectrum method, a bounded ultrasonic beam may be decomposed into an infinite number of plane waves or angular components centered about the incident angle. This is a powerful tool to deal with bounded beams since the analytical framework for plane waves is well established.

Pialucha and Cawley [61] modelled the diffraction effects originating from the finite size of flat transducers used in the NDE of the interfacial region, using the angular spectrum method. They concluded that a finite beam model is essential to predict the full response of the transducer, and that under certain circumstances the plane wave approximation may be used. In their work, it was necessary to perform an experimental correction on measured signal by means of a reference spectrum.

Most of the commercially available transducers in the higher frequency range (typically > 15 MHz), which is required for the examination of the interfacial region using method (c) (see Section 2.4.2), are manufactured with a focussing lens in order to shorten the near field length. In addition, focused beams make it possible to generate various wave types over a wide range of angles simultaneously inside the adherend. There exists no theoretical studies of the interaction of focused waves with the adhesive/adherend interfacial region in

the literature. The present work models an oblique-incidence immersion measurement system with a focused transmitter and receiver.

2.4.4.3 Models for the interfacial region

It may be recalled that water attacks primarily the interfacial region of an adhesive joint; therefore a physical model of the interfacial region is required, and many approaches have been proposed in the literature for this purpose. These models for the interfacial region may be readily incorporated into the above wave propagation models for adhesive joints.

Wang and Rokhlin [55] modelled the interfacial region as a two-layered structure, consisting of the oxide layer and a weak-boundary layer. The oxide layer was modelled as elastically anisotropic because of its porous structure. They used a weak-boundary layer concept to simulate interfacial weakening, either as a result of degradation or due to improper surface preparation of the adherends. Such layered models of the interfacial region have been used by other investigators as well [47, 60, 74]. A simple isotropic, visco-elastic interlayer with complex dynamic moduli was also considered to model the interfacial region [51, 72].

The major disadvantage of the interlayer model is that very little is known about the nature of the adhesive interphase (or weak boundary layer), and the changes to the adhesive interphase and the oxide layer as a result of environmental degradation. A simple isotropic, elastic interlayer model to describe the adhesive interphase needs four parameters, namely the two elastic constants, density and the thickness. If the oxide layer is also to be included, seven more additional properties are required, namely five elastic constants (for transverse isotropy), the thickness of the oxide and its density [73, 74].

Other researchers have modelled the interfacial region using normal and tangential springs [51, 58, 59, 75]. Very strong springs correspond to perfect interfacial adhesion, while a weakening in adhesion is represented by weak springs. Mathematically, the spring model requires only a minor modification in the boundary conditions. At a perfect interface between two half spaces, the boundary conditions consist of the continuity of normal and shear stresses

and displacements across the interface. In the spring model case (imperfect interface) the boundary conditions are the continuity of the stresses and a discontinuity in the displacements which depends on the spring constants. For the plane strain case:

$$(\sigma_{zz})_1 = (\sigma_{zz})_2 = K_n(w_2 - w_1), \quad (\tau_{xz})_1 = (\tau_{xz})_2 = K_t(u_2 - u_1) \quad (2.5)$$

where w and σ_{zz} are the normal displacement and stress, respectively, u and τ_{xz} are the tangential displacement and stress, respectively, and, K_n and K_t are the normal and the tangential spring constants at the interface, respectively. The subscripts 1 and 2 refer to the adherend and the adhesive respectively.

Wang and Rokhlin [72] have described the physical basis for the spring model. They showed that it is a special case of the layer model, in which the elastic responses of the interlayer are considered and their inertia is neglected. The spring constants are equivalent to the elastic properties of the layer normalized by its thickness, and sometimes are referred to as the specific stiffnesses [51]. It was shown [72] that the spring model is valid in the long wavelength limit, i.e., when the thickness of the interfacial region is much smaller than the wavelength involved. When the oxide layer thickness is negligible (which is the case, for instance, with the FPL surface pretreatment of the adherend) the above condition is usually satisfied because the adhesive interphase is of the order of 1 - 5 μm thick and the typical wavelength is at least one order of magnitude greater in the commercially feasible frequency range of 5 - 30 MHz.

Another situation where the spring model is applicable is the case of a distribution of sub-wavelength defects (defect size, $a \ll \lambda$) at the interface between two solids. Because of the presence of the sub-wavelength defects, the local stiffness at the interface is lowered relative to the bulk solids, a situation which can be described by a spring model. Such a model has been applied to fusion welding and diffusion bonding [76-78], where there is only a partial (intermittent) contact between the materials on a micro-structural level.

The spring model is attractive because it needs only two parameters to characterize the interfacial region. However, there has been no experimental evidence of the validity of the spring model in the case of adhesive joints. The present work investigates the applicability of the spring model to describe the environmental degradation of the interfacial region in adhesive joints.

This chapter presents a theoretical approach to the analysis of the peel test. First, the large displacement, elastic-plastic pure bending theory of the flexible adherend is extended to a bilinear stress-strain response. Second, a new model is developed for the still-attached part of the flexible adherend, treating it as an elastic-plastic beam on an elastic foundation. The prediction of the adherend plastic dissipation is made possible by combining the above two solutions, thereby allowing the determination of the critical fracture energy and mode-ratio from the peel test data. Numerical simulation is carried out to understand the effects of various material parameters on the adherend plastic dissipation. Finally, the model is validated experimentally. The material presented in this chapter has already been published by the author [79, 80].

3.1 Energy balance in steady-state peeling

In a peel test (Fig. 3.1), after the debond begins to propagate, the peel force approaches a steady value for constant peel angle. Under steady-state conditions, the following energy balance may be formulated [43]:

$$G_c = W_{ext} - W_{et} - W_{pt} - W_{pb} \quad (3.1)$$

where G_c is the critical fracture energy, W_{ext} is the external work per unit area, W_{et} is the stored elastic energy per unit area in tension of the flexible adherend (hereafter referred to as the “adherend”), W_{pt} is the energy per unit area dissipated plastically due to tensile deformation of the adherend, and W_{pb} is the energy per unit area dissipated plastically due to

bending of the adherend. The external work per unit area may be calculated from [2]:

$$W_{ext} = \frac{P}{b} (1 + \epsilon_t - \cos \phi) \quad (3.2)$$

where P is the peel force, b is the width of the adherend, ϕ is the peel angle, and ϵ_t is the tensile strain in the detached part of the adherend. In most cases of adhesive bonds, W_{et} and W_{pt} are negligible compared to W_{pb} . The calculation of W_{pb} is not a trivial task because it depends on many variables such as the material (adhesive/adherend) properties, peel angle and the critical fracture energy itself. The prediction of the plastic dissipation due to bending in the adherend (hereafter referred to as the adherend plastic dissipation or simply, the plastic dissipation) is the major objective of the present analysis.

The critical fracture energy, G_c , includes the surface energy term (work of adhesion or work of cohesion, depending on whether the failure locus is *interfacial* or *cohesive*) and the local dissipation ahead of the crack tip due to the plastic and visco-elastic effects. It should also be noted that the peel test constitutes a mixed-mode fracture, and hence G_c may be partitioned into its opening mode (mode I) and sliding mode (mode II) components.

3.2 Adherend plastic dissipation in steady-state peeling

Figures 3.1a and 3.1b show the configuration of the adherend, and the corresponding moment-curvature (M-K) diagram, respectively, in a steady-state peel test [39, 40]. The adherend ceases to be elastic at point A, where it attains the elastic-limit curvature and yield moment. From point A to point B, the adherend is plastically deformed and reaches the maximum curvature at the root, B. It undergoes elastic unloading during B-C, and reverse plastic loading during C-D to straighten the adherend. It is convenient to normalize the moment and curvature with respect to the collapse moment and elastic limit curvature, respectively [39, 81]:

$$m = M/M_p; \quad k = K/K_e \quad (3.3)$$

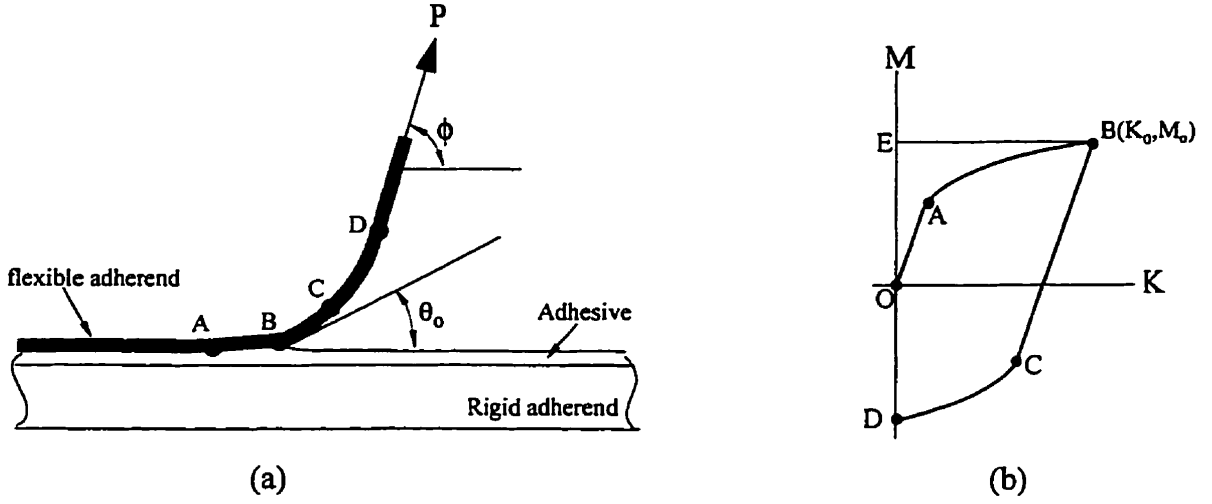


Figure 3.1 (a) Steady-state peel configuration, (b) Corresponding moment-curvature diagram

where M and K are the moment per unit width and the curvature of the centroidal axis of the adherend cross-section, respectively, at any position along the adherend, and, M_p and K_e are the collapse moment per unit width and elastic limit curvature, respectively, given by:

$$M_p = \sigma_y h^2 / 4; \quad K_e = 2\sigma_y / Eh \quad (3.4)$$

where σ_y is the adherend yield stress, h is the adherend thickness, and E is the Young's modulus of the adherend.

The adherend plastic dissipation is given by the area enclosed by the M-K diagram (Fig. 3.1b), i.e., the area enclosed by O-A-B-C-D-O, given by:

$$W_{pb} = M_p K_e \int_{OABCD} m(k) dk \quad (3.5)$$

It should be noted that the above equation includes the residual elastic bending energy also. To evaluate the above expression, the m-k relations for the various stages of deformation (Fig. 3.1b) are derived below for a linear strain-hardening (bilinear) material.

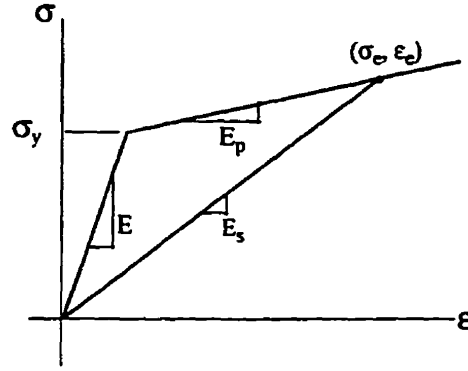


Figure 3.2 Bi-linear stress-strain diagram

3.3 Moment-curvature relations for a bi-linear material

In this section the moment-curvature relationships for a bilinear stress-strain behaviour of the flexible adherend is newly derived. It may be noted that, Kinloch et al [43] considered the bilinear case; however, their derivation led to some misleading restrictions on the solution.

The uniaxial stress-strain relation for a bilinear material (Fig. 3.2) may be expressed as:

$$\begin{aligned}\sigma &= E\varepsilon & \varepsilon < \varepsilon_y \\ &= f(\varepsilon) = \sigma_y + E_p(\varepsilon - \varepsilon_y) & \varepsilon > \varepsilon_y\end{aligned}\quad (3.6a)$$

where σ_y and ε_y are the yield stress and yield strain of the adherend, respectively, E is the Young's modulus of the adherend, and E_p is the slope of the strain-hardening part of the stress-strain diagram (Fig. 3.2). It is convenient to normalize Eq. 3.6a as follows:

$$\begin{aligned}\bar{\sigma} &= \bar{\varepsilon} & \bar{\varepsilon} < 1 \\ &= f(\bar{\varepsilon}) = (1 - \delta) + \delta\bar{\varepsilon} & \bar{\varepsilon} > 1\end{aligned}\quad (3.6b)$$

where $\bar{\sigma} = \sigma/\sigma_y$, $\bar{\varepsilon} = \varepsilon/\varepsilon_y$ and $\delta = E_p/E$.

With the usual assumption of beam theory that plane sections remain plane and normal to the centroidal axis, the axial strain at any point on the adherend cross-section is given by:

$$\bar{\varepsilon} = k\bar{y} \quad (3.7)$$

where $\bar{y} = y/(h/2)$, y being the distance of a point from the neutral axis.

The normalized moment-curvature relationship may be obtained from the following equation, in conjunction with Eq. 3.6b and Eq. 3.7 and by knowing the stress distribution of the adherend cross-section (Fig. 3.3):

$$m = 2 \int \bar{\sigma} \bar{y} d\bar{y} \quad (3.8)$$

Elastic loading (Fig. 3.3a): During segment O-A (Fig. 3.1), elastic loading of the adherend takes place, and the well-known moment-curvature relation for elastic bending may be obtained from Eq. 3.8 as:

$$m_{OA}(k) = \frac{2}{3}k \quad (3.9)$$

Plastic loading (Fig. 3.3b): During segment A-B, plastic loading of the adherend occurs, and the stress distribution is given by:

$$\begin{aligned} \bar{\sigma} &= \bar{\varepsilon} = k\bar{y} & 0 < \bar{y} < \bar{y}_1 \\ &= f(\bar{\varepsilon}) = f(k\bar{y}) & \bar{y}_1 < \bar{y} < 1 \end{aligned} \quad (3.10)$$

where f is given by Eq. 3.6b, and \bar{y}_1 is the elastic-plastic interface (Fig. 3.3b), which can be obtained from Eq. 3.10, using the condition that $\bar{\sigma} = 1$ at the elastic-plastic interface, giving $\bar{y}_1 = 1/k$. Therefore, using Eq. 3.8, we get:

$$m_{AB}(k) = (1 - \delta) \left(1 - \frac{1}{3k^2} \right) + \frac{2\delta k}{3} \quad (3.11)$$

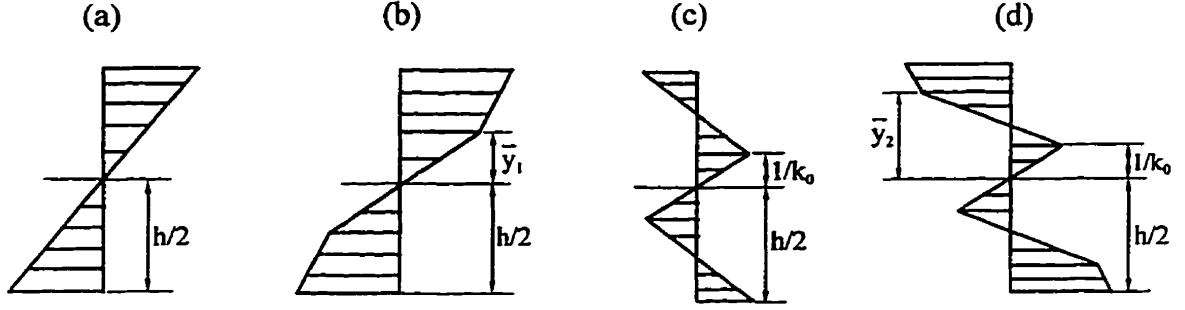


Figure 3.3 Stress distribution of the adherend cross-section, (a) elastic loading, (b) plastic loading, (c) elastic unloading, (d) reverse plastic loading

Elastic unloading (Fig. 3.4c): During segment B-C, elastic unloading of the adherend occurs and the stress distribution is given by:

$$\begin{aligned}\bar{\sigma} &= \bar{\epsilon} = k\bar{y} & 0 < \bar{y} < 1/k_o \\ &= f(k\bar{y}) - (k_o - k)\bar{y} & 1/k_o < \bar{y} < 1\end{aligned}\quad (3.12)$$

where k_o is the normalized root curvature. Using Eq. 3.8, the following moment-curvature relation for the elastic unloading stage may be obtained:

$$m_{BC}(k) = m_o - \frac{2}{3}(k_o - k) \quad (3.13)$$

where m_o is the normalized moment at the root of the adherend, given by (see Eq. 3.11):

$$m_o = (1 - \delta) \left(1 - \frac{1}{3k_o^2} \right) + \frac{2\delta k_o}{3} \quad (3.14)$$

Reverse plastic loading (Fig. 3.3d): The stress distribution during the reverse plastic bending stage, C-D in Fig. 3.1, can be shown to be.

$$\begin{aligned}
 \bar{\sigma} &= k\bar{y} & 0 < \bar{y} < 1/k_o \\
 &= f(k_o\bar{y}) - (k_o - k)\bar{y} & 1/k_o < \bar{y} < \bar{y}_2 \\
 &= -f(k\bar{y}) & \bar{y}_2 \leq \bar{y} \leq 1
 \end{aligned} \tag{3.15}$$

where \bar{y}_2 is the new elastic-plastic interface in reverse plastic bending (Fig. 3.3d), which may be found from the condition that the stress at \bar{y}_2 is equal to the yield stress, i.e., from Eq. 3.15:

$$f(k_o\bar{y}_2) - (k_o - k)\bar{y}_2 = -1 \tag{3.16}$$

For a bilinear material, using Eq. 3.6b, we get:

$$\bar{y}_2 = \frac{2 - \delta}{k_o(1 - \delta) - k} \tag{3.17}$$

Finally, from Eq. 3.8, we get the moment-curvature relation for the reverse plastic bending stage as:

$$m_{CD}(k) = (1 - \delta) \left(2\bar{y}_2^2 - 1 - \frac{1}{3k_o^2} - \frac{2}{3}k_o\bar{y}_2^3 \right) - \frac{2}{3}\delta k + \frac{2}{3}(1 + \delta)k\bar{y}_2^3 \tag{3.18}$$

The curvature at point C, needed to calculate the area under the M-K diagram (Fig. 3.1b), can be found from Eq. 3.16 using the condition that the stress on the outer fiber ($\bar{y} = 1$) at C is equal to the yield stress, i.e.,

$$f(k_o) - (k_o - k_C) = -1 \tag{3.19}$$

For a bilinear material, using Eq. 3.6b, we get

$$k_C = k_o - 2 - \delta(k_o - 1) \tag{3.20}$$

It is also noteworthy, that under certain conditions the points C and D coincide, i.e., the

reverse plastic bending stage is absent. The value of the root curvature, k_o , at which this happens may be found from Eq. 3.20 with $k_C = 0$, i.e.,

$$k_o \leq 1 + \frac{1}{1-\delta} \quad (3.21)$$

By substituting the m-k relations (Eqs. 3.9, 3.11, 3.13 and 3.18) into Eq. 3.5, the following expression for the adherend plastic dissipation may be obtained:

$$\frac{W_{pb}}{M_p K_e} = (1-\delta) \left(\frac{k_o^2}{3} + \frac{2}{3k_o} - 1 \right) \quad \text{for } 1 < k_o \leq 1 + \frac{1}{1-\delta} \quad (3.22a)$$

$$\begin{aligned} \frac{W_{pb}}{M_p K_e} = & (1-\delta) \left(k_o + \frac{1}{3k_o} - 1 \right) + (k_C - k_o) \left(m_o + \frac{k_C - k_o}{3} \right) \\ & - k_C (\delta - 1) \left(1 + \frac{1}{3k_o^2} \right) + \frac{\alpha (k_C^2 + k_o^2)}{3} - (2-\delta) (1-\delta) \left(2 - \frac{k_o}{3} \right) \\ & - \frac{k_C}{3} (1+\delta) (2-\delta) - (2-\delta)^2 \left(\frac{(4-\delta^2)}{3k_o(1-\delta)} - \frac{(1+\delta)}{3} - \frac{2}{k_o} \right) \\ & \text{for } k_o \geq 1 + \frac{1}{1-\delta} \end{aligned} \quad (3.22b)$$

3.4 Analysis of the detached part of the flexible adherend

Using the large-displacement, elastic-plastic theory [39, 43], the following expression may be derived for the detached part of the flexible adherend:

$$\frac{P}{b} (1 - \cos(\phi - \theta_o)) = M_p K_e \left[m_o k_o + \int_{k_o}^{k_c} m_{BC}(k) dk + \int_{k_c}^0 m_{CD}(k) dk \right] \quad (3.23)$$

where θ_o is the rotation at the root, B , of the adherend (Fig. 3.1a). Substitution of the new m-k relations for a bilinear material (Eqs. 3.9, 3.11 3.13 and 3.18) into the above equation yields:

$$\frac{P}{bM_p K_e} (1 - \cos(\phi - \theta_o)) = \frac{k_o^2}{3} \quad \text{for } 1 < k_o \leq 1 + \frac{1}{1 - \delta} \quad (3.24a)$$

$$\begin{aligned} \frac{P}{bM_p K_e} (1 - \cos(\phi - \theta_o)) = & k_C m_o + \frac{(k_C - k_o)^2}{3} - k_C (\delta - 1) \left(1 + \frac{1}{3k_o^2} \right) + \frac{\delta k_C^2}{3} \\ & - (2 - \delta)(1 - \delta) \left(2 - \frac{k_o}{3} \right) - \frac{k_C}{3} (1 + \delta)(2 - \delta) \\ & - (2 - \delta)^2 \left(\frac{(4 - \delta^2)}{3k_o(1 - \delta)} - \frac{(1 + \delta)}{3} - \frac{2}{k_o} \right) \\ & \text{for } k_o \geq 1 + \frac{1}{1 - \delta} \end{aligned} \quad (3.24b)$$

In the equations 3.22 and 3.24, the unknowns are the adherend plastic dissipation in bending, W_{pb} , the root curvature, k_o , and the root rotation, θ_o . The additional information needed to calculate the plastic dissipation energy, W_{pb} , may be obtained by analyzing the attached part of the adherend as an elastic-plastic beam on an elastic foundation.

3.5 Analysis of the attached part of the adherend

In this section, a new theory is developed for the deformation of an elastic-plastic beam on an elastic foundation in order to analyze the attached part of the flexible adherend. For this analysis, two simplifying approximations are made:

(i) *Long-beam assumption*: At point A on the attached beam, the deformation ceases to be elastic, and at the root B it reaches the highest degree of plastic deformation (Figs. 3.1). Generally, both the elastic and the elastic-plastic sections of the attached part of the adherend have to be analyzed. However, the problem is greatly simplified by making the assumption of a semi-infinite elastic-plastic beam on an elastic foundation. This approximation is equivalent to the long beam assumption in the theory of a beam on elastic foundation [84]. It may be shown that for the long beam assumption to be valid, the extent of the elastic-plastic section (A-B in Fig. 3.1) need only be greater than a few millimeters for typical peel tests.

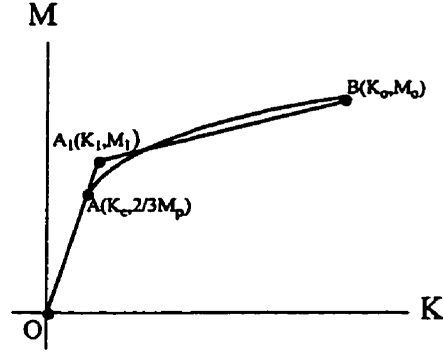


Figure 3.4 Linear approximation to the M-K relation for elastic-plastic loading

(ii) *Approximate m-k relation for elastic-plastic section*: The actual moment curvature relationship for the elastic-plastic section of the attached part of the adherend is given by Eq. 3.11. However, due to the non-linear nature of the m-k relation, an analytical treatment of the deformation of the attached part of the adherend becomes impossible. To overcome this difficulty, a linear approximation to the moment-curvature relation during the elastic-plastic bending is used, as shown in Fig. 3.4. A rational way to linearize the elastic-plastic section of the M-K diagram is to equate the area (i.e., the energy dissipated) under the actual M-K diagram (O-A-B) to that under the approximated M-K diagram (O-A₁-B). Finally an approximate, normalized moment-curvature relation for plastic-loading section (A₁-B) may be obtained as:

$$m_{A_1B}(k) = m_1 + \varsigma (k - k_1) \quad (3.25)$$

where

$$\varsigma = \frac{(m_o - m_1)}{(k_o - k_1)} \quad (3.26)$$

$$k_1 = \left(\frac{k_o + 2}{2} - \frac{3m_o}{4} \right) - \sqrt{\left(\frac{k_o + 2}{2} - \frac{3m_o}{4} \right)^2 - 3 \left(\gamma - \frac{m_o k_o}{2} \right)} \quad (3.27)$$

$$m_1 = \frac{2}{3}k_1 \quad (3.28)$$

$$\gamma = (1 - \alpha) \left(k_o - 1 + \frac{1}{3k_o} \right) + \frac{\alpha k_o^2}{3} \quad (3.29)$$

This linearization procedure is a reasonably accurate description of common peel tests for adhesive joints. It may be readily shown that when $k_o \gg 1$, the actual m - k relation (Eq. 3.11) for stage A-B is in fact nearly linear.

Beam-on-elastic-foundation: According to the theory of beam on an elastic foundation, the beam displacements and the foundation stresses are related as follows [33]:

$$\sigma_{yy} = \lambda_{\sigma} \nu; \quad \tau_{xy} = \lambda_{\tau} u \quad (3.30)$$

where ν and u are the vertical and horizontal beam displacements, and λ_{σ} and λ_{τ} are the effective normal and tangential foundation constants (or foundation moduli), respectively. In the case of adhesive joints, it is important to consider the compliances of both the adhesive and the adherend. The adherend compliance is due to the fact that the adherend does not act as a built-in cantilever, and undergoes some rotation at the root even in the extreme case of a perfectly rigid adhesive [41, 42]. The effective foundation constant may be calculated by assuming that the adhesive and adherend compliances act in series [82, 83]:

$$\frac{1}{\lambda_{\sigma}} = \frac{1}{\lambda_{\sigma}^{ads}} + \frac{1}{\lambda_{\sigma}^{adn}}; \quad \frac{1}{\lambda_{\tau}} = \frac{1}{\lambda_{\tau}^{ads}} + \frac{1}{\lambda_{\tau}^{adn}} \quad (3.31)$$

where the superscripts *ads* and *adn* represent the adhesive and the adherend, respectively. The adhesive is considered to be elastic, giving the following relations [83]:

$$\lambda_{\sigma}^{ads} = \frac{E_a}{t_a}; \quad \lambda_{\tau}^{ads} = \frac{\mu_a}{t_a} \quad (3.32)$$

where E_a and μ_a are the adhesive Young's modulus and shear modulus respectively, and t_a is the adhesive thickness.

Adherend foundation constant under elastic-plastic loading: In the presence of plastic deformation, the adherend foundation constants depend on the degree of plasticity. Expressions are sought for the normal and shear foundation constants of the adherend under elastic-plastic loading.

First, consider the normal foundation constant, λ_{σ}^{adn} , of the adherend. According to the deformation theory of plasticity (or total strain theory), the generalized Hooke's law may be used to relate the stress and total strain, provided that E and ν (Poisson ratio) are replaced by the secant modulus E_s (Fig. 3.2) and 0.5, respectively [84]. By using these relations, and Kanninen's approach for the elastic case [42], the normal foundation constant of the adherend may be shown to be:

$$\lambda_{\sigma}^{adn} = \frac{2E_s}{h} \quad (3.33)$$

The secant modulus, E_s , may be obtained from the bilinear stress-strain relations (Eq. 3.6b), provided that the effective total strain, ϵ_e , (Fig. 3.2) is known, i.e.,

$$E_s = \frac{\sigma_y}{\epsilon_e} (1 - \delta) + \delta E \quad (3.34)$$

For the purpose of deriving an analytical expression for E_s , the effective strain ϵ_e is assumed to be equal to the maximum bending strain at the root:

$$\epsilon_e = \frac{1}{2} K_o h \quad (3.35)$$

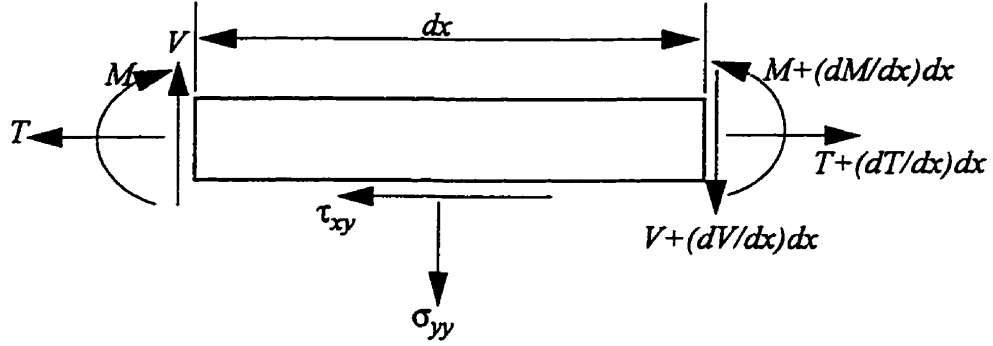


Figure 3.5 Free body diagram of a differential element on the attached part of the flexible adherend

The foundation constant for the shear deformation (λ_{τ}^{adh}) may be obtained in a similar manner as:

$$\lambda_{\tau}^{adh} = \frac{2E_s}{3h} \quad (3.36)$$

Governing equation: Figure 3.5 shows a differential element of the attached part of the adherend. By applying the equilibrium equations to this element [33], together with the linear m-k relation (Eq. 3.25), and Eq. 3.30, the following differential equation may be obtained governing the foundation shear stress (Appendix A):

$$\frac{d^7 \tau_{xy}}{dx^7} - Q_1 \frac{d^5 \tau_{xy}}{dx^5} + Q_3 \frac{d^3 \tau_{xy}}{dx^3} - Q_5 \frac{d \tau_{xy}}{dx} = 0 \quad (3.37)$$

The foundation normal stress may be found from the following equation (Appendix A):

$$\sigma_{yy} = \frac{Q_1 d \tau_{xy}}{Q_2 dx} - \frac{1}{Q_2} \frac{d^3 \tau_{xy}}{dx^3} \quad (3.38)$$

where

$$Q_1 = \frac{\lambda_\tau}{Eh} \left(1 + \frac{2}{\zeta} \right); \quad Q_2 = \frac{4\lambda_\tau}{\zeta Eh^2}; \quad Q_3 = \frac{8\lambda_\sigma}{\zeta Eh^3}; \quad (3.39)$$

$$Q_4 = \frac{4\lambda_\sigma}{\zeta Eh^2}; \quad Q_5 = Q_1 Q_3 - Q_2 Q_4 \quad (3.40)$$

The general solution to Eq. 3.37 is:

$$\begin{aligned} \tau_{xy}(x) = & C_1 + C_2 e^{-\kappa x} + C_3 e^{\kappa x} + e^{\eta_r x} [C_4 \cos(\eta_i x) + C_5 \sin(\eta_i x)] \\ & + e^{-\eta_r x} [C_6 \cos(\eta_i x) + C_7 \sin(\eta_i x)] \end{aligned} \quad (3.41)$$

where κ , $-\kappa$, $\eta_r \pm \eta_i$ and $-\eta_r \pm \eta_i$ are the roots of the characteristic equation of Eq. 3.37.

Because of the long beam assumption, four of the seven constants (C_1 , C_2 , C_6 and C_7) are zero, by virtue of the boundary condition that $\tau_{xy} = 0$, as $x \rightarrow -\infty$. Equation 3.41 may be re-written as:

$$\tau_{xy}(x) = C_3 e^{\kappa x} + e^{\eta_r x} (C_4 \cos(\eta_i x) + C_5 \sin(\eta_i x)) \quad (3.42)$$

The following boundary conditions are valid at the root ($x = 0$):

$$[T]_{x=0} = \frac{P}{b} \cos \phi = \frac{Eh}{\lambda_\tau} \left[\frac{d\tau_{xy}}{dx} \right]_{x=0} - \frac{Eh^2}{2} K_0; \quad (3.43)$$

$$[V]_{x=0} = \frac{P}{b} \sin \phi = \frac{Eh^3 \zeta}{8Q_2 \lambda_\sigma} \left[\frac{d^6 \tau_{xy}}{dx^6} \right]_{x=0} - \frac{Q_1 Eh^3 \zeta}{8Q_2 \lambda_\sigma} \left[\frac{d^4 \tau_{xy}}{dx^4} \right]_{x=0} + \frac{h}{2} [\tau_{xy}]_{x=0} \quad (3.44)$$

$$[K]_{x=0} = K_0 = \left[\frac{d^2 v}{dx^2} \right]_{x=0} = \frac{1}{\lambda_\sigma} \left[\frac{d^2 \sigma_{yy}}{dx^2} \right]_{x=0}; \quad (3.45)$$

$$[\tan \theta]_{x=0} = \tan \theta_0 = \left[\frac{dv}{dx} \right]_{x=0} = \frac{1}{\lambda_\sigma} \left[\frac{d\sigma_{yy}}{dx} \right]_{x=0} \quad (3.46)$$

where T and V are the axial and shear forces respectively. From Eq. 3.42 and Eqs. 3.43-3.46, the following simultaneous algebraic equations may be obtained:

$$\kappa C_3 + \eta_r C_4 + \eta_i C_5 = \lambda_\tau \left(\frac{hk_o K_e}{2} + \frac{P \cos \phi}{Ebh} \right) \quad (3.47)$$

$$\left(\frac{Q_1 \kappa^4 - \kappa^6}{Q_2} - Q_4 \right) C_3 + a_4 C_4 + a_5 C_5 = -\frac{8\lambda_\sigma P \sin \phi}{Ebh^3} \quad (3.48)$$

$$\frac{Q_1 \kappa^3 - \kappa^5}{Q_2} C_3 + b_4 C_4 + b_5 C_5 = k_o K_e \lambda_\sigma \quad (3.49)$$

$$\frac{Q_1 \kappa^2 - \kappa^4}{Q_2 \lambda_\sigma} C_2 + d_3 C_3 + d_4 C_4 = \tan \theta_0 \quad (3.50)$$

where

$$a_4 = \frac{1}{Q_2} [Q_1 (\eta_r^4 - 6\eta_r^2 \eta_i^2 + \eta_i^4) - \eta_r^6 + 15\eta_r^4 \eta_i^2 - 15\eta_r^2 \eta_i^4 + \eta_i^6] - Q_4 \quad (3.51)$$

$$a_5 = \frac{1}{Q_2} [Q_1 (4\eta_r^3 \eta_i - 4\eta_r \eta_i^3) - 6\eta_r^5 \eta_i + 20\eta_r^3 \eta_i^3 - 6\eta_r \eta_i^5] \quad (3.52)$$

$$b_4 = \frac{1}{Q_2} [Q_1 (\eta_r^3 - 3\eta_r \eta_i^2) - \eta_r^5 + 10\eta_r^3 \eta_i^2 - 5\eta_r \eta_i^4] \quad (3.53)$$

$$b_5 = \frac{1}{Q_2} [Q_1 (-\eta_i^3 + 3\eta_r^2 \eta_i) - \eta_i^5 + 10\eta_r^2 \eta_i^3 - 5\eta_r^4 \eta_i] \quad (3.54)$$

$$d_4 = \frac{1}{\lambda_\sigma Q_2} (Q_1 (\eta_r^2 - \eta_i^2) - \eta_r^4 - \eta_i^4 + 6\eta_r^2 \eta_i^2) \quad (3.55)$$

$$d_5 = \frac{1}{\lambda_\sigma Q_2} (2Q_1 \eta_r \eta_i + 4\eta_r \eta_i^3 - 4\eta_r^3 \eta_i) \quad (3.56)$$

Equations 3.47-3.50 along with Eqs. 3.1, 3.22 and 3.24 are sufficient to calculate the adherend plastic dissipation during the peeling process.

Fracture energy from local stresses: The peel test may be considered as a mixed-mode fracture of some combination of mode I (opening mode) and mode II (sliding mode). Since the adhesive is considered to be elastic, the mode I and mode II components of the fracture energy may be expressed in terms of the foundation stresses (Eq. 3.42 and 3.39) as [83]:

$$G_I = \frac{\sigma_{yy}^2(0)}{2\lambda_\sigma}; \quad G_{II} = \frac{\tau_{xy}^2(0)}{2\lambda_\tau} \quad (3.57)$$

$$G_c = G_I + G_{II}; \quad \varphi = \text{atan} \left(\sqrt{\frac{G_{II}}{G_I}} \right) \quad (3.58)$$

where φ is the phase angle, which is a measure of the amount of mode-II component of G_c relative to its mode-I component. The fracture energy of many adhesives is a function of φ ; see, for example ref. [83].

Numerical implementation: The numerical solution for the critical fracture energy consists of solving the seven simultaneous equations, (3.1), (3.22), (3.24) and (3.47)-(3.50) for seven unknowns namely, C_3 , C_4 , C_5 , k_o , θ_o , W_{pb} and G_c . The mode ratio may be calculated from Eqs. 3.57-3.58. A Matlab program was written using the Newton-Raphson method to achieve the solution.

3.6 Numerical results

In this section, numerical simulation is carried out to study the variation in the magnitudes of adherend plastic dissipation with changes in material (adhesive/adherend) properties and peel angle. The adherend is assumed to be an elastic-perfectly plastic material ($\delta = 0$), and the foundation shear stress is neglected in the numerical studies. It was verified that, in most cases, the exclusion of the shear stress introduces an error less than 15% in the adherend plastic dissipation. Since the primary objective at this point is to seek general trends in the plastic dissipation, it is justified to simplify the calculations by neglecting the effect of the shear stress.

Figure 3.6 shows the ratio of external energy to the critical fracture energy (W_{ext}/G_c) plotted against G_c , calculated for various values of adherend thickness and yield stress at $\phi = 90^\circ$. The range for G_c was chosen to reflect typical structural adhesive joints, which have G_c ranging from 200 - 3000 J/m^2 . It is noted from Fig. 3.6 that, for a given G_c , the external energy, W_{ext} , and hence the adherend plastic dissipation ($W_{ext} = G_c + W_{pb}$) can be very sensitive to the adherend properties. Therefore, it is important to choose the adherend properties such that the adherend plastic dissipation is kept small. It is observed from Fig. 3.6 that for high-fracture energy systems, the use of low values of adherend thickness and yield stress keeps the effects of adherend plastic dissipation small. On the other hand for low fracture energy systems, the use of relatively high values of the thickness and yield stress would be desirable to keep the plastic dissipation effects low. It is also noted from Fig. 3.6 that for given adherend properties and peel angle, there is a particular value of G_c at which the plastic dissipation effects are the maximum.

Previous investigators [36, 41] have pointed out the existence of a critical adherend thickness at which the plastic dissipation is a maximum for a given G_c . Figure 3.7 shows the

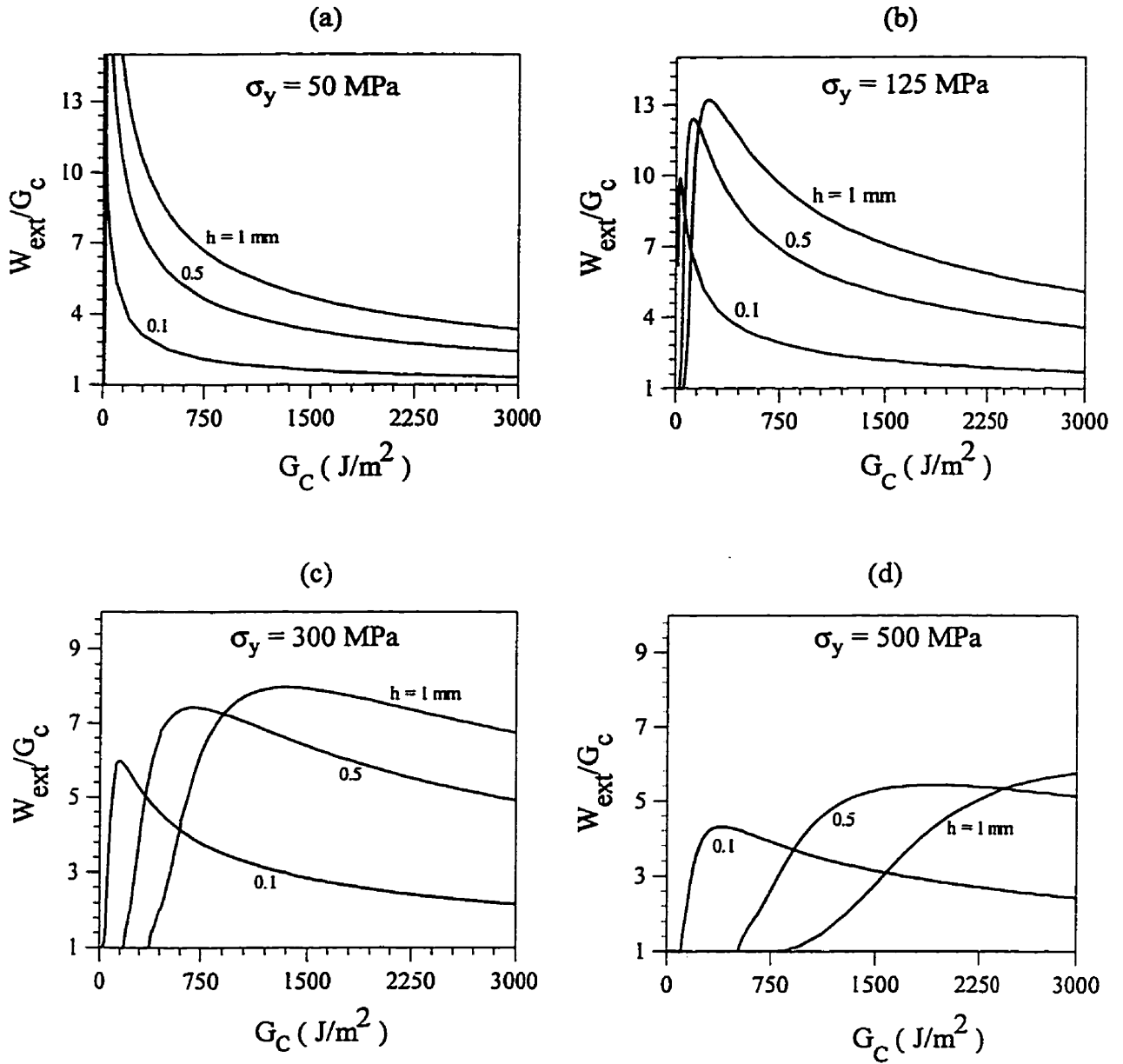


Figure 3.6 Effect of adherend properties on plastic dissipation: W_{ext}/G_c versus G_c for adherends of different thickness and yield stress; the joint parameters used are: $\phi = 90^\circ$, $E_a = 2.5$ GPa and $t_a = 0.4$ mm.

variation of W_{ext}/G_c with adherend thickness h , for several values of the yield stress σ_y , and for two extreme values of G_c (250 and 2500 J/m^2). The range of thickness was chosen to reflect common peel tests for metallic adhesive joints. The figure does indeed predict the

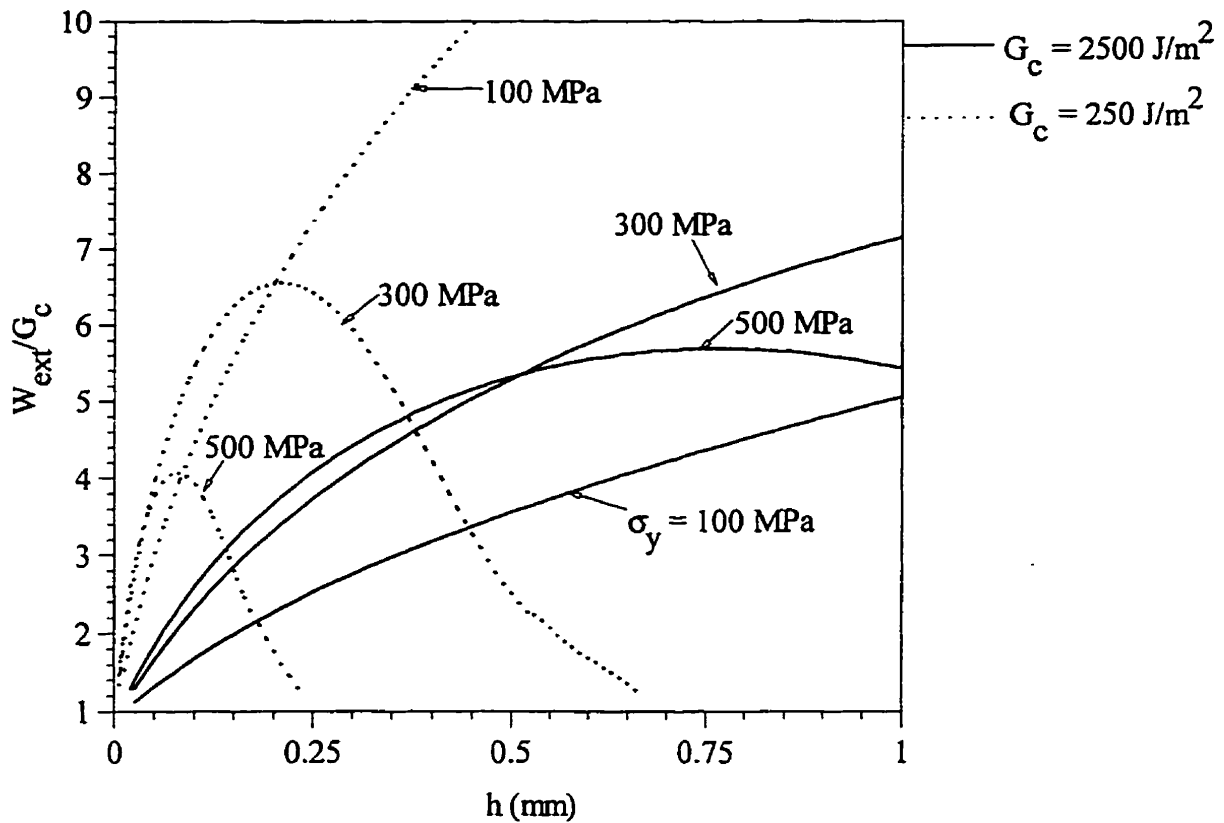


Figure 3.7 Existence of a critical adherend thickness: W_{ext}/G_c versus h for various values of G and σ_y ; the joint parameters used are: $\phi = 90^\circ$, $E_a = 2.5$ GPa and $t_a = 0.4$ mm.

existence of a critical adherend thickness, although not all the maxima fall within the useful thickness range.

A closer examination of Fig. 3.7 reveals that for a low fracture system, the use of a high yield strength material with a thickness much larger than the critical thickness keeps the adherend plastic dissipation low. This is consistent with the conclusions drawn from Fig. 3.6. The alternative solution of choosing an adherend thickness much smaller than the critical thickness would not be feasible in this case since the thickness would be too small, and the adherend might yield in tension. For medium to high fracture energy systems (most structural adhesive systems fall in this category), the use of a low yield-strength adherend with a thickness much smaller than the critical thickness is the preferred solution for minimizing the effects of plastic dissipation.

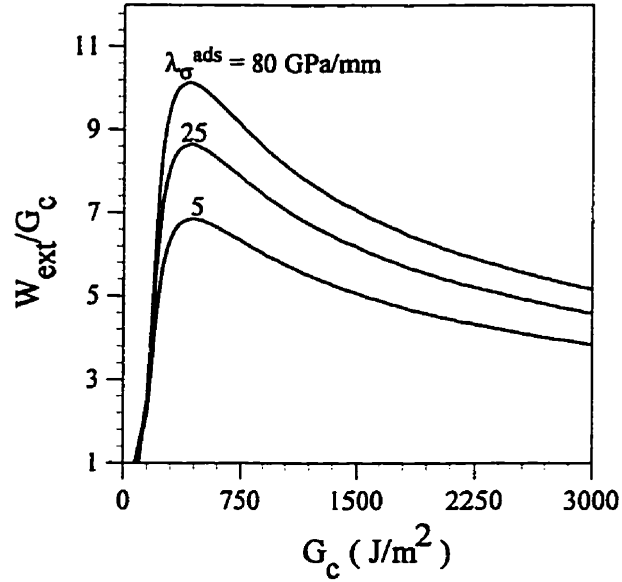


Figure 3.8 Effect of adhesive properties on plastic dissipation: W_{ext}/G_c versus G_c for various values of the normal adhesive foundation constant (λ_{σ}^{ads}); the joint parameters used are: $\phi = 90^\circ$, $\sigma_y = 300$ MPa and $h = 0.3$ mm.

Figure 3.8 shows the variation of W_{ext}/G_c vs. G_c for various values of the ratio of adhesive modulus to thickness (i.e., the normal foundation constant of the adhesive). It is observed that the plastic dissipation increases with increasing foundation constant. This is expected intuitively, since the root curvature becomes sharper with increasing adhesive stiffness for a given adhesive thickness.

Figure 3.9 shows the ratio W_{ext}/G_c vs. the peel angle, ϕ , for fixed values of G_c and adherend properties. It is observed that W_{ext}/G_c , and hence the adherend plastic dissipation, increases steadily with peel angle, a trend which has been reported elsewhere [85]. The result is expected on physical grounds, since an increase in peel angle would cause the root radius of the adherend to become sharper, thereby leading to an increase in plastic dissipation. It should be realized that for very low values of peel angle, the predominant deformation of the adherend is tensile. The present model, which assumes pure bending for the detached part of the adherend, may not be applicable in this case.

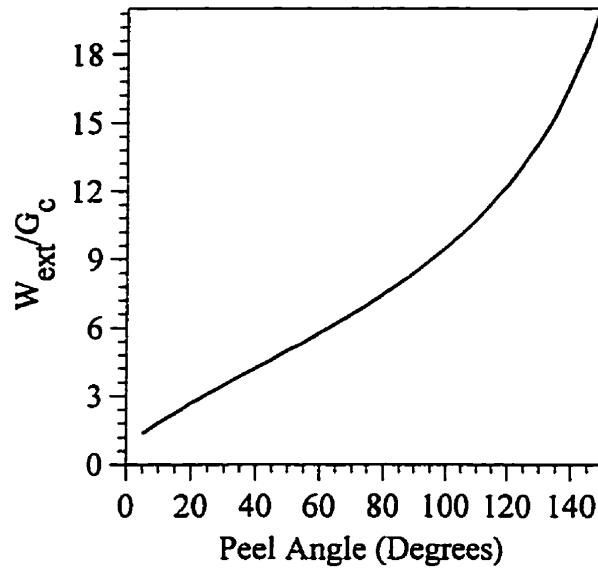


Figure 3.9 Effect of peel angle on plastic dissipation: W_{ext}/G_c versus ϕ ; the joint parameters used are: $\sigma_y = 250$ MPa, $h = 0.5$ mm, $E_a = 2.5$ GPa and $t_a = 0.4$ mm and $G_c = 1000$ J/m².

3.7 Experimental validation of the model

For a given adhesive system (adherend material, surface treatment and adhesive), the critical fracture energy should be independent of the peel angle, adherend thickness and adherend yield stress, provided that the mode ratio and the contribution of the crack-tip dissipation to G_c do not vary with the test geometry. Therefore, the strategy for the experimental validation of the model was to predict G_c and mode ratio by applying the model to experimental peel data obtained from specimens prepared using the same metal, surface pretreatment and adhesive; the only variables were the peel angle, the adherend thickness and the adherend yield stress.

3.7.1 The peel data

Two sets of experimental peel data were analyzed. The data set I is from ref. [38], and the data set II corresponds to the peel tests carried out in the present work. Data set I includes two aluminum alloys as the flexible adherend; namely, a relatively high yield-strength AA2024-T3 alloy and a relatively low yield-strength BS 3L61 alloy. The peel specimens were prepared

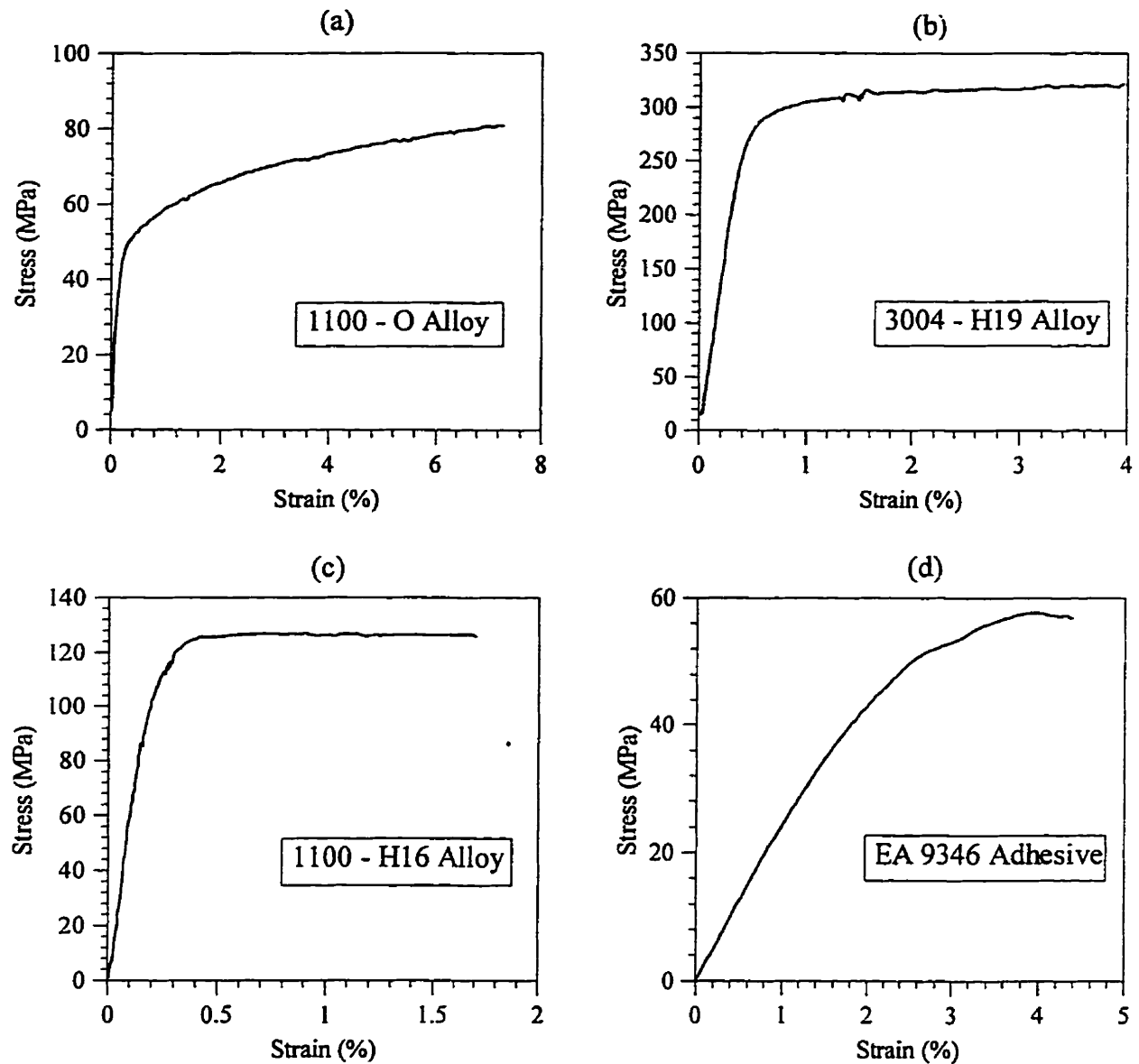


Figure 3.10 Stress-Strain diagrams; (a) AA1100-O alloy, (b) AA3004-H19 alloy, (c) AA1100-H16 alloy, (d) Hysol EA9346 adhesive

with a rubber-modified epoxy as the adhesive. Peel tests were conducted for angles of 30° , 60° and 90° with each alloy. The adherend properties, obtained from the bilinear approximation to the uniaxial stress-strain curves reported in [38] are shown in Table 3.1. Young's modulus for this adhesive was reported to be 2.0 GPa [38].

Data set II was obtained experimentally using three aluminum alloys (AA1100-O, 3004-H19 and 1100-H16) as the flexible adherends, varying in thickness and yield characteristics. Uniaxial tension tests were carried out to determine the yield stress and strain hardening characteristics of the alloys; the results are shown in Figs. 10a to 10c. Table 3.2 contains the adherend properties from a bilinear fit to the stress-strain curves. The adhesive used was Hysol EA 9346, an unfilled single-part epoxy adhesive. Tension tests were conducted on 0.4 mm thick cast specimens of the adhesive (Fig. 3.10d) giving a Young's modulus of about 2.5 GPa.

The flexible adherends were pretreated using the FPL etch (ASTM 2162) procedure, and the joints were cured according to the manufacturer's instructions. The peel tests were conducted at a rate of 5 mm per minute, for three peel angles (45° , 90° and 135°) for the AA1100-O and AA1100-H16 alloys, and for two peel angles (45° and 90°) for AA3004-H19 alloy. Six to seven specimens, from different batches, were tested for each peel angle with the AA1100-O and AA3004-H19 alloys, and three to four specimens from two batches were used for each peel angle with the AA1100-H16 alloy.

3.7.2 Results and discussion

Table 3.1 gives the results of an analysis of data set I. The external energy was calculated using Eq. 3.2. The critical fracture energy, G_c , was determined using Eq. 3.1 together with Eqs. 3.47-3.50, Eq. 3.22 and Eq. 3.25. The mode-ratio was obtained using Eqs. 3.57-3.58. A finite-element analysis of these peel tests may be found in ref. [38]. Table 3.2 gives a corresponding analysis of the data set II

Effects of peel angle and adherend properties: It may be observed from both Tables 3.1 and 3.2 that the external work increases greatly with increase in peel angle, as predicted by the model for a given G_c (Fig. 3.9). For a given peel angle and G_c , the numerical predictions showed that the plastic dissipation is very sensitive to the adherend thickness and yield stress (Fig. 3.6). It may be observed from Tables 3.1 and 3.2 that, for a given peel angle the external energy is very sensitive to the adherend properties. It was found from the numerical results

(see Fig. 3.6 and 3.7) that for medium to high-strength adhesives, such as the adhesives used in both data sets I and II, the effects of plastic dissipation may be kept relatively by employing a relatively thin adherend with low yield stress. Referring to Table 3.2, it may be noted that the AA1100-O (which has a relatively low yield stress and thickness), with a 45° peel angle gave the lowest value of external energy compared to other combinations of alloy and peel angle.

Table 3.1 Analysis of data set I

Alloy Type	ϕ (Deg.)	P (N/mm)	W_{ext} (J/m ²)	G_c (Eq. 3.1) (J/m ²)	ϕ (Deg.)	ϵ_t^{adh}	ϵ_t^{ads}
2024 - T3 $h = 0.64$ mm $\sigma_y = 330$ MPa $\delta = 0.02$	30	23.2	3121	930	31.3	0.041	0.066
	60	7.3	3651	769	31.9	0.036	0.058
	90	4.3	4300	730	33.6	0.034	0.054
BS 3L61 $h = 0.57$ mm $\sigma_y = 65$ MPa $\delta = 0.003$	30	22.5	3027	970	37.9	0.070	0.100
	60	9.4	4702	1060	38.1	0.083	0.118
	90	6	6001	1060	39.9	0.086	0.123

Critical fracture energy (G_c): Table 3.1 gives the critical fracture energy determined for data set I. It is noted that for the relatively high yield strength aluminum alloy (AA 2024 - T3), the phase angle remains approximately constant with increase in peel angle, and thus it is expected that G_c should be largely independent of the peel angle. However, it is observed that G_c for the 30° case is somewhat higher than the other two peel angles. This is possibly because the calculated fracture energy includes the energy dissipation due to local adhesive plastic and visco-elastic effects. The finite element analysis of the peel tests, carried out by Crocombe and Adams [38], showed that the adhesive plastic zone sizes are greater for lower peel angles. Therefore, the increased crack-tip dissipation for low peel angles may explain the higher fracture energy calculated for low peel angles in the case of the AA2024-T3 alloy. This is further confirmed by the trends in the calculated values of the average transverse or

thorough-thickness strain at the root, both in the adherend, $\varepsilon_t^{\text{adh}}$, and the adhesive, $\varepsilon_t^{\text{ads}}$, (Table 3.1). It may be observed that G_c increases with the transverse strains; implying an increase in fracture energy due to enhanced plastic and visco-elastic effects in the vicinity of the crack tip.

Table 3.2 Analysis of data set II

Alloy Type	ϕ (Deg.)	P (N/mm)	W_{ext} (J/m ²)	G_c (Eq. 3.1) (J/m ²)	ϕ (Deg.)	$\varepsilon_t^{\text{adh}}$	$\varepsilon_t^{\text{ads}}$
1100 - O h = 0.12 mm $\sigma_y = 48$ MPa $\delta = 0.0065$	45	5.2 ± 0.28	1526	890	27.1	0.319	0.048
	90	2.3 ± 0.06	2301	913	30.3	0.309	0.046
	135	1.81 ± 0.1	3051	932	34.1	0.294	0.044
3004 - H19 h = 0.3 mm $\sigma_y = 300$ MPa $\delta = 0.003$	45	14.1 ± 0.82	4140	1195	28.3	0.122	0.046
	90	6.2 ± 0.43	6201	935	32.2	0.103	0.039
1100 - H16 h = 1.25 mm $\sigma_y = 120$ MPa $\delta = 0.0005$	45	36.9 ± 3.2	10824	2284	40.0	0.060	0.094
	90	16.4 ± 0.16	16403	1822	42.3	0.097	0.152
	135	14.2 ± 0.55	24243	1558	46.2	0.147	0.230

For the lower yield strength alloy (BS 3L61), the predicted G_c is higher than that of the AA 2024-T3 alloy system, consistent with an appreciably higher overall phase angle, ϕ . The crack-tip dissipation effects may play a role as described above, as confirmed by the similar trends in G_c , and the adhesive and adherend transverse strains (Table 3.1).

Given that the two aluminum alloys (AA2024-T3 and BS 3L61) had the same pretreatment, and that the same adhesive was used to make the peel specimens of both the alloys, the fracture energy should be equal for the two systems at a particular phase angle, ϕ . The G_c values determined using the model bear this out well, and the differences in the

estimates of G_c between the two alloys can be explained by the mode of loading (i.e., an overall change in the phase angle) and the crack-tip dissipation effects.

Table 3.2 gives the critical fracture energy determined for data set II. For AA1100-O alloy, the phase angles do not change greatly with change in peel angle, and accordingly G_c values are about the same for all peel angles. For AA3004-H19, the phase angles for both peel angles remain about the same as that for AA1100-O; however, G_c for the 45° case is appreciably higher than that for the 90° case. This may be again due to an increase in crack-tip dissipation effects as explained above, as revealed by the higher transverse strains at 45° angle compared to 90° (Table 3.2).

For the relatively thick AA1100-H16 alloy, the phase angle is appreciably higher than for the other two alloys, and the fracture energy values are accordingly higher. However, it should be noted that the adherend plastic dissipation is so high for this case (80 to 94% of the external energy) that the approximations used in the analysis may significantly affect the estimates of the fracture energy.

Ultrasonic Nondestructive Evaluation: Theoretical Aspects

In this chapter, theoretical aspects of the characterization of the adhesive/adherend interfacial region using ultrasound are investigated. First, the plane wave reflection coefficients from the interfacial region, for both normal and oblique incidence, are studied using the spring model (Section 2.4.4.3). Next, a new angular spectrum approach is developed to model an oblique-incidence, focused wave measurement system for the interfacial characterization of adhesive joints [86, 87]. Numerical simulation results are given for typical adhesive joints, using the spring model to describe the interfacial region.

4.1 Plane-wave reflection coefficients of the interfacial region

This section considers the plane-wave ultrasonic reflection coefficients (ratio of the amplitude of the reflected wave to that of the incident wave) of the adhesive/adherend interfacial region, which might be used as indicators of the interfacial strength. First, normally incident waves are considered.

4.1.1 Normal incidence

In the study of ultrasonic wave reflection from planar interfaces, the case of normally incident waves is the simplest to analyze since it deals with the one-dimensional form of the wave equation [70]. It is of interest to derive expressions for the normal-incidence reflection coefficient of longitudinal and shear waves incorporating the spring boundary condition, given by:

$$(\sigma_{zz})_1 = (\sigma_{zz})_2 = K_n(w_2 - w_1), \quad (\tau_{xz})_1 = (\tau_{xz})_2 = K_t(u_2 - u_1) \quad (4.1)$$

where σ_{zz} and w are the normal stress and displacement respectively, τ_{xz} and u are the

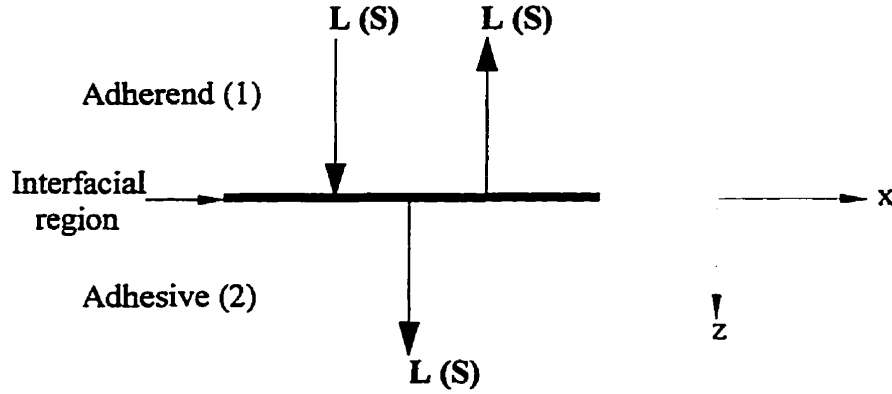


Figure 4.1: Schematic of a plane wave normally incident at the interfacial region; 'L' represents longitudinal wave and 'S' represents shear wave.

tangential stress and displacement respectively, and K_n and K_t are the normal and tangential spring constants respectively. The subscripts 1 and 2 represent the top and bottom half-spaces respectively (Fig. 4.1). Seeking a plane harmonic wave solution to the one-dimensional form of the wave equation, the following expressions for the normal-incidence plane wave reflection coefficient of longitudinal (R_{ll}) and shear (R_{ss}) waves, respectively, may be derived [58]:

$$R_{ll} = \frac{Z_{2l} - Z_{1l} + i\omega Z_{1l}Z_{2l}/K_n}{Z_{2l} + Z_{1l} - i\omega Z_{1l}Z_{2l}/K_n} \quad (4.2a)$$

$$R_{ss} = \frac{Z_{2s} - Z_{1s} + i\omega Z_{1s}Z_{2s}/K_t}{Z_{2s} + Z_{1s} - i\omega Z_{1s}Z_{2s}/K_t} \quad (4.2b)$$

where $Z = \rho c$ is the specific acoustic impedance, ρ and c being the density and wave velocity, respectively, and ω is the circular frequency. In Eq. 4.2, the subscripts l and s denotes longitudinal and shear waves, respectively.

Table 4.1 Material properties used in the simulations

	c_l (m/s)	c_t (m/s)	ρ (kg/m ³)
Aluminum	6435	3160	2690
Epoxy	2530	1175	1360

Figure 4.2 reveals the essential features of the spring model. It shows the normal-incidence, shear-wave reflection coefficient (R_{ss}) from an aluminum-epoxy interface, plotted against frequency for various values of the spring constant ranging from a perfect bond ($K_t \rightarrow \infty$) to a complete debond ($K_t \rightarrow 0$). The material properties used in the calculations are given in Table 4.1. It is seen that for a given frequency, the spring model predicts a gradually increasing reflection coefficient with a decrease in the spring constant. The reflection coefficient approaches the usual values of $(Z_{2s} - Z_{1s}) / (Z_{2s} + Z_{1s})$ for a perfect bond, and unity for a debond. For the two extreme cases of a perfect bond and a debond, the reflection coefficient is independent of frequency. It is observed that for intermediate values of the spring constant, the reflection coefficient shows a frequency dependence. The normal longitudinal-wave reflection coefficient shows a similar behavior as the shear wave reflection

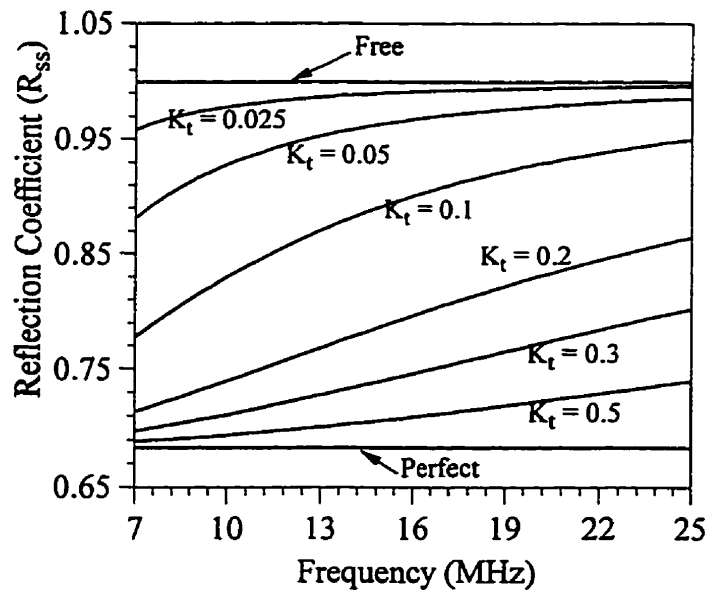


Figure 4.2: Normal-incidence shear-wave reflection coefficient spectra for various values of the tangential spring constant, K_t .

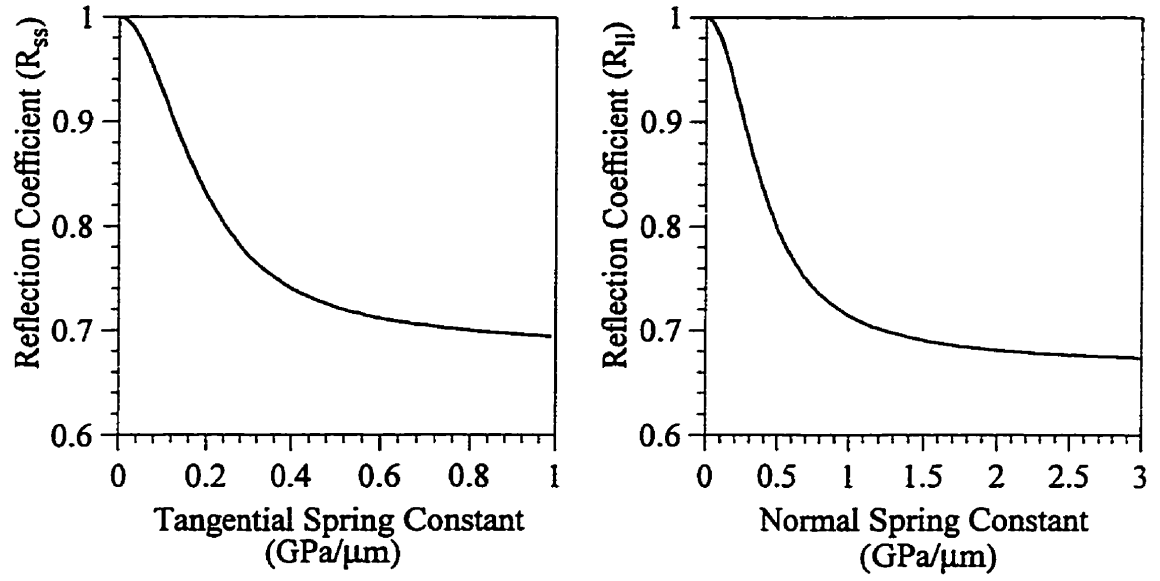


Figure 4.3: Normal-incidence reflection coefficient versus spring constant; (a) shear wave, (b) longitudinal wave.

coefficients. In principle, the normal and tangential spring constants may be determined by measuring the plane wave reflection coefficient spectra of normally incident longitudinal and shear waves, respectively.

Figure 4.3(a) and 4.3(b) gives the normal-incidence shear and longitudinal reflection coefficient at 15 MHz plotted against the relevant spring constant. The reflection coefficient decreases from unity, corresponding to a free bond, and approaches a limiting value, corresponding to a perfect bond. In practice, the measurement of the reflection coefficient, R , can be used to determine the spring constant, K , if they fall in the range where R changes with K . By comparing Fig. 4.3(a) and 4.3(b), it may be observed that the increase in R_{ss} with a change in K_t is greater than the increase in R_{ll} with a proportional change in K_n , especially for small changes in the spring constants from the limiting case of a perfect bond. Therefore, generally speaking, it may be said that shear waves are more sensitive to interfacial properties. This is expected on physical grounds, since shear waves have shorter wavelengths than longitudinal waves.

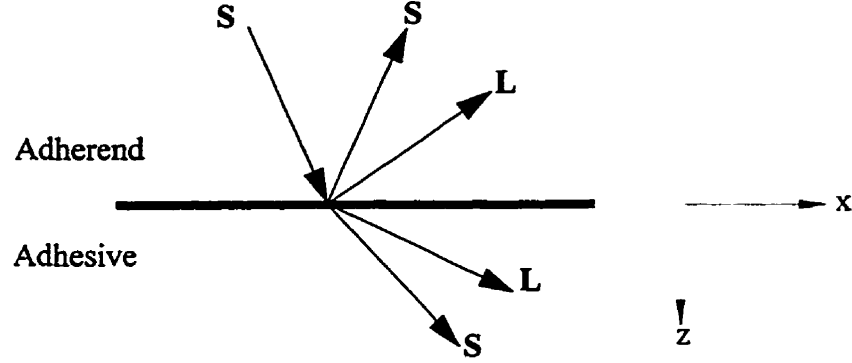


Figure 4.4: Schematic of the oblique-incidence, shear wave reflection from the interfacial region.

4.1.2 Oblique incidence

In practice, normal-incidence shear wave inspection of the interfacial region is difficult to perform reliably due to the variabilities associated with coupling. On the other hand, vertically polarized, oblique shear waves may be readily generated within the adherend by mode-conversion of oblique longitudinal waves at the adherend top surface. The analysis of the reflection of obliquely incident plane waves from the adhesive/adherend interfacial region (Fig. 4.4) is relatively complicated because of mode-conversion, and the involvement of both the normal and the tangential spring constants simultaneously. The solution may be achieved by the wave-potential theory (Section 2.4.4), and the following relations may be derived for the reflection and transmission coefficients of incident longitudinal and shear waves respectively (Appendix B):

$$[Q] \begin{bmatrix} R_{ls} \\ R_{ll} \\ D_{ls} \\ D_{ll} \end{bmatrix} = [q]_l \quad [Q] \begin{bmatrix} R_{ss} \\ R_{sl} \\ D_{ss} \\ D_{sl} \end{bmatrix} = [q]_s \quad (4.3)$$

where R and D are the reflection and transmission coefficients of the interfacial region, respectively, and the subscripts l and s represent longitudinal and shear waves, respectively.

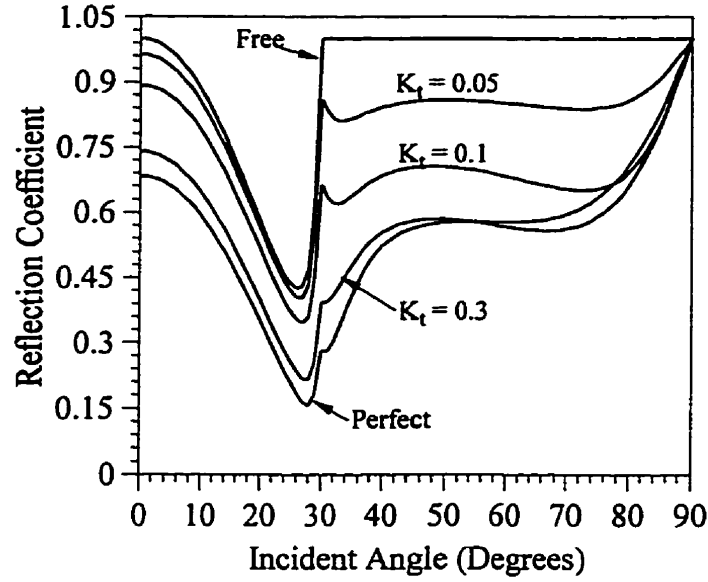


Figure 4.5: Oblique shear reflection coefficient versus angle of incidence for various values of the spring constants. The ratio of normal to tangential spring constant, K_n/K_t , is fixed at 4.

The elements of Q and q , which are given in Appendix B, depend on the bulk material properties, the spring constants, and the ultrasonic parameters such as frequency and incident angle.

The oblique incident reflection coefficient shows the spectral properties described earlier for the normal-incidence case. An important feature of oblique incidence is the angular dependance of the plane wave reflection coefficients [59], which is due to the energy partition associated with reflection, refraction and mode-conversion at the interface. Figure 4.4 gives the angular characteristics of the shear-to-shear reflection coefficient (R_{SS}), for various values of the spring constants ranging from a perfect bond ($K_n = K_t \rightarrow \infty$) to a debond ($K_n = K_t \rightarrow 0$). For the intermediate values of the spring constants, it has been assumed that $K_n/K_t \approx 4$, based on normal incidence longitudinal and shear wave measurements on a freshly prepared adhesive joint. The frequency is 15 MHz, and the material properties used in the calculations are given in Table 4.1. It is observed from Fig. 4.5 that the angular response of R_{SS} is quite sensitive to change in spring constants. The incident angle most sensitive to

change in the spring constants is about 30° , which represents a critical angle at which the reflected longitudinal wave (Fig. 4.4) becomes an inhomogeneous plane wave parallel to the interface.

4.2 Oblique-incidence, focused wave measurement system

The plane-wave theory of ultrasonic reflection from the interfacial region assumes a transducer with infinite diameter; however in practice measurements must be carried out using finite-sized transducers. There is a need to account for the diffraction of the wave field caused by the finite size of the transmitter. Also, the ultrasonic model should account for the effects of the receiver characteristics on the measured signal.

Most commercial ultrasonic transducers in the high frequency range (> 15 MHz) are manufactured with a focussing lens. Focused transducers generate ultrasonic waves at a relatively wide range of angles simultaneously; it may be recalled that the sensitivity of the reflection coefficients to the spring constants is strongly angular dependant (Fig. 4.5). In this section, a theoretical framework for an oblique-incidence, focused ultrasonic measurement system for the interfacial characterization of adhesive joints is developed.

4.2.1 Measurement system

Figure 4.6 shows the schematic of a focused wave measurement system for oblique incidence inspection of the adhesive/adherend interfacial region. A focused source located in the coupling medium (water) launches waves over a wide range of angles depending on its aperture and focal length. These waves produce both longitudinal and shear waves over a range of angles inside the adherend by refraction/mode-conversion at the top surface of the adherend; these waves in turn are reflected at the interfacial region (Fig. 4.6b), thereby carrying information regarding the interfacial properties.

For a symmetrically placed, transmitter-receiver pair shown in Fig. 4.6, the signal at the receiver depends on the distance of the probe pair with respect to the specimen surface (L_v in Fig. 4.6). As the transmitter-receiver pair is moved towards the specimen from a front-wall focused position ($L_v = F \cos \theta$ where F is the focal length and θ is the nominal incident

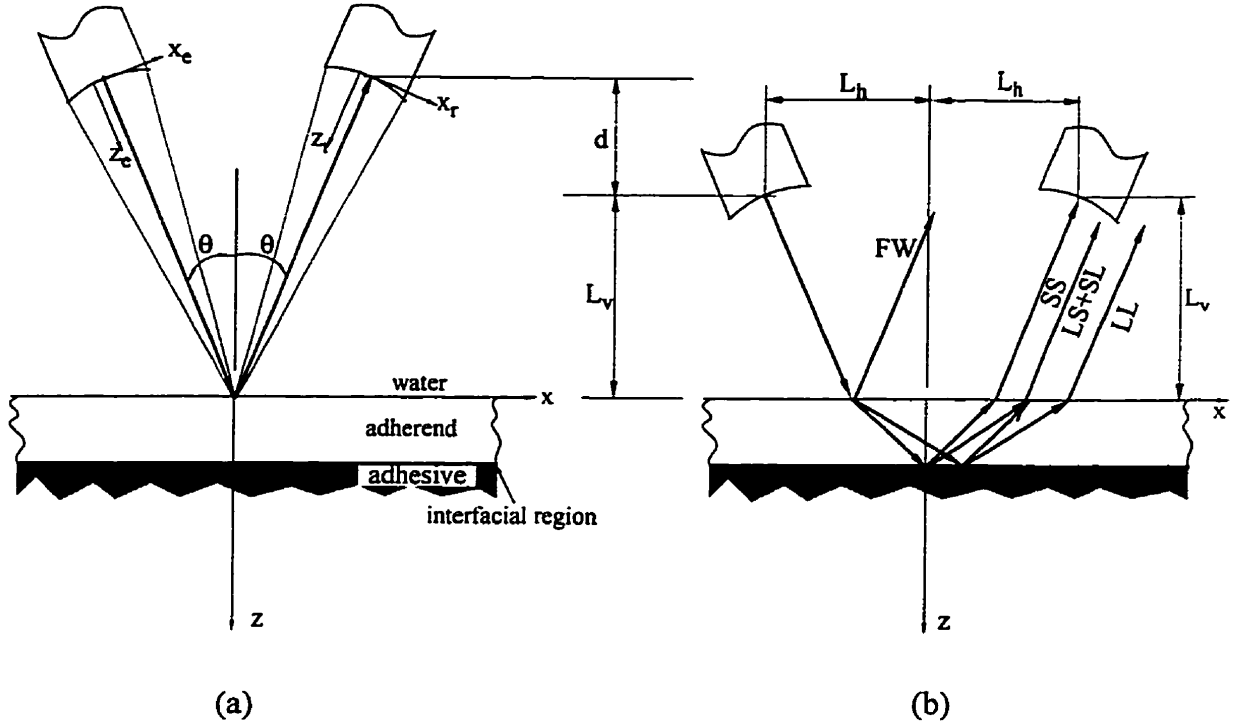


Figure 4.6: Oblique incidence, focused ultrasonic measurement system; (a) Front-wall focused configuration, (b) A configuration where the probe-pair is moved down to receive interfacial reflections.

angle), the various wave types reflected from the interfacial region are received successively. The three primary types of reflection from the interfacial region are referred to as SS, LS+SL and LL, where S denotes shear waves and L denotes longitudinal waves. It should be noted that each of the reflected wave types contains a range of angular components due to the use of a focused system. It is of interest develop a model to predict the signal corresponding to a specified type of reflection, as a function of the vertical distance, L_v , of the probe pair from the specimen, and frequency, ω .

4.2.2 Angular spectrum model for the measurement system

The angular spectrum or the plane wave decomposition method (Section 2.4.4.2) is a powerful tool to model radiation from a finite source [71, 88]. The present work developed an angular spectrum approach to model the measurement system shown in Fig. 4.6.

4.2.2.1 Emitted field

It is convenient to define the coordinate systems $x_e y z_e$, $x_r y z_r$, and $x y z$, attached to the emitter, the receiver and the specimen, respectively, as shown in Fig. 4.6a. The ultrasonic waves generated by the focused transducer can be described by a scalar potential, ϕ_e , which may be expressed as a superposition of plane waves by the following Fourier integral, in the emitter co-ordinates:

$$\phi_e(x_e, y, z_e, \omega) = \int_{-k_w}^{k_w} \int_{-k_w}^{k_w} A_e(\xi_e, \zeta, \omega) \exp[i(\xi_e x_e + \zeta y + \alpha_e z_e)] d\xi_e d\zeta \quad (4.4)$$

where $A_e(\xi_e, \zeta, \omega)$ is the angular spectrum of plane waves (i.e. the amplitude distribution of the various plane wave or angular components), k_w is the wave number in water (the coupling medium), and $\{\xi_e, \zeta, \alpha_e\}$ is the wave vector. The angular spectrum may be obtained by the inverse Fourier transform of Eq. 4.4 at the plane $z_e = 0$:

$$A_e(\xi_e, \zeta, \omega) = \frac{1}{(2\pi)^2} \int_{-\infty}^{\infty} \int_{-\infty}^{\infty} \phi_e(x_e, y, 0, \omega) \exp[-i(\xi_e x_e + \zeta y)] dx_e dy \quad (4.5)$$

where $\phi_e(x_e, y, 0)$ is the excitation at the source. To model a focused source, the thin lens approximation [71] is employed, by which the focused source is replaced by a plane source with appropriate phase term to account for focussing. The field at the source may then be written as:

$$\phi_e(x_e, y, 0, \omega) = P_e(x_e, y) \exp \left[-ikF_e \left(1 - \sqrt{1 - \frac{x_e^2 + y^2}{F_e^2}} \right) \right] \quad (4.6)$$

where $P_e(x_e, y)$ is the pupil or aperture function of the transmitter, and F_e is the focal length of the emitter in water. In the present work, the aperture function is assumed to be uniform

across the transducer aperture and zero outside. Using Eq. 4.6, the angular spectrum of the emitter (Eq. 4.5) may be readily evaluated, and the field emitted by the transmitter may be calculated by Eq. 4.4.

4.2.2.2 Reflected field

The multi-layered adhesive joint is insonified by the emitted wave field represented by Eq. 4.4 (see Fig. 4.6). To calculate the reflected field, it is convenient to work in the specimen coordinates, xyz . The following transformation equations from the emitter to the specimen coordinates may be obtained:

$$\xi_e = \xi \cos \theta - \alpha \sin \theta, \quad \alpha_e = \alpha \cos \theta + \xi \sin \theta \quad (4.7)$$

$$x_e = (x + L_h) \cos \theta - (z + L_v) \sin \theta, \quad z_e = (z + L_v) \cos \theta + (x + L_h) \sin \theta \quad (4.8)$$

Transforming Eq. 4.4 by using Eq. 4.7-4.8, the wave field incident on the adhesive joint may be re-written, in the specimen co-ordinates, as:

$$\phi_e(x, y, z, \omega) = \int_{-k}^k \int_{-k}^k A_e(\xi \cos \theta - \alpha \sin \theta, \zeta, \omega) \exp [i(\xi(x + L_h) + \alpha(z + L_v) + \zeta y)] \frac{(\alpha \cos \theta + \xi \sin \theta)}{\alpha} d\xi d\zeta \quad (4.9)$$

To obtain the reflected field, each angular or plane wave component of the incident field (Eq. 4.9) is multiplied by the corresponding plane wave reflection coefficient from the multi-layered structure (Section 2.4.4); the expression is then integrated over all ξ and ζ . The resulting field is a combination of all the possible reflected waves, including multiple reflections, within each of the layers involved.

There are two disadvantages to the multi-layered approach. First, the calculation of the plane wave reflection coefficient from the layered structure poses some numerical challenges (Section 2.4.4). The transfer matrix algorithm becomes unstable for typical combinations of adherend thickness and frequency range of interest. Therefore, computationally expensive

global matrix methods [67] must be used for the calculation of the plane wave reflection coefficient from the multi-layered structure.

Second, only the reflections from the upper interface (Fig. 4.6b) are of interest for the interfacial characterization of adhesive joints. If the multi-layered approach is used to calculate the entire reflection spectrum, the extraction of the spectrum due to a specific echo reflected from the top interfacial region is tedious: an inverse temporal Fourier transform must be performed on the entire (multi-layered) reflected spectrum. The echo of interest may then be singled out in the time domain and a forward temporal Fourier transform must then be performed on the specific echo to obtain its frequency spectrum.

To overcome the above drawbacks, a new formulation, termed the *resolved* approach, is now presented that concentrates on a specific wave type as it travels through the joint. Each of the plane wave components of a specified wave type, say the SS reflection, is weighted by the appropriate reflection and transmission coefficients as it crosses various interfaces. In addition, each plane wave component has an associated phase due to travel within the top adherend before re-emerging back into the coupling medium. Incorporating these ideas into Eq. 4.9, the following expression has been newly derived for the potential associated with each of the three primary reflected waves:

$$\begin{aligned} \phi_r^{mn}(x, y, z, \omega) = & \int_{-k_w}^{k_w} \int_{-k_w}^{k_w} A_e(\xi \cos \theta - \alpha \sin \theta, \zeta, \omega) \Gamma_{mn}(\xi, \zeta, \omega) \\ & \exp [i(\xi(x + L_h) + \alpha(L_v - z) + \zeta y)] \frac{(\alpha \cos \theta + \xi \sin \theta)}{\alpha} d\xi d\zeta \end{aligned} \quad (4.10)$$

where mn denotes ll , ls and ss , corresponding to the three primary reflections, LL, LS+SL, and SS, respectively. The function Γ_{mn} is defined by, for the SS case

$$\Gamma_{ss}(\xi, \zeta, \omega) = T_{ls}(\xi, \zeta) R_{ss}(\xi, \zeta, \omega) T'_{sl}(\xi, \zeta) \exp [i2h\beta_1] \quad (4.11)$$

for the LS+SL case,

$$\begin{aligned} \Gamma_{ls}(\xi, \zeta, \omega) = & \{ T_{ls}(\xi, \zeta) R_{sl}(\xi, \zeta, \omega) T'_{ll}(\xi, \zeta) \\ & + T_{ll}(\xi, \zeta) R_{ls}(\xi, \zeta, \omega) T'_{sl}(\xi, \zeta) \} \exp [ih(\alpha_1 + \beta_1)] \end{aligned} \quad (4.12)$$

and for the LL case,

$$\Gamma_{ll}(\xi, \zeta, \omega) = T_{ll}(\xi, \zeta) R_{ll}(\xi, \zeta, \omega) T'_{ll}(\xi, \zeta) \exp [i2h\alpha_1] \quad (4.13)$$

In Eqs. 4.10-4.13, the exponentials correspond to the phase terms due to travel in the adherend, α_1 is the vertical wave number of longitudinal wave in the adherend, β_1 is the vertical wave number of shear wave in the adherend, h is the adherend thickness, T and T' represent the transmission coefficients at the water-aluminum and aluminum-water interfaces, respectively (Appendix B), and R represents the oblique-incidence plane-wave reflection coefficient at the interfacial region (Section 4.1.2), which carries the information regarding the integrity of the interfacial region.

The field due to any combination of the three types of reflection or multiple reflections may be found by simple superposition. The present approach involves the calculation of the plane wave reflection and transmission coefficients at various interfaces, which are numerically well behaved and amenable to very fast computation. In addition, the frequency domain representation of any specific wave type, or a combination of the wave types may be calculated directly.

The multi-layered model is the best choice if the spectrum due to all the wave modes, including multiple reflections, is sought. In this case, the function Γ in Eq. 4.10 is the plane wave reflection spectrum of the multi-layered structure.

4.2.2.3 Signal spectrum at the receiver

In order to predict the signal captured by the receiver, the effect of the receiver

characteristics on the signal must be modelled. The receiver voltage may be found by integrating the reflected wave potential (Eq. 4.10) over the receiver aperture, after multiplying by the appropriate phase transformation term in accordance with the thin lens model for focused receivers. The signal at the receiver is given by, in the receiver coordinates:

$$S_{mn}(0, 0, \omega) = \int_{-\infty}^{\infty} \int_{-\infty}^{\infty} \phi_r^{mn}(x_r, y, 0, \omega) P_r(x_r, y) \exp \left[-ik_w F_r \left(1 - \sqrt{1 - \frac{x_r^2 + y^2}{F_r^2}} \right) \right] dx_r dy \quad (4.14)$$

where $P_r(x_r, y)$ is the aperture function for the receiver, F_r is the focal length of the receiver in water. The final expression for the signal, in the specimen co-ordinates, may be obtained by substituting Eq. 4.10 into Eq. 4.14, yielding:

$$S_{mn}(L_h, -L_v, \omega) = \int_{-k_w}^{k_w} \int_{-k_w}^{k_w} A_e(\xi \cos \theta - \alpha \sin \theta, \zeta, \omega) A_r(\xi \cos \theta - \alpha \sin \theta, \zeta, \omega) \Gamma_{mn}(\xi, \zeta, \omega) \exp [2i(\xi L_h + \alpha L_v)] \frac{(\alpha \cos \theta + \xi \sin \theta)}{\alpha} d\xi d\zeta \quad (4.15)$$

where A_r is the angular spectrum of the receiver. For two identical transducers positioned symmetrically, the angular spectrums A_e and A_r are identical. For a cylindrically focused system, the two-dimensional version of the above should be employed, i.e.:

$$S_{mn}(L_h, -L_v, \omega) = \int_{-k_w}^{k_w} A_e(\xi \cos \theta - \alpha \sin \theta, \omega) A_r(\xi \cos \theta - \alpha \sin \theta, \omega) \Gamma_{mn}(\xi, \omega) \exp [2i(\xi L_h + \alpha L_v)] \frac{(\alpha \cos \theta + \xi \sin \theta)}{\alpha} d\xi \quad (4.16)$$

4.2.2.4 Normalization spectrum

In experimental work, the signal spectrum of interest is commonly normalized with

respect to a reference spectrum in order to de-convolve the inherent frequency response of the transducers. The obvious choice for the normalization spectrum is the front-wall signal (Fig. 4.6a), since it is independent of the adhesive/adherend interfacial properties and can be readily measured for the same specimen on which the interfacial echoes are measured. Since the front-wall signal and the interfacial signals undergo different amounts of diffraction, it is important to calculate the normalized theoretical spectrum, S_{mn}/S_{fw} , when comparing theory and experiments, where S_{fw} is the spectrum of the front-wall signal, given by:

$$S_{fw}(F \sin \theta, -F \cos \theta, \omega) = \int_{-k_w}^{k_w} \int_{-k_w}^{k_w} A_e(\xi \cos \theta - \alpha \sin \theta, \zeta) A_r(\xi \cos \theta - \alpha \sin \theta, \zeta) R_{fw}(\xi, \zeta) \exp[2i[\xi L_h + \alpha L_v]] \frac{(\alpha \cos \theta + \xi \sin \theta)}{\alpha} d\xi d\zeta \quad (4.17)$$

where R_{fw} is the plane-wave reflection coefficient at the front wall.

4.2.2.5 Time domain echoes

If the time domain echoes, $S_{mn}(L_h, -L_v, t)$, were to be calculated, the signal spectrum (Eq. 4.15) may be multiplied by the measured frequency response of the probe-pair, $H(\omega)$, and then an inverse temporal Fourier transform may be performed:

$$S_{mn}(L_h, -L_v, t) = \frac{1}{2\pi} \int_{-\infty}^{\infty} S_{mn}(L_h, -L_v, \omega) H(\omega) e^{-i\omega t} d\omega \quad (4.18)$$

4.2.2.6 Attenuation

The frequency dependant attenuation in the propagating media may influence the measured signals appreciably. In the present case, the interfacial echoes travel in water and the metallic adherend. The attenuation within the adherend may be safely neglected because of the relatively low attenuation in metals, and the smaller travel path. However, the attenuation in the water can be substantial, especially at higher frequencies, since the water path is

relatively long. A simple method to account for the attenuation is to make the wave number complex [69]:

$$k = k_r + ik_i \quad (4.19)$$

where $k_r = \omega/c$, c being the wave velocity in the propagation medium, and k_i is the attenuation coefficient in the medium in Nepers per meter. The attenuation coefficient in water as a function of frequency, f , and temperature, T , is well known [89], and is given by:

$$k_i = 0.025 [1 - 0.031 (T - 20)] f^2 \quad \text{Np/m} \quad (4.20)$$

4.2.3 Numerical implementation

The calculation of the signal spectrum is numerically intensive, although the present formulation of the problem resulted in significant numerical advantages compared to the conventional multi-layered approach. The major step in the numerical implementation is the calculation of the angular spectrum (Eq. 4.6) for each frequency. Spherically focused systems require the evaluation of double integrals (three dimensional problem), which is numerically demanding. Spatial Fast Fourier Transforms (FFT) are the best way to calculate the angular spectrums in such a situation. In the two-dimensional case (cylindrically focused transducers), the calculation of the angular spectrum involves the evaluation of a single integral, and standard numerical integration procedures are quite sufficient. Additional simplification is achieved if the transmitter and the receiver have identical characteristics, in which case only one angular spectrum needs to be evaluated.

Calculation of the function G (Eq. 4.11-4.13) is numerically straightforward. The final step is to evaluate the integral Eq. 4.15 for each frequency and L_v , which involves a double integration for a spherically focused system or a single integration for a cylindrically focused system. Again, a spatial FFT algorithm is preferred for 3-D problems, while numerical integration procedures are satisfactory for 2-D problems. A Matlab code was written to implement the numerical solution scheme for a cylindrically focused system.

4.2.4 Numerical simulations

In this section, a theoretical simulation of the response of the focused wave measurement system from a typical adhesive joint is given. The transmitter and the receiver are assumed to have identical characteristics with a cylindrical focus. The material properties used are given in Table 4.1, and the thickness of the aluminum was 1.6 mm, typical of aluminum sheets used in the aerospace industry. The wave velocity and attenuation of water were determined from the temperature [89], which was assumed to be 23°C .

4.2.4.1 Comparison of *resolved* and *multi-layered* approaches

In this subsection, the new resolved formulation for predicting the interfacial signals received by the system is compared with the conventional multi-layered approach. For this purpose, a nominal incident angle of 16° and an aperture angle of 24° were chosen. Although the nominal incident angle of the transmitter is greater than the first critical angle of the water-aluminum interface (14°), both longitudinal and shear waves will be generated inside the adherend because of the relatively large aperture angle.

Figure 4.7a and 4.7b show the predicted time domain signals from the joint, using Eq. 4.15 along with Eq. 4.17, for the resolved and multi-layered, respectively. These signals correspond to the case where the shear wave is focused ($d = 4.5$ mm, where $d = F\cos\theta - L_v$, is the distance by which the probe-pair is moved downwards to the specimen from a front-wall focused position, see Fig. 4.6) at the interfacial region. For case (a), the superposition principle was employed to calculate the combined spectrum of the three primary back-wall wave types: SS, LS+SL and LL (Eq. 4.11-4.13). For case (b), the reflection spectrum of the entire plate was calculated using the global matrix approach (Section 2.4.4).

By comparing the three pairs of primary interfacial echoes (LL, LS+SL and SS) in Fig. 4.7a and 4.7b, it may be observed that there is excellent agreement between the resolved and the multi-layered approaches. The computational time for case (a) was less than 10% of that for case (b). If only one of the echoes, such as SS, is required, as is the case in most practical applications, the computational effort for the resolved formulation is further reduced.

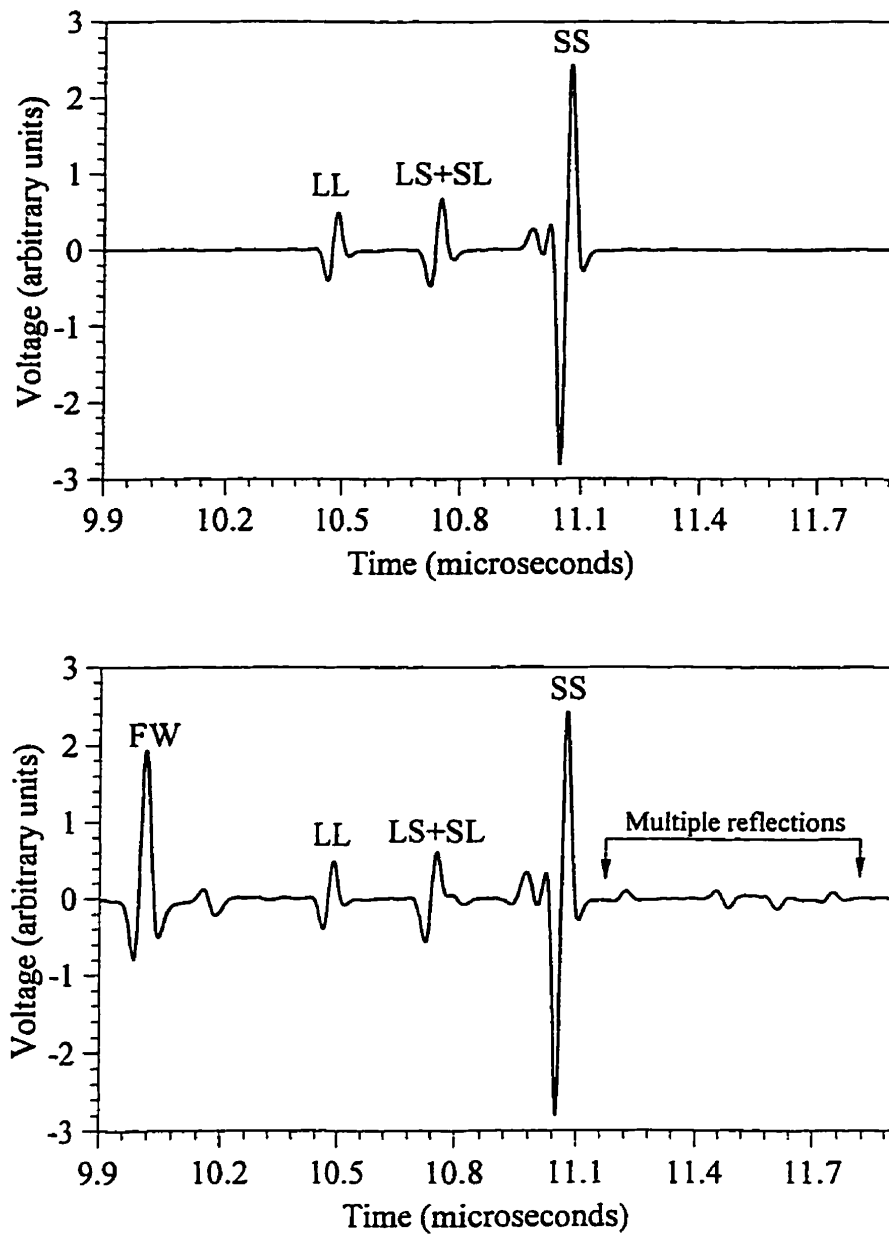


Figure 4.7: Predicted time domain echoes when the shear-shear (SS) reflection is focused at the interfacial region, using, (a) the new resolved approach, and (b) the conventional multi-layered approach. A perfect interface was assumed in the calculations.

4.2.4.2 Focused-beam interaction with the interfacial region

As the transducer-pair is moved towards the specimen from the front-wall focused position, the first echo to be focused at the interfacial region is the shear-shear (SS) echo, because of the lower velocity of the shear waves as compared to longitudinal waves, followed by the LS+SL echo and then the LL echo. It may be recalled that the SS reflection is the most suitable type for the inspection of the interfacial region. In this subsection, the shear-shear reflection from the adhesive/adherend interfacial region received by the focused wave measurement system is analyzed, using the spring model to describe the interfacial region.

It is preferred to have the nominal incident angle of the transmitter in water above the first critical angle, θ_{cr} , (14° for water-aluminum interface) of the front-wall of the adherend. This is because, (i) the mode-conversion of the longitudinal wave in water into a shear wave in the aluminum is very efficient at angles greater than θ_{cr} , and, (ii) at angles above θ_{cr} , only shear waves are generated inside the adherend, thereby simplifying echo identification. A nominal incident angle in water of 18° , and an aperture angle of 12° were chosen for the simulation.

Figures 4.8a and 4.8b give the magnitude spectrum of the SS reflection from the interfacial region for various values of the spring constants at two positions of the probe-pair relative to the specimen; namely, where the shear wave is focused ($d = 4.5$ mm) and a de-focused position ($d = 6.0$ mm). The frequency range was chosen to reflect practical situations. The results are shown for spring constants ranging from a perfect bond ($K_n = K_t \rightarrow \infty$) to a debond ($K_n = K_t \rightarrow 0$). For the intermediate values of the spring constants, it has been assumed that $K_n/K_t = 4$, based on measurements on a fresh bond.

It is observed from Fig. 4.8 that under the de-focused condition ($d = 6.0$ mm), the frequency spectrum shows an interference pattern. This phenomenon may be explained by the interaction of the various angular components of the focused beam. For a given probe-pair and material properties, the signal amplitude depends on the relative phases of the angular components. The phase depends on the frequency and the time of flight of the angular components (in other words the path lengths of the angular components, determined by the

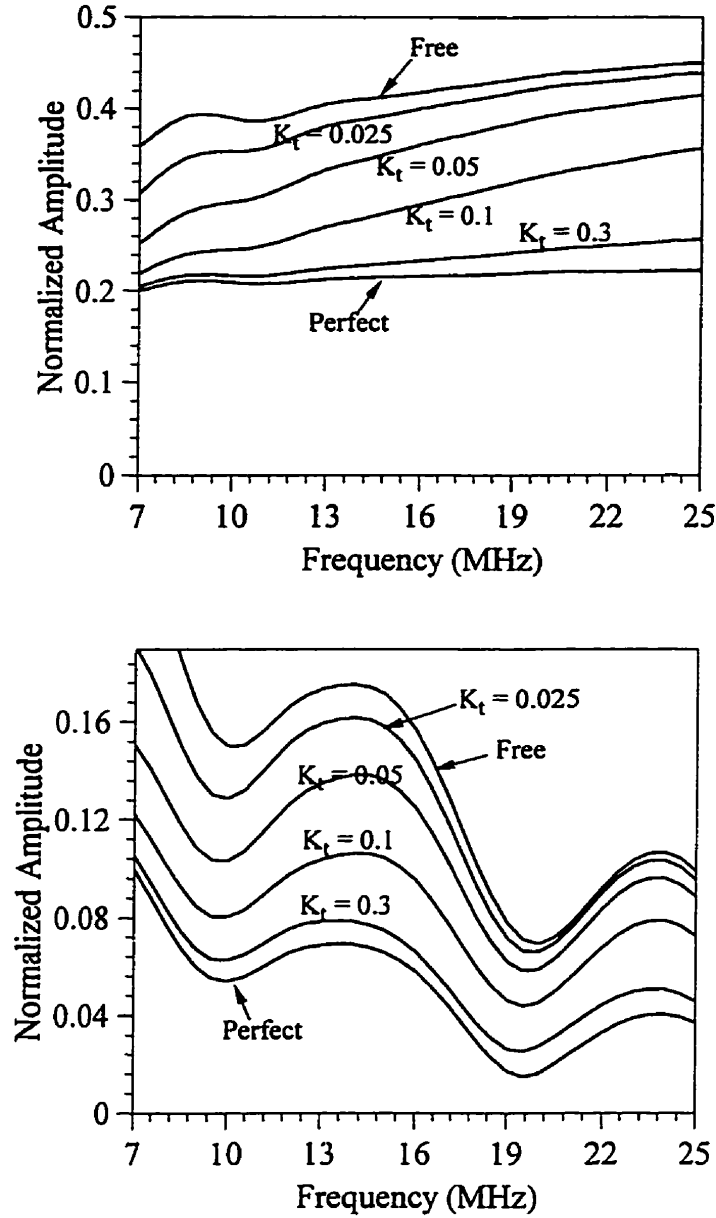


Figure 4.8: Normalized amplitude spectra of shear-shear (SS) reflection from the interfacial region for various values of the spring constants, at, (a) focused position, $d = 4.5$ mm, (b) de-focused position, $d = 6.0$ mm. It has been assumed that the ratio, K_d/K_p , is fixed at 4.0.

relative distance of the probe-pair with respect to a given specimen; Fig. 4.6). When the displacement d (Fig. 4.6) is such that the phases of the various angular components are approximately equal, the amplitudes of the angular components add constructively for all frequencies, and the interaction of the angular components is largely independent of

frequency. The signal attains maximum strength at this position; this situation was found to occur at about $d = 4.5$ mm for the present case. However, when d is such that the path length differences, and hence the relative phases, of the angular components are substantial, the interaction of the angular components becomes frequency dependent. This gives rise to an interference pattern in the magnitude spectrum of the signal (Fig. 4.8b).

It is observed from Fig. 4.8 that the sensitivity of the shear waves to the spring constants (i.e. change in amplitude with change in the spring constants) generally increases under the de-focused condition (Fig. 4.8b) compared to the focused position (Fig. 4.8a), especially for relatively small values of the spring constants. This increased sensitivity may be explained by the interaction of the angular components of the focused beam depending on d , explained above.

4.2.4.3 Sensitivity to adhesive and adherend properties

It should be emphasized that the interfacial characterization of adhesive joints involves the detection of rather subtle changes in a thin region embedded between the adhesive and the adherend. The inspection of the interfacial region must be performed via the top adherend; hence even small changes in the adherend properties may significantly alter the amplitude spectrum of waves reflected from the interfacial region. The amplitude spectrum depends to some extent on adhesive properties as well. It may be recalled (Section 2.2.2) that, as a result of environmental degradation, the bulk adhesive may undergo changes, in addition to the interfacial region.

The sensitivity of the SS reflection to typical perturbations in the bulk adhesive properties is assessed in Fig. 4.9, which shows the change in the amplitude spectrum at the focused condition when the bulk adhesive longitudinal wave velocity increased by 10%. It was assumed that the interface is a perfect bond. The amplitude is observed to drop as a result of increased velocity. Such changes in the amplitude spectrum can not be ignored when small changes in the spring constants are being evaluated (Fig. 4.8). Similar results were obtained for the de-focused position, except that the dips in the amplitude spectrum show relatively higher sensitivity to adhesive properties.

Figures 4.10a and 4.10b give the change in the amplitude spectrum when the adherend shear wave velocity was increased by 1% for the focused and de-focused cases respectively. For the focused position (Fig. 4.10a), the spectrum is practically insensitive to adherend properties at low frequencies, while at high frequencies, the spectrum does show a slight change. Under the de-focused condition (Fig. 4.10b), the amplitude spectrum is observed to undergo substantial changes, especially the position of the peaks and dips. Therefore, in practice, the focused position is preferable for the interfacial characterization, although it shows smaller sensitivity to the spring constants compared to the de-focused position (Fig. 4.8).

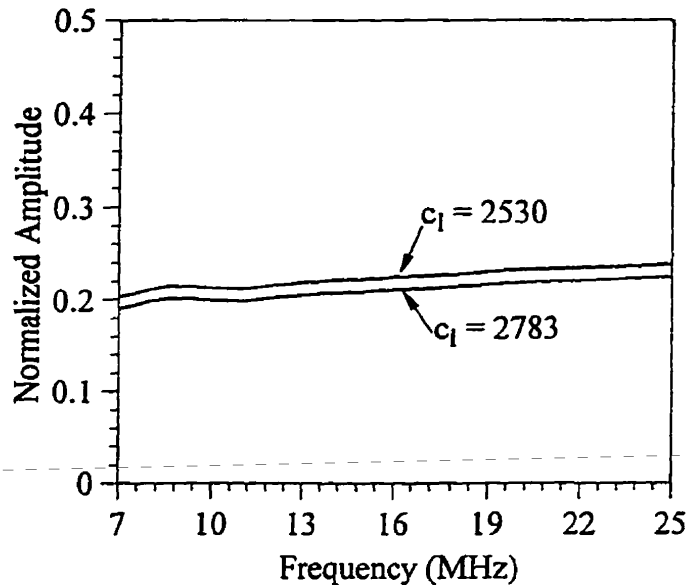


Figure 4.9: Effect of a 10% change in the adhesive longitudinal wave velocity on the amplitude spectrum of SS reflection at focused position.

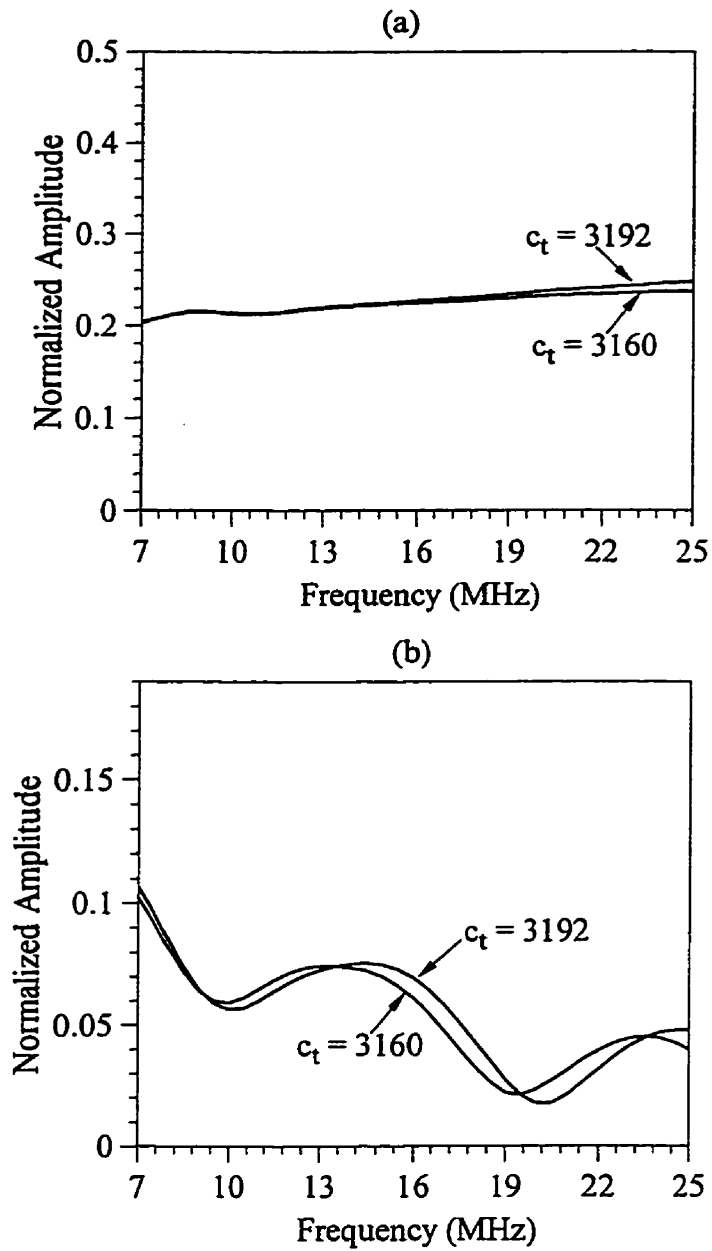


Figure 4.10: Effect of a 1% change in the adherend shear wave velocity on the amplitude spectrum of the SS reflection, at (a) focused position ($d = 4.5$ mm) and (b) De-focused position ($d = 6.0$ mm).

This chapter gives the various experimental methods employed in this work. First, an open-faced specimen geometry for durability experiments is introduced, followed by the details of the specimen preparation. The peel test procedure for the new specimen geometry is given next. Methods for measuring the normal-incidence, longitudinal and shear wave reflection coefficients from the adhesive/adherend interfacial region are described. Finally, the design and construction of a novel oblique incidence, cylindrically focused transducer for the inspection of the adhesive/adherend interfacial region is given [87].

5.1 Durability experiments

5.1.1 The open-faced specimen

It may be recalled (Section 2.2.2), that the existing specimen geometry is inadequate to study the time-dependant degradation of structural adhesive joints corresponding to a specific exposure condition. In order to overcome the drawbacks of the traditional geometry (Fig. 5.1a), an open-faced specimen (Fig. 5.1b) is proposed. In an open-faced joint, the adhesive is bonded to only one adherend, leaving the other face exposed. Since the adhesive thickness

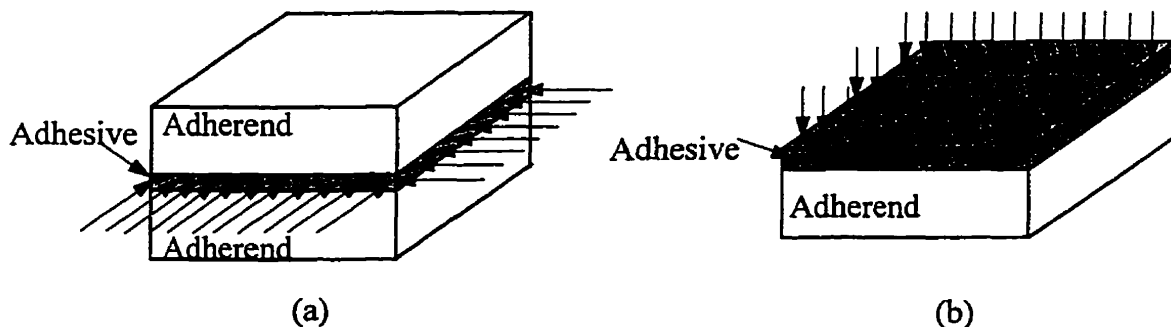


Figure 5.1: Schematic of moisture diffusion into, (a) the traditional geometry, and (b) the open-faced geometry.

offers a much shorter water diffusion path, the time for water uptake is greatly decreased in the case of the open-faced joint, and equilibrium with a controlled environment can be achieved in a relatively short time. An added advantage of the open-faced specimen is that it allows *wet* (as conditioned) and *dry* (after drying out the absorbed water) testing of joint strength.

5.1.2 Materials and specimen preparation

5.1.2.1 Materials

It may be recalled that the plastic dissipation effects are kept small in the peel test if the adherend material is of relatively low yield strength and thickness (Chapter 3). For this reason, the AA1100 series, which has a relatively low yield strength, was chosen as the aluminum alloy for the present work. The thin adherend has the added advantage that the peel failure path is close to the interfacial region, making it suitable for interfacial characterization.

Peel specimens were made using 0.12 mm thick AA1100-O alloy (yield strength of about 50 MPa) as the flexible adherend. The aluminum thickness for the ultrasonic specimens was 1.6 mm (Fig. 5.2b); typical of aerospace applications. For adherends much thinner than 1.6 mm, prohibitively high frequencies (> 25 MHz central frequency) would be required to resolve the interfacial signals from the front-wall signal. The aluminium alloy chosen for ultrasonic experiments was AA1100-H14, which differs from AA1100-O only in the temper.

Two commercial adhesives, representing two different classes of epoxy adhesive, were studied; Permabond E04 epoxy adhesive, which is a two-part, room temperature-curing system, and Hysol EA9346 epoxy adhesive, which is a one-part heat-curing system.

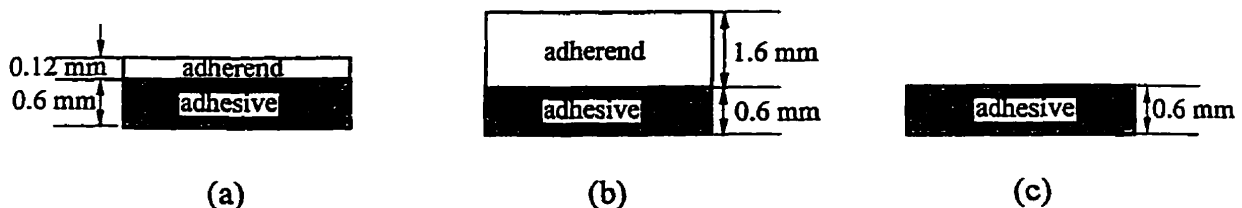


Figure 5.2: Schematic of the specimens for, (a) peel tests, (b) ultrasonic tests, and, (c) tensile tests and moisture diffusion studies

5.1.2.2 Specimen preparation

The adherend surface preparation (pretreatment) for both the peel and ultrasonic specimens was the Forest Products Laboratory (FPL) etch procedure (ASTM D-2651), which produces a very thin oxide layer (< 100 nm) on the adherend surface.

Open-faced peel specimens (Fig. 5.2a) were prepared using pretreated flexible adherends (0.12 mm thick, AA1100-O alloy) of size, 100 mm by 80 mm. The adhesive was applied to the adherend, and the uncured joint was clamped between Teflon-coated, 12.7 mm thick steel plates. Teflon shims were used to control the adhesive thickness at 0.60 ± 0.05 mm. The Permabond E04 adhesive was cured at room temperature (25°C) for at least 24 hours. The Hysol EA9346 was cured for 90 minutes in an oven preheated to 120°C , ensuring that the bondline was at 120°C for at least one hour. The specimens were then allowed to cool to room temperature. The open-faced ultrasonic specimens (Fig. 5.2b) were prepared in an identical manner using the 1.6 mm thick AA1100-H14 aluminum alloy.

Cast bulk adhesive specimens (Fig. 5.2c) for tensile tests and moisture diffusion studies were prepared by curing the adhesive between two Teflon-coated steel plates. Teflon shims were used to control the thickness of the cast specimens at 0.60 ± 0.05 mm.

5.1.3 Aging: wet and dry specimens

The open-faced peel and ultrasonic specimens were immersed in de-ionized water at $67 \pm 3^{\circ}\text{C}$, and periodically removed in order to investigate various levels of degradation. An important aspect of the present work was to investigate the *wet* (as conditioned) and dry (after drying out the absorbed water) tests in order to distinguish between the reversible and permanent effects of water on the joint. The specimens for *dry* testing were kept under vacuum at 70°C for 3 days after removal from the water, in order to dry out the absorbed water.

The cast adhesive specimens for the tensile tests were subjected to the same environment at $67 \pm 3^{\circ}\text{C}$, and tested for various levels of exposure for both the dry and wet cases. Water diffusion studies were also conducted by measuring the mass uptake of water by the cast

adhesive specimens as a function of duration of immersion in water at $67 \pm 3^\circ\text{C}$.

5.2 Destructive testing

5.2.1 Peel tests

In order to facilitate the peel testing of the open-faced specimens after degradation, the exposed face of the adhesive was bonded to a 1.6 mm thick, rigid plate by means of the room temperature-curing, Permabond E04 adhesive (Fig. 5.3). The secondary bondline thickness was kept to less than 0.1 mm. It should be mentioned that the use of thin adherend (0.12 mm thick) ensured that the secondary bond had practically no effect on the measured peel force.

The open adhesive faces of the specimens that were selected for *wet* testing were secondary-bonded immediately after removal from the water bath. Similar secondary bonding was done on the *dry* specimens, after drying out the absorbed water. The final step was to cut these wet and dry specimens into strips, at least 15 mm wide, for peel testing.

Figure 5.4 shows the test apparatus for peel testing at an angle of 45° . The peel specimen was clamped on the 45° angle block, and the flexible adherend was held using a friction grip. The grip was connected to a long (about 60 cm) flexible steel wire, which was attached to the crosshead of an Instron-1000 machine at the other end. The long steel cable ensured that the peel angle was kept to $45 \pm 3^\circ$ when the flexible adherend was peeled from the adhesive.

The peel testing was conducted at a rate of 5 mm per minute, and the flexible adherend was peeled from the adhesive for a length of at least 50 mm. The peel force data was collected

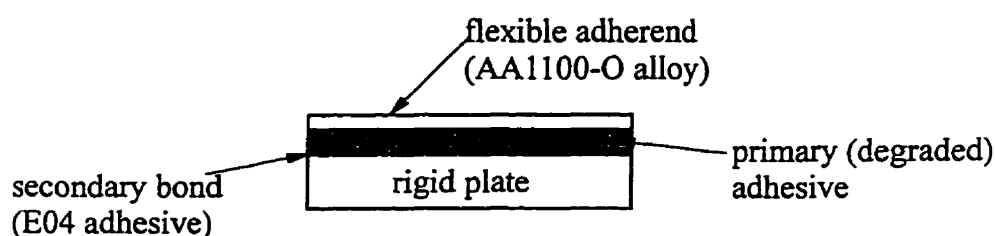


Figure 5.3: Secondary bonding of the open-faced peel specimen

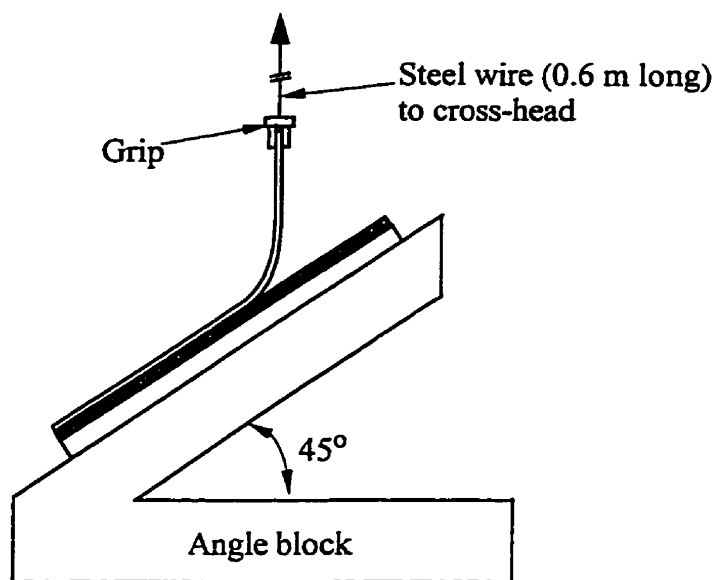


Figure 5.4: Peel test apparatus

by a computerized data acquisition system as the flexible strip was peeled. The final result was in the form of the peel force vs. the cross-head movement (the peel trace). Figure 5.5 shows a typical peel trace from a fresh, Permabond E-04 adhesive joint, after the peel force had reached a steady value. The slight increase in peel force is due the slight change in the peel angle (within 3°) as a function of the cross-head movement. The peel force is usually expressed as the average value of the peel trace per unit width of the specimen.

5.2.2 Failure surface analysis

The peel failure surfaces of fresh and degraded specimens were analyzed using the Scanning Electron Microscope (SEM) operating in the secondary electron (SE) mode, to study the effects of water on the interfacial regions of the joint. In addition, elemental analysis of the surfaces was carried out using energy dispersive spectroscopy (EDS).

5.2.3 Tensile tests

It was described in Chapter 2 (section 2.2.2) that the adhesive may undergo reversible or permanent changes as a result of water absorption. In order to assess the effect of water on the Young's modulus of the adhesive, tensile tests were conducted on fresh and degraded (wet and dry) cast adhesive specimens (Fig. 5.2c). The tensile tests were performed at the same rate as

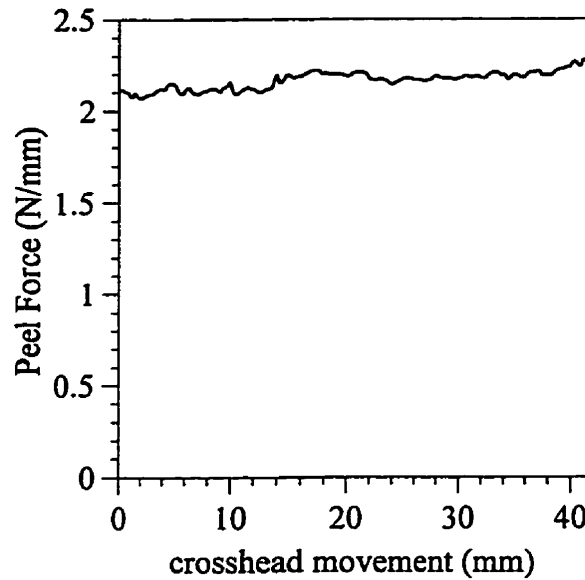


Figure 5.5: Typical peel trace for a fresh specimen

the peel tests, i.e., 5 mm per minute.

5.3 Ultrasonic experiments

5.3.1 Normal-incidence shear reflection coefficient

The measurement of the normal incidence shear wave reflection coefficient from the interfacial region is a relatively difficult task, since a contact method should be used to couple the ultrasound to the sample. Amplitude measurement using a contact method, with the transducer placed directly on the sample, is unreliable, especially for detecting the subtle changes in the reflection coefficient associated with the environmental degradation of adhesive joints. In this section, a new reliable method for the measurement of the plane, shear wave reflection coefficient from the adhesive/adherend interfacial region is described.

5.3.1.1 Principle

The method is based on the use of a buffer rod (or delay line) between the specimen and the transducer (Fig. 5.6a) [90]. Two echoes, one each from the front-wall and the back-wall of the adherend were measured, and the back-wall echo was normalized to the front-wall echo. This normalization procedure is the key to achieving reliable measurements. Most of the

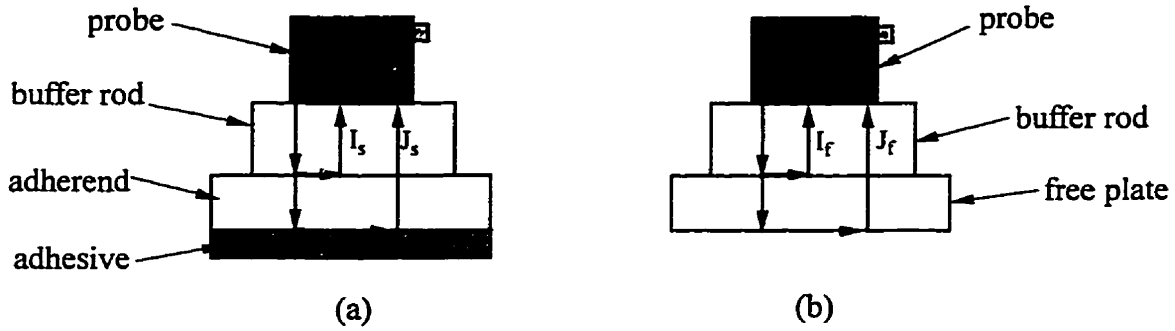


Figure 5.6: Measurement of the plane wave reflection coefficient of normal shear waves: configuration for (a) open-faced specimen, and (b) free plate

variabilities in contact measurements are due to the fact that the electro-mechanical efficiency of the transducer is very sensitive to coupling. Since, both the front and back-wall echoes go through the interface between the probe and the buffer rod, the variabilities associated with the transducer coupling are cancelled in the normalization process. Referring to Fig. 5.6a, the following expressions may be derived for the front and back-wall signals:

$$I_s(\omega) = H(\omega) (1 - R_1(\omega)^2) R_2(\omega) X_1(\omega) \quad (5.1)$$

$$J_s(\omega) = H(\omega) (1 - R_1(\omega)^2) (1 - R_2(\omega)^2) R_{ss}(\omega) X_2(\omega) \quad (5.2)$$

where H is the transducer excitation, R_1 , R_2 and R_{ss} are the reflection coefficients at the transducer-buffer rod interface, buffer rod-specimen interface, and the back-wall (interfacial region) of the adherend respectively, X_1 and X_2 are terms which account for diffraction and attenuation in the buffer rod, and the buffer rod/adherend combination, respectively. The normalization of the back-wall echo with respect to the front-wall echo gives:

$$N_s(\omega) = \frac{J_s(\omega)}{I_s(\omega)} = R_{ss}(\omega) N_f(\omega) \quad (5.3)$$

where

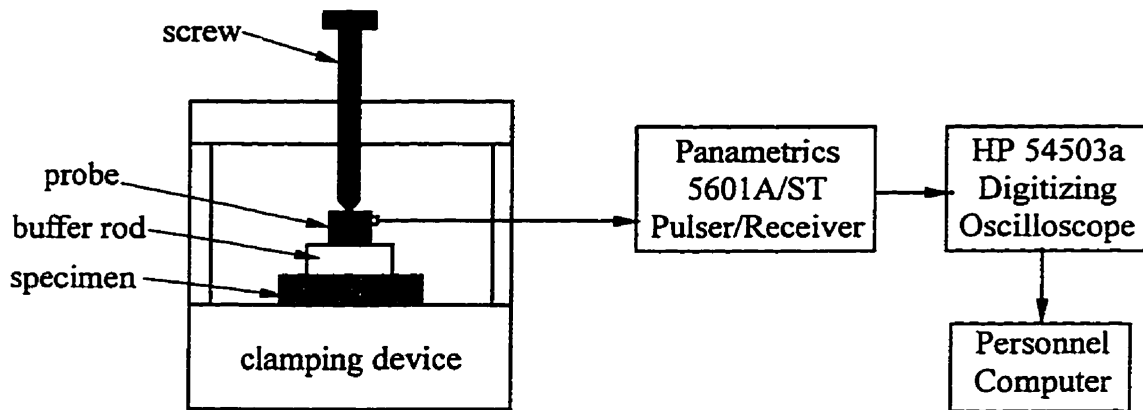


Figure 5.7: Experimental set-up for the measurement of plane-wave reflection coefficient of normal shear waves

$$N_f(\omega) = \frac{X_2(\omega) (1 - R_2(\omega)^2)}{X_1(\omega) R_2(\omega)} \quad (5.4)$$

It is obvious from Eq. 5.3 that for determining R_{ss} , the function N_f is required. In order to evaluate N_f , a similar set of measurements were performed on a free plate (Fig. 5.6b), which was identical to the adherend in the open-faced specimen. The free plate has a reflection coefficient, R_{ss} , of unity at the back-wall, and hence N_f is directly obtained (Eq. 5.3) by the normalization of the back-wall signal with the front-wall signal for the free plate. This assumes that the buffer rod-specimen reflection coefficient (R_2) is the same in both the open-faced specimen and the free plate measurements. It will be shown in the next section that this can be achieved in practice by careful measurements.

5.3.1.2 Implementation

Figure 5.7 shows the schematic of the experimental implementation of the method described in the previous section. The most important requirement is to obtain a repeatable contact between the buffer rod (3 mm thick plexi-glass disc) and the specimen. This was achieved by using Salol (phenyl salicylate) to temporarily bond the buffer rod to the specimen

[90]. Salol is a crystalline material with a melting point of 42°C , which solidifies on cooling to room temperature. The Salol was first melted between the buffer rod and the specimen, and between the probe and the buffer rod, which were then held together with the transducer using a clamping device (Fig. 5.7). After the device was cooled to the room temperature, the liquid Salol layers were solidified by seeding them with a tiny Salol crystallite. The resulting bonding layer were verified to be repeatedly less than $5\text{ }\mu\text{m}$ thick.

The transducer used in the measurements was a contact shear probe with a diameter of 6.3 mm (Krautkraemer: 2914847). It was excited by a high frequency pulser (Panametrics 5601A/ST) which generated a short pulse with a central frequency of 15 MHz, and a bandwidth (6 dB) of 7 - 22 MHz. The reflected pulses (I and J , Fig. 5.6) were received and amplified, sent to a digitizing oscilloscope (HP 54503a), and then to a computer for signal processing. Fast fourier transform algorithm was used to transform the echoes to the frequency domain before processing them using Eq. 5.3-5.4.

The repeatability of experimental procedure was assessed by measuring the function $H_f(\omega)$ (Eq. 5.4) for a 1.6 mm thick, aluminum free-plate. The repeatability of the spectrum was found to within 1.5%.

5.3.2 Normal-incidence longitudinal reflection coefficient

The measurement of the plane-wave reflection coefficient of normally incident longitudinal waves is a relatively easy task since water can be readily used as the coupling medium. The principle of measurement is the same as that of the shear waves except that water column acted as the buffer rod (Fig. 5.8). First, the echo from the interfacial region of the open-faced joint was normalized with respect to the front-wall echo (Fig. 5.8a). In order to measure the *plane* wave reflection coefficients, the wave diffraction and attenuation effects must be eliminated from the normalized signal of the open-faced specimen. This was done by the free-plate measurement shown in Fig. 5.8b, as in the case of shear waves.

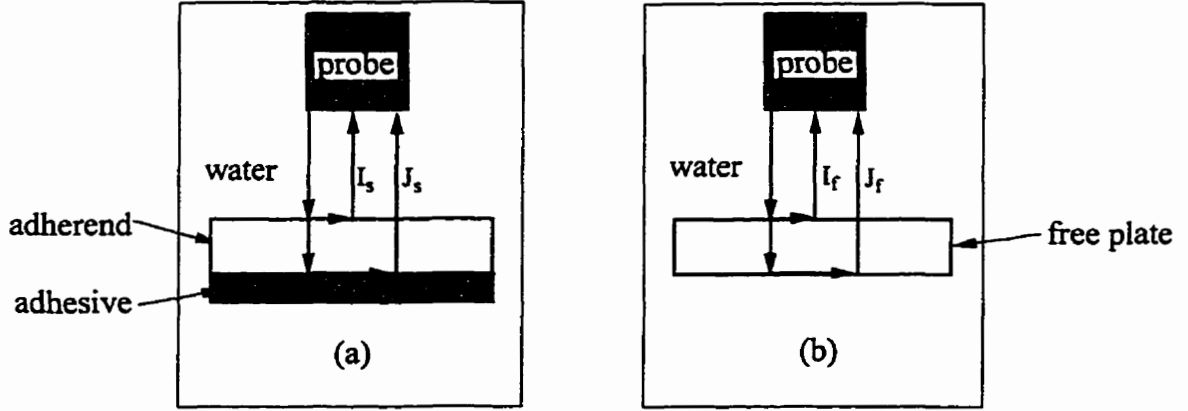


Figure 5.8: Measurement of the plane-wave reflection coefficient of normal longitudinal waves; (a) open-faced joint, (b) free-plate.

The data acquisition system was the same as that for the shear waves (Fig. 5.7). Accurate positioning of the transducer was very important to achieve repeatable results. This was done by using a tilt table to precisely align the transducer normal to the sample surface, and a micrometer for vertical movement.

As in the case of shear waves, the plane-wave reflection coefficient of normal-incidence longitudinal waves, R_{ll} , may be obtained from;

$$R_{ll}(\omega) = \frac{R_{fw} N_s(\omega)}{N_f(\omega)} \quad (5.5)$$

where R_{fw} is the known reflection coefficient at the aluminum-water interface. The signals were processed in the frequency domain using an FFT algorithm.

5.3.3 Oblique incidence measurements

5.3.3.1 Transducer design and construction

A novel transducer for oblique-incidence measurements was developed in the present work. The transducer was made out of polyvinylidene fluoride (PVDF), a polymer piezoelectric material which has become widely popular [91, 92]. The PVDF film used was

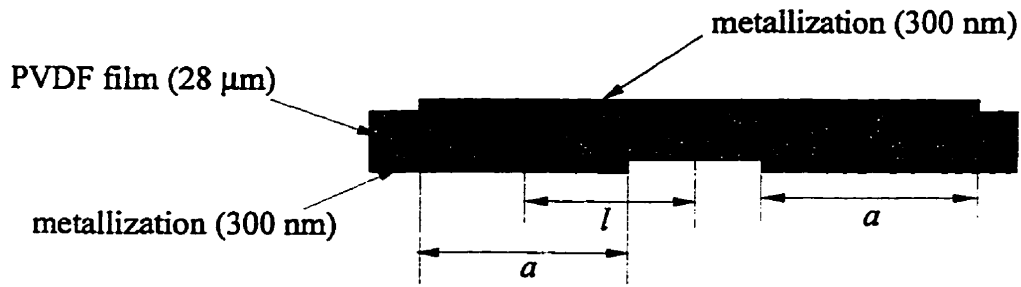


Figure 5.9: Pattern etched on the PVDF film

28 μm thick, with a very thin (300 nm) sputtered metallization (electrodes) covering both sides. A dual-element, oblique incidence, cylindrically focused transducer was manufactured as follows:

The pattern shown in Fig. 5.9 was made on the film by etching away part of the metallization using ferric chloride solution. Two symmetrical active elements were thus formed by the overlapping areas of the metallizations on the two sides of the film (length a in Fig. 5.9). The length l represents the distance from the center of the entire film to the center of each active element. The patterned film was then positioned on a steel half-cylinder such that the two elements were symmetric with respect to a vertical line passing through the center of the half-cylinder. The radius of the half-cylinder was equal to the desired focal length, F .

The active connection was made by bonding a thin wire to the top metallization, in between the two active elements (Fig. 5.10), using a conductive epoxy. A stainless steel case was then placed over the film, and a two-part epoxy resin was poured on top of the film as the backing material. Epoxy was chosen as the backing because it is acoustically well-matched to the PVDF film. The backing was allowed to cure for at least twenty-four hours. Once cured, the half-cylinder was removed, and the active wire attached to a UHF connector as shown in Fig. 5.10. The case acted as the ground, by electrically connecting it to the front face of the film.

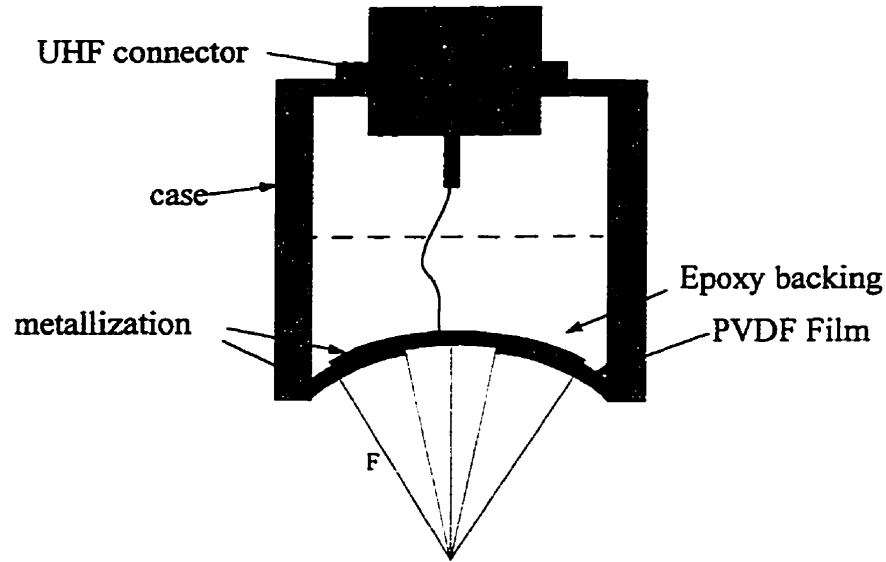


Figure 5.10: Construction of the oblique-incidence transducer

The nominal incident angle and aperture angle of the probe are determined by the focal length, F , and the dimensions of the pattern. The nominal incident angle may be calculated as, $\theta = l/F$ and the aperture angle is given by $\theta_a = a/F$. Here a is the width of each active element, and l is the distance between the center of the entire pattern and the center of each active element (Fig. 5.7). The present probe had the nominal parameters of $\theta = 17.9^\circ$, $\theta_a = 14.3^\circ$ and $F = 24.0 \text{ mm}$.

Figure 5.11 shows the echo recorded by the probe when focused on an aluminum reflector. The probe gives rise to a very broad-band signal with a center frequency of the pulse is about 18 MHz and its 6 dB bandwidth ranges from 7 MHz to 25 MHz . Satisfactory results may be obtained from 7 to 28 MHz .

5.3.3.2 Experimental set up

Figure 5.12 shows the experimental set-up used for oblique incidence measurements. It consisted of a tilt table, that could rotate about two horizontal axes, to precisely align the

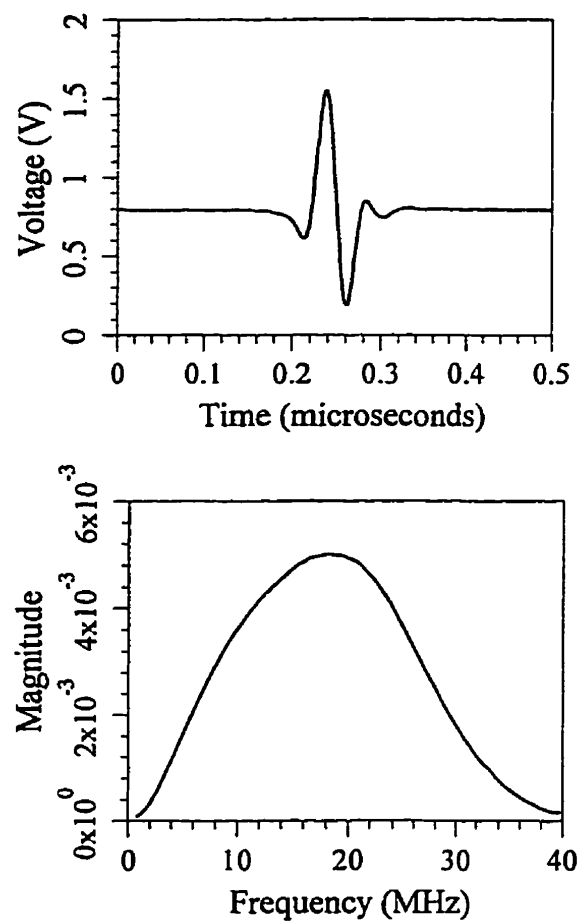


Figure 5.11: Typical signal recorded by the oblique-incidence transducer when focused on an aluminum reflector; (a) time-domain echo, and (b) corresponding frequency spectrum.

transducer normal to the sample. A micrometer was used to move the transducer/tilt table assembly in the vertical (z) direction. The transducer was excited by a Panametrics 5601 A/ST high frequency pulser, which also acted as the receiver/amplifier. The amplified echo was digitized by an HP 54503a oscilloscope and then fed to a personal computer for further analysis.

The transducer was focused at the front-wall first, and the corresponding echo was digitized. The probe was then moved towards the specimen to collect the shear-shear (SS) echo from the interfacial region as a function of d (Fig. 4.6). The echoes were transformed to

the frequency domain by a Fast Fourier Transform (FFT) algorithm. The SS echoes were normalized with respect to the front-wall echo in the frequency domain, in order to deconvolve the frequency response of the transducer from the measured spectrum, and to cancel out any variabilities in the electronics.

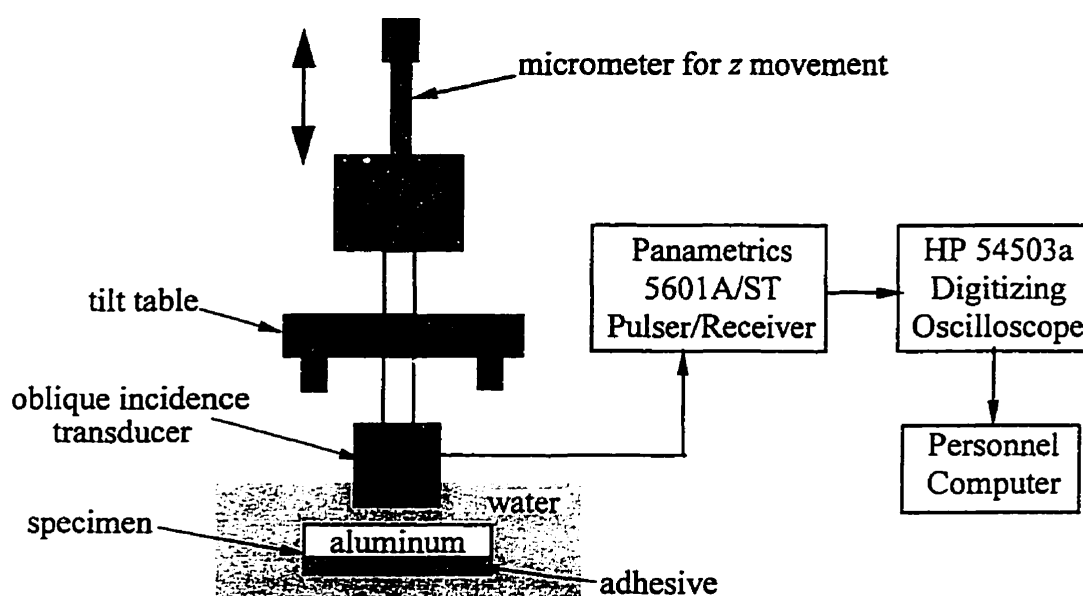


Figure 5.12: Schematic of the experimental set-up for oblique-incidence measurements

This chapter contains the analysis and discussion of the results of the experiments described in Chapter 5. First, the results of the moisture diffusion studies in the adhesive are given, and compared with theory. Next, the destructive test results, comprising the peel tests, tensile tests and surface analysis are given for the two adhesive systems described in Chapter 5. The peel durability data are analyzed using the model developed in Chapter 3. The above destructive results and analysis is based on the author's paper [93]. Finally, the results of the ultrasonic nondestructive measurements are given for both normal and oblique incidence. The nondestructive experimental results are compared with the theoretical models developed in Chapter 4, enabling the determination of the interfacial spring constants as a function of degradation of the joint.

6.1 Water diffusion studies

It may be recalled that water enters a joint mainly by diffusion through the bulk adhesive. This section focuses on the water diffusion characteristics of the adhesives exposed to a specific environment, namely 100% relative humidity at 67°C . It is of interest to predict the time taken by the open-faced joints (Fig. 5.1a) to reach equilibrium with the given conditions.

Figure 6.1 shows the fractional mass uptake by the cast specimens of the two-part adhesive (Permabond E04). It is seen that these specimens do not follow Fick's law [15], according to which the uptake curve should reach the equilibrium after an initial linear stage. Figure 6.1 reveals a relatively slower secondary uptake stage after an initial linear part. After an apparent maximum was reached (at about 240 hours), the weight of the specimens was observed to decrease. The drop in weight may be attributed to the leaching of the adhesive.

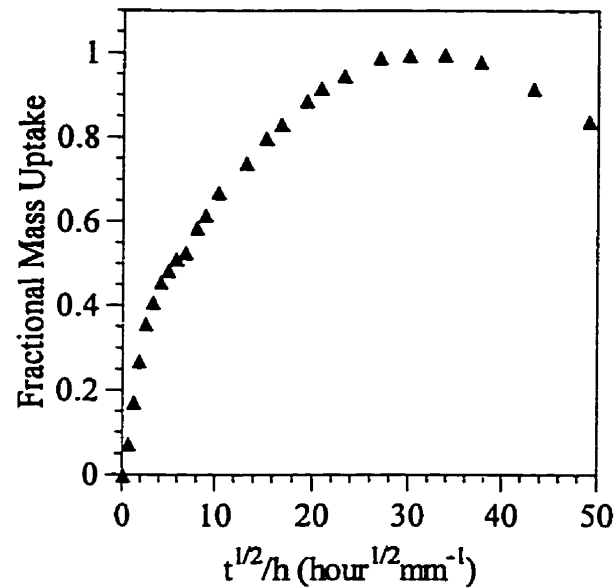


Figure 6.1: Moisture diffusion curve for the two-part (Permabond E04) system; t is the time of exposure, and $h = 0.518$ mm is the adhesive thickness. Each data point corresponds to the average of ten specimens.

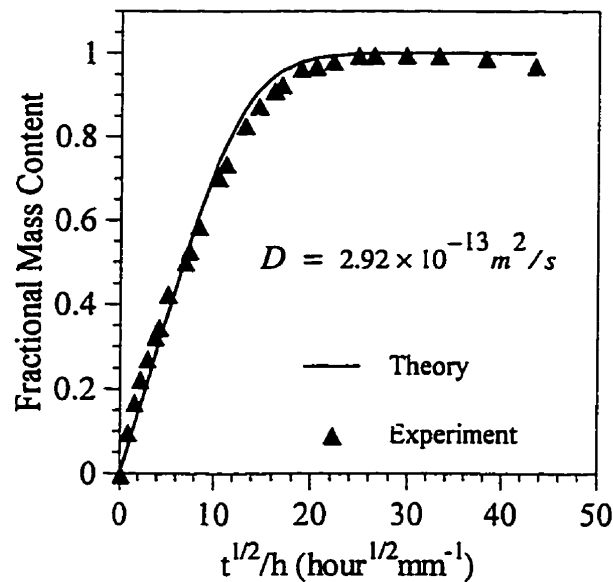


Figure 6.2: Moisture diffusion curve for the one-part (Hysol EA9346) system; t is the time of exposure, and $h = 0.578$ mm, is the adhesive thickness. Diffusion coefficient, D , is determined from Fick's model. Each data point corresponds to the average of six points.

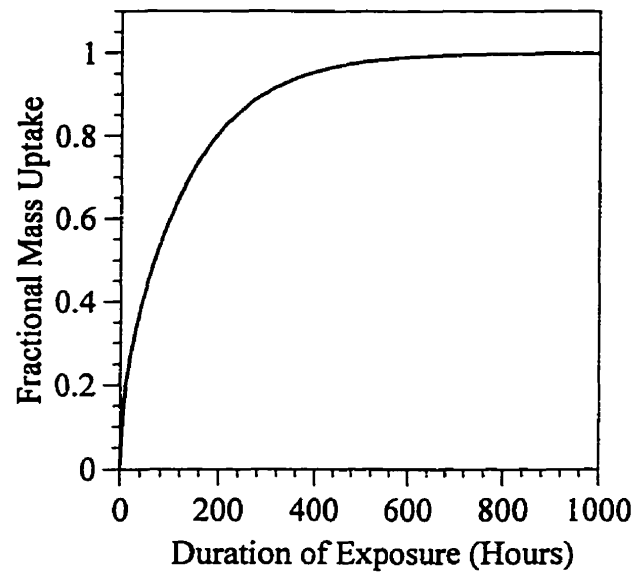


Figure 6.3: Calculated moisture diffusion curve for open-faced joint of the Hysol EA 9346 system. The adhesive thickness was 0.6 mm.

Figure 6.2 shows the diffusion curve of the one-part adhesive (Hysol EA 9346). The theoretical curve was obtained by fitting Fick's model (Appendix C) to the experimental curve using a least-squares method. It may be observed that there is excellent agreement between the theory and the experiments with a diffusion coefficient of $2.92 \times 10^{-13} \text{ m}^2/\text{s}$. The cast adhesive samples reached equilibrium in about 140 hours, and the equilibrium water content was about 5.4% by mass.

From the measured diffusion coefficient for the one-part system, the water diffusion into the open-faced specimen may be predicted using Fick's model. Figure 6.3 shows the calculated fractional moisture content as a function of duration of exposure for a typical open-faced joint. It may be readily observed that the joint reaches equilibrium in about 700 hours (approximately 30 days). In contrast, a typical traditional joint geometry (Fig. 5.1b) would need many years to achieve saturation under the same conditions.

6.2 Destructive test results

6.2.1 Two-part adhesive system (AA1100-O - Permabond E04)

Figures 6.4 and 6.5 respectively, show the measured wet and dry peel force vs. time of exposure for the two-part system (AA1100-O bonded with Permabond E04). Each data point represents the mean of the average peel forces, obtained from the peel traces (Section 5.2.1), of specimens from at least three batches. Figure 6.6 gives the tensile test results for cast Permabond E04 as cured, and in both the wet and dry states after 100 days immersion.

The wet and dry peel results show markedly different behavior, mainly due to the adhesive plasticization in the wet samples. This is evident from Fig. 6.6 where the Young's modulus (defined at 0.5% strain) of the wet adhesive is observed to decrease to 0.22 GPa from an initial value of 0.48 GPa. As a result of plasticization, the fracture mechanism for the wet specimens was primarily cohesive, with large chunks of adhesive present on the flexible strip. For severely degraded wet samples (> 300 days exposure), the amount of residual adhesive on the peel strip was observed to decrease, presumably as the interface became weaker. The peel forces were much higher for the wet case (Fig. 6.4), compared to the dry case (Fig. 6.5), because of the increased crack-tip dissipation due to the cohesive nature of the fracture and the relatively high compliance of the adhesive.

It was therefore apparent that, for the two-part system, after exposure to a moist environment, the peel tests must be carried out in a dry state in order to characterize permanent, interfacial strength degradation. In contrast to the wet case, the failure loci for the fresh and dry cases were close to the interfacial region with a very thin residual adhesive layer on the peel strip. The dry peel force data (Fig. 6.5) indicated considerable degradation only after a long exposure time (> 300 days). However, it is noted from Fig. 6.6 that the adhesive in a dried, degraded condition had become relatively rigid and brittle. Tensile tests were conducted on bulk dry adhesive after 30, 100 and 210 days exposure, and the Young's modulus (defined at 0.5% strain) was found to increase as shown in Table 6.1. The increase in stiffness with degradation may be due to permanent chemical and physical changes in the adhesive associated with exposure to warm water, such as hydrolysis and leaching of some components.

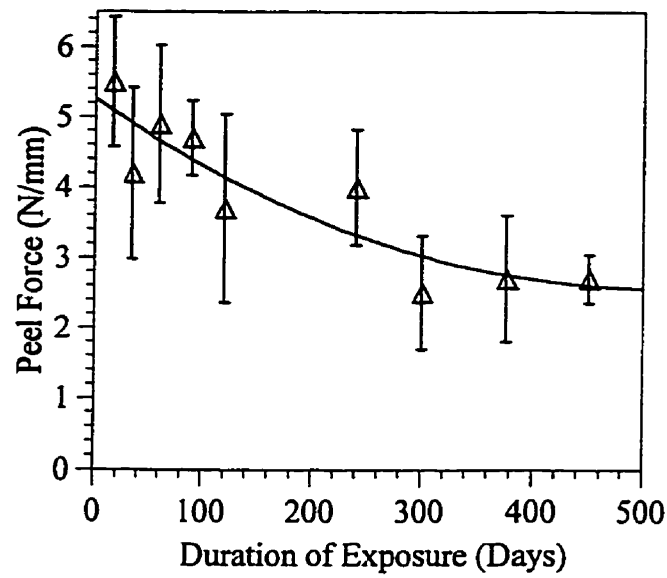


Figure 6.4: Peel force vs. exposure time for two-part (Permabond E04) wet case. The error bars represent one standard deviation each on both sides of the mean value. The curve is a quadratic fit ($r^2 = 0.81$).

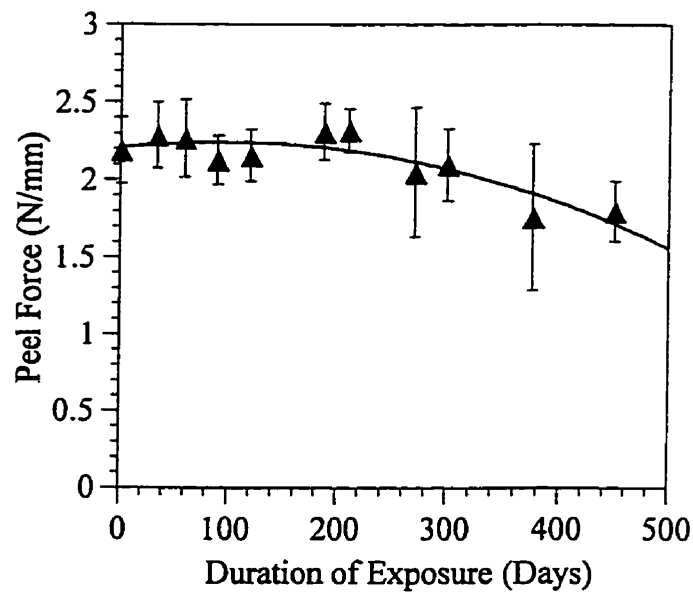


Figure 6.5: Peel force vs. exposure time for two-part (Permabond E04) dry case. The error bars represent one standard deviation each on both sides of the mean value. The curve is a quadratic fit ($r^2 = 0.76$).

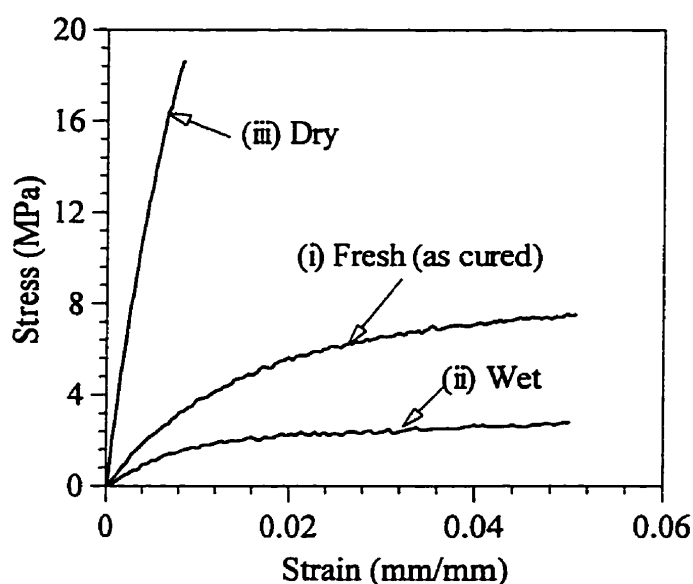


Figure 6.6: Tensile test results for cast two-part adhesive (Permabond E04) tested in three conditions: (i) freshly cured (ii) immersed for 100 days and then tested wet, (iii) immersed for 100 days and then tested dry.

Table 6.1 Tensile test results for the two-part (Permabond E04) system in dry state

Time of exposure of bulk specimen (Days)	Equivalent time of exposure for open-faced specimen (days)	E (GPa)
0	0	0.48
30	60	2.34
100	130	2.50
210	240	2.68

Noting that the plastic dissipation in the flexible adherend increases with an increase in adhesive stiffness (Fig. 3.9), the calculation of the fracture energy must account for the changing adhesive modulus. It should be noted that the adhesive modulus was measured using cast bulk specimens, which saturate more quickly than open-faced specimens with the same adhesive thickness - four times faster according to Fick's model (Appendix C). Therefore, before using the modulus values measured using the cast adhesive specimens to analyze the peel data, the above difference in the rate of moisture uptake has to be taken into account by using an "equivalent" open-faced exposure time. The equivalent open-faced exposure time

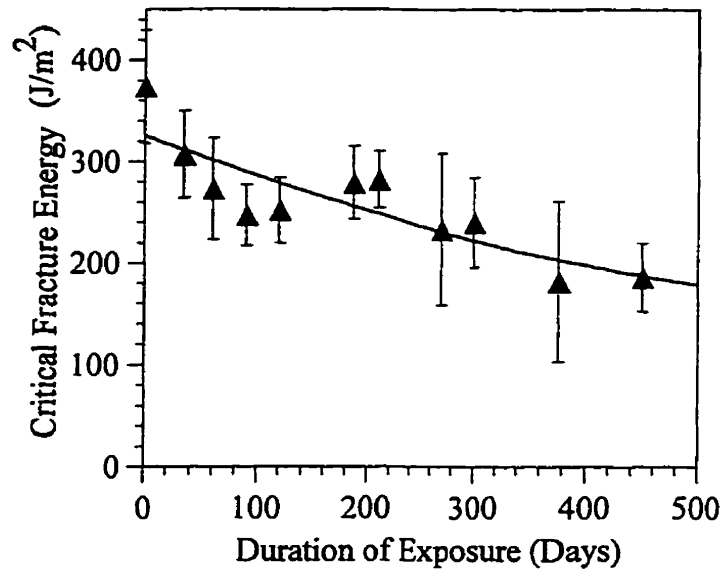


Figure 6.7: Critical fracture energy vs. exposure time for the two-part dry case (peel data of Fig. 6.5). The error bars represent one standard deviation each on both sides of the mean value. The curve is a quadratic fit ($r^2 = 0.72$)

using an “equivalent” open-faced exposure time. The equivalent open-faced exposure time may be obtained by adding the difference between the saturation time of the open-faced and cast specimens (about 30 days in the present case), to the cast-specimen exposure time (Table 6.1). For example, for a cast specimen exposed for 30 days, the equivalent open-faced exposure time is 60 days, while for a cast specimen exposed for 210 days, the equivalent open-faced exposure is 240 days.

Figure 6.7 shows the fracture energy corresponding to the dry peel force data of Fig. 6.5, calculated with the adhesive modulus equal to 0.48 GPa for fresh specimens and 2.50 GPa for all specimens degraded for 2 months or more. The adhesive modulus was assumed to vary linearly for exposure times ranging between 0 to 2 months. In contrast to the trend of Fig. 6.5, the fracture energy is seen to decrease continuously with exposure time.

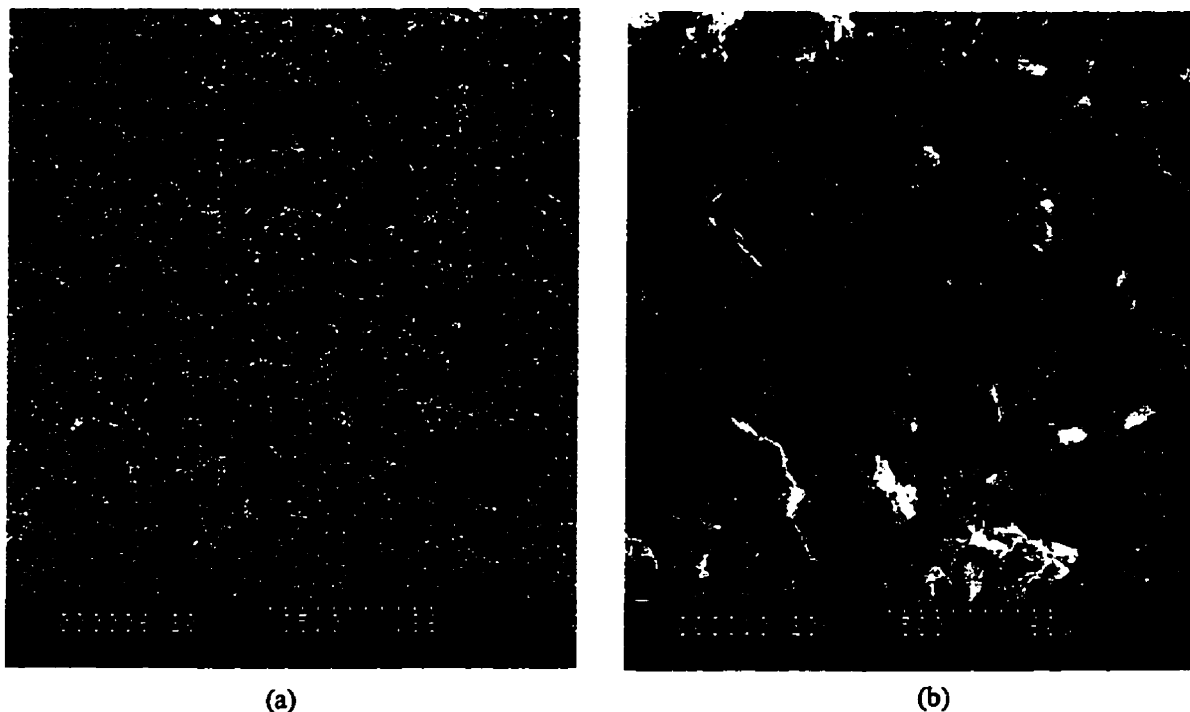


Figure 6.8: SEM micrographs of a fresh specimen of the two-part adhesive at magnifications; (a) 35 times, (b) 500 times

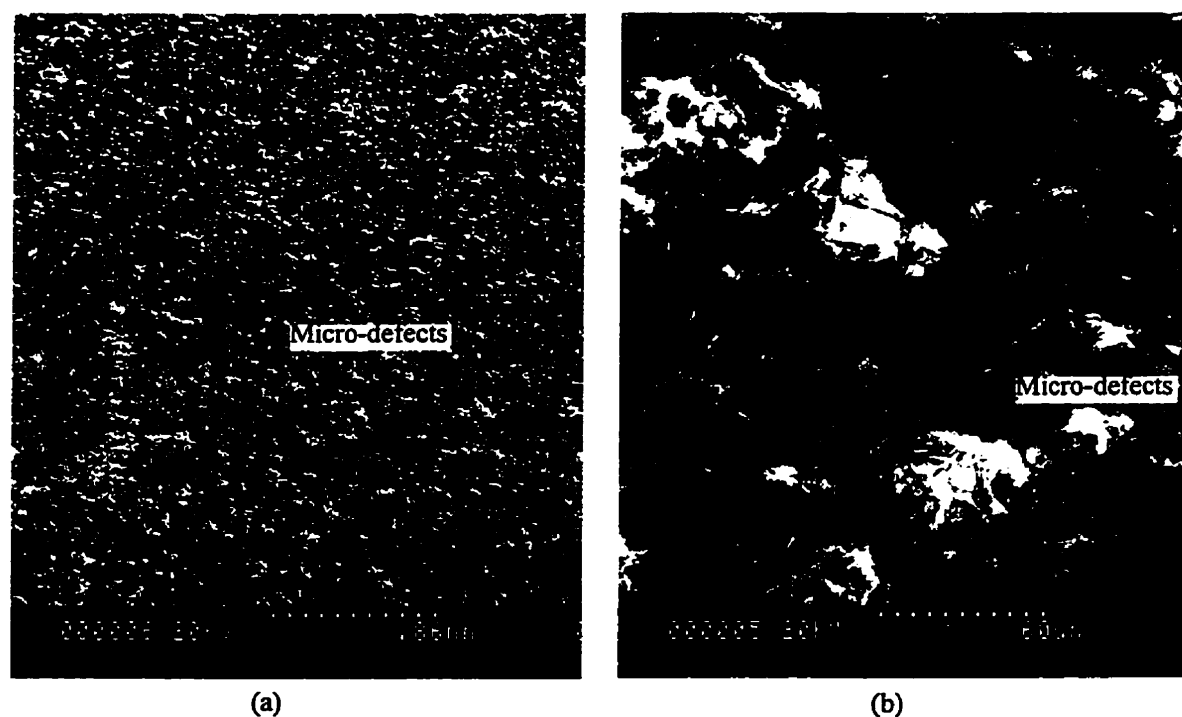


Figure 6.9: SEM micrographs of a degraded specimen (376 days) of the two-part adhesive at magnifications; (a) 35 times, (b) 500 times

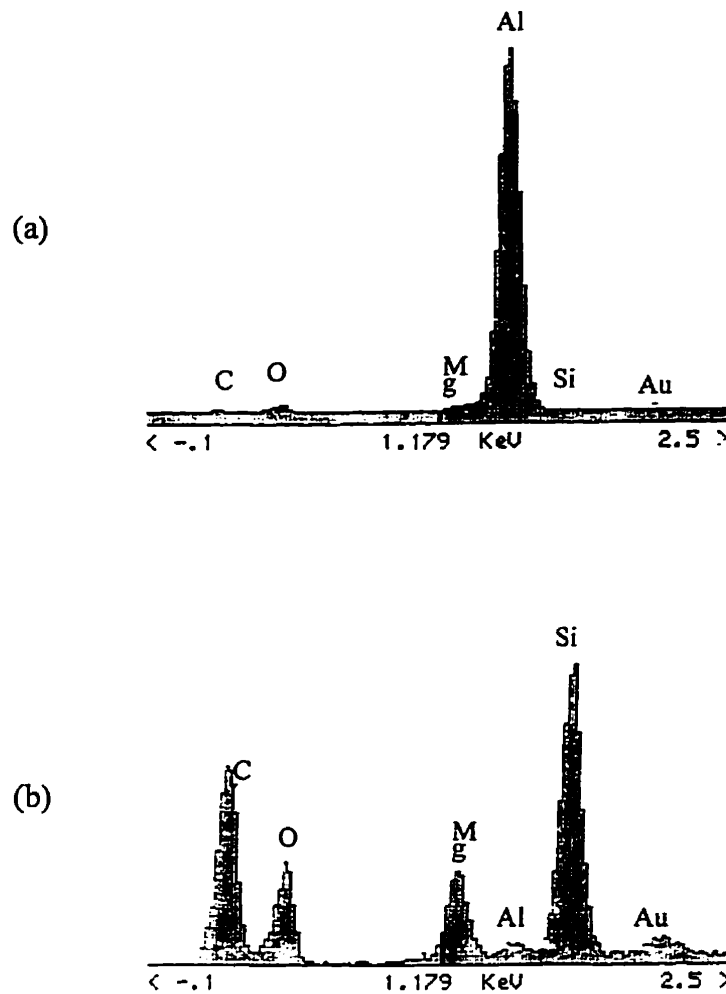


Figure 6.10: X-ray spectrum at, (a) a micro-defect site, and (b) a defect-free site of the specimen in Fig. 6.9.

Analysis of the failure surfaces of the fresh and degraded (dry) specimens was carried out using the SEM. An interesting observation was the formation of micro-defects on the flexible adherend surfaces of the degraded specimens. Figures 6.8a and 6.8b show the SEM micrographs of the adherend surface of a fresh specimen of the two-part system, and Figs. 6.9a and 6.9b show the corresponding micrographs of a dry specimen after 376 days exposure.

The micro-defect formation is visible on the degraded sample. Energy Dispersion Spectroscopy (EDX) showed (Fig. 6.10) only a strong aluminum peak at the defect sites, indicating a complete debond, while the defect-free sites showed mainly the presence of carbon, oxygen, magnesium and silicon. The micro-debonds were found to be between 30 - 150 μm in size, and were consistently evident on specimens after about 300 days exposure. They were also evident to a lesser degree on some specimens degraded for less than 300 days. The distribution of micro-debonds was nonuniform in all cases.

It is noted that there is appreciable scatter in the peel data for degraded specimens as shown by the standard deviation bars. The wet data (Fig. 6.4) showed considerably more scatter within the peel trace than did the dry data (Fig. 6.5), a phenomenon which can be attributed to the cohesive fracture mechanism. The dry data showed relatively greater variability for samples degraded for a long time. The micro-defect distribution also showed appreciable variability. These observations indicate that there was a considerable degree of inhomogeneity in the degradation process.

6.2.2 One-part adhesive system (AA1100-O - Hysol EA9346)

Figure 6.11 shows the peel force data for the Hysol EA 9346 one-part adhesive for wet and dry cases as a function of exposure time. Each data point represents the mean of the average peel forces of specimens from at least three batches. Figure 6.12 gives the tensile test results for a freshly-cured cast adhesive specimen, and 100-day old wet and dry cast specimens.

The wet and dry tests show similar behavior because this adhesive undergoes very little plasticization. This can be seen from Fig. 6.12, where the Young's modulus of a fresh sample is about 2.3 GPa, and for degraded samples, both wet and dry, is about 2 GPa. The crack paths for both wet and dry specimens were essentially interfacial, again showing the absence of significant adhesive plasticization for the wet samples. Therefore, for this one-part adhesive, both wet and dry results were affected primarily by interfacial weakening. It is noteworthy that some of the interfacial strength was regained upon drying, indicating that for this system there was some reversible degradation superimposed on a larger permanent degradation.

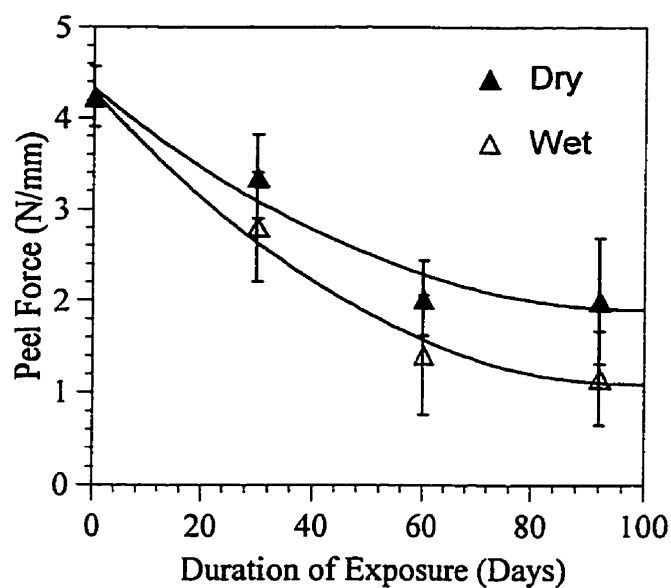


Figure 6.11: Peel force vs. exposure time for the one-part (Hysol EA9346) adhesive, both in wet and dry conditions. The error bars represent one standard deviation each on both sides of the mean value. The curves are quadratic fits ($r^2 \approx 0.95$ for dry and $r^2 = 0.99$ for wet).

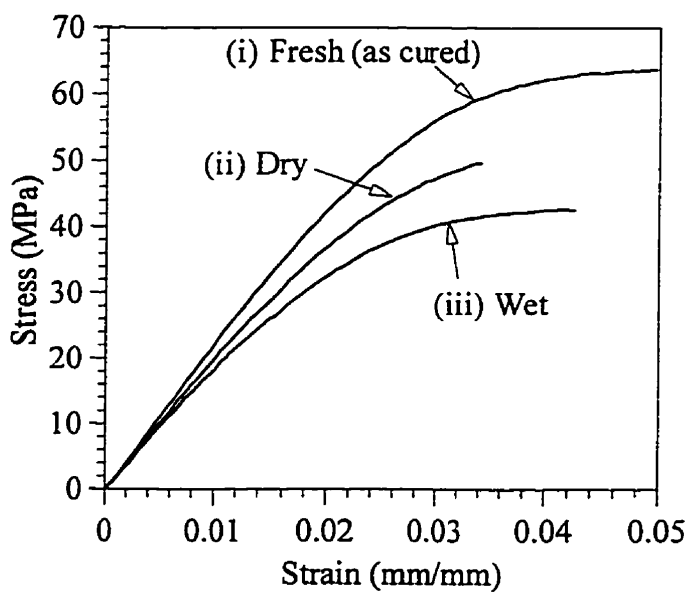


Figure 6.12: Tensile test results for cast one-part adhesive (Hysol EA9346) tested in three conditions: i) freshly cured, ii) immersed for 100 days and then tested wet, iii) immersed for 100 days and then tested dry.

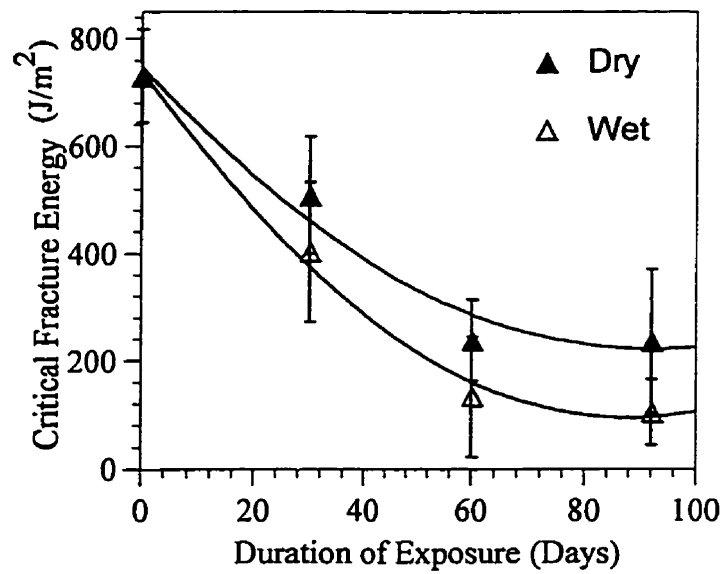


Figure 6.13: Fracture energy vs. exposure time for one-part wet and dry cases (peel data of Fig. 6.11). The error bars represent one standard deviation each on both sides of the mean value. The curves are quadratic fit ($r^2 = 0.97$ for dry and $r^2 = 0.99$ for wet).

Figure 6.13 shows the fracture energy corresponding to the peel force data in Fig. 6.11. In this case, since the cohesive properties do not vary greatly with degradation (Fig. 6.12), the change in the adherend plastic dissipation due to change in adhesive modulus was negligible. The failure loci for fresh, degraded-wet and degraded-dry specimens were very close to the interfacial region with no residual adhesive visible on the flexible aluminum strip. However, the aluminum surfaces of the degraded samples appeared shiny compared to that of fresh samples, suggesting cohesive failure for the fresh samples and interfacial failure for the degraded samples. There were no significant differences visible between the surfaces of fresh and degraded (wet or dry) specimens in SEM micrographs (Fig. 6.14). The X-ray analysis of the aluminum surface also did not show any appreciable differences between fresh and degraded fracture surfaces. The adhesive side of the failure surface was also examined using the SEM, and again no differences were found between fresh and degraded samples on a microscopic level. However, the X-ray analysis of the adhesive side of the failed specimen did show some traces of aluminum, although this was inconclusive due to a lack of consistency. More surface-sensitive analytical techniques, such as X-ray Photoelectron Spectroscopy (XPS), may be required to reveal appreciable differences between fresh and degraded

surfaces.

As with the two-part system, there was considerable scatter in the peel force data, with the degraded samples (wet and dry) showing more scatter as the exposure time increased.

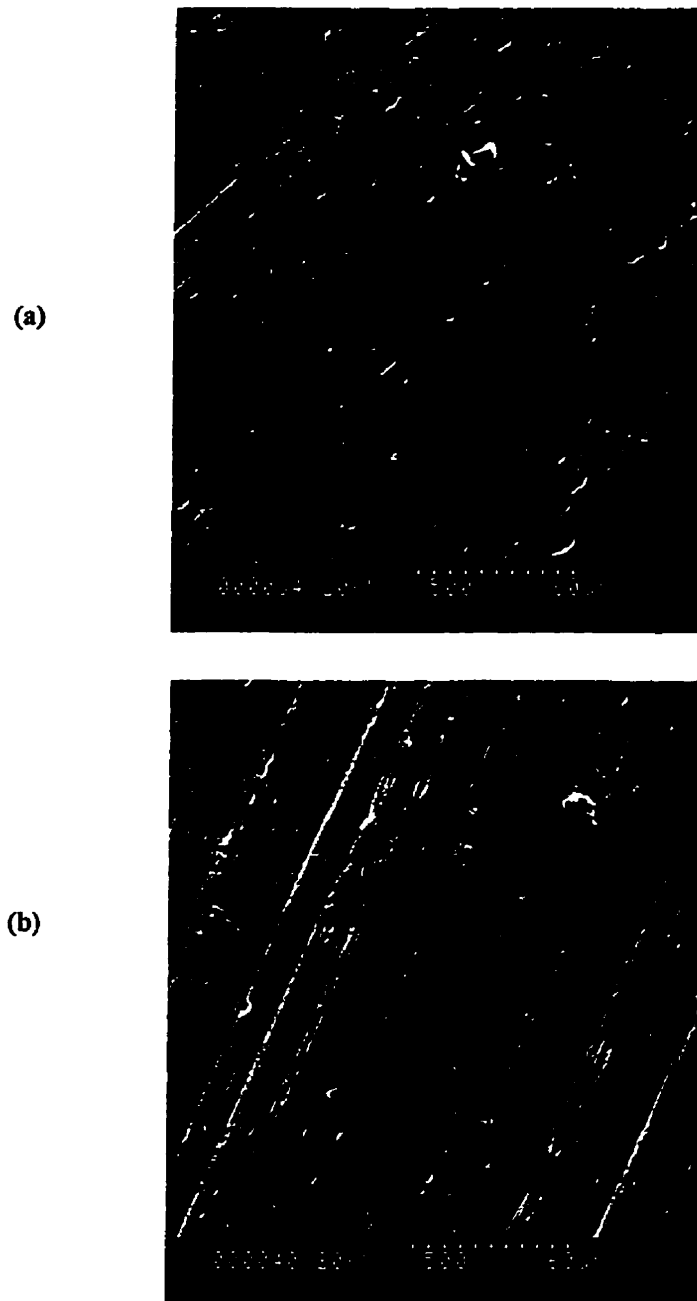


Figure 6.14: SEM micrographs of (a) a fresh specimen, and (b) a degraded (60 days) specimen of the one-part adhesive system (Hysol EA9346).

6.3 Ultrasonic Test Results

6.3.1 Two-part system (AA1100-O alloy - Permabond E04 adhesive)

6.3.1.1 Normal-incidence measurements

This section deals with the results of the plane wave reflection measurements of shear and compression waves incident normally at the interfacial region of the two-part (AA1100 - Permabond E04) system. The major objective of these measurements was to determine the interfacial spring constants as a function of degradation. It should be noted that all the ultrasonic experiments were conducted in a *dry* state, i.e., only permanent degradation of the joint was assessed ultrasonically.

Figure 6.15 gives the experimental reflection coefficient spectra of normally incident shear waves for different exposure levels ranging from the fresh condition to 15.5 months of exposure. Each curve represents the average of at least eight measurements. Figure 6.16 gives the shear reflection coefficient at 15 MHz as a function of duration of exposure. Figures 6.17 and 6.18 gives the results of similar measurements for normally incident compression (longitudinal) waves. In the longitudinal case, the reflection spectra (Fig. 6.17) represent the average of at least twenty four measurements.

Before comparing the experimental results with theory in detail, some general observations may be made. First, for all cases, the reflection coefficient increases with frequency, consistent with the spring model of the interfacial region (Chapter 4, Fig. 4.2). It may be observed that initially (until 8 months of exposure) the reflection coefficient shows a slight drop in the amplitude with exposure, although this is more clearly evident for shear waves (Fig. 6.16) compared to longitudinal waves (Fig. 6.18). The decrease in the reflection coefficient is due primarily to the increase in the wave velocities of the adhesive in a dried, degraded state as given in Table 6.2; shear waves showing a relatively large increase in velocity compared to longitudinal waves. This increase in the wave velocities is consistent with the increase in Young's modulus (Fig. 6.6) for the two-part system in a dried state after degradation. After the 8-month exposure level, the reflection coefficient is observed to increase (Fig. 6.16 and 6.18) with exposure, indicating interfacial degradation.

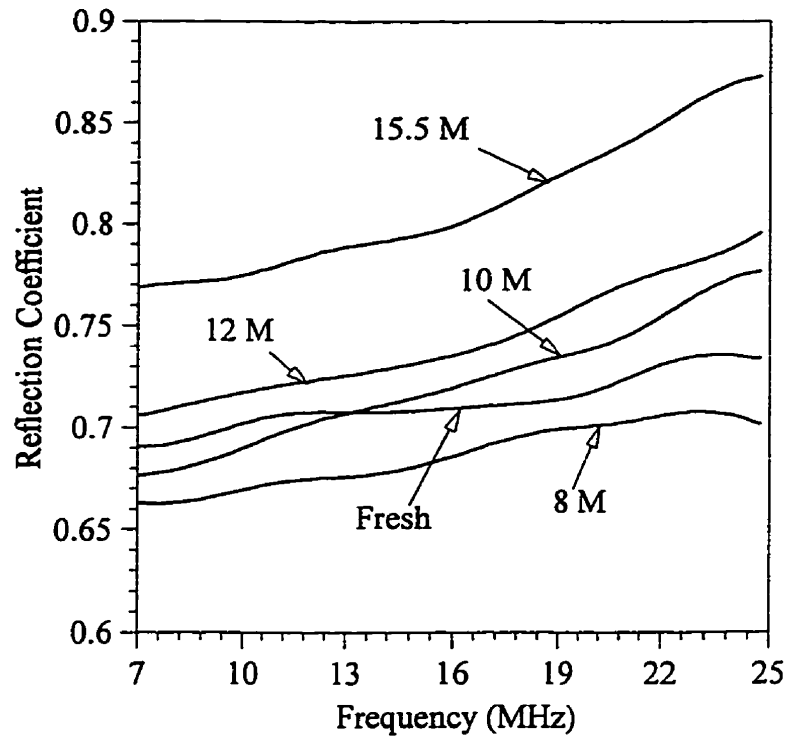


Figure 6.15: Measured normal shear-wave reflection coefficient spectra of the interfacial region, corresponding to various levels of degradation of the two-part (Permabond E04) system; 'M' indicates months of degradation.

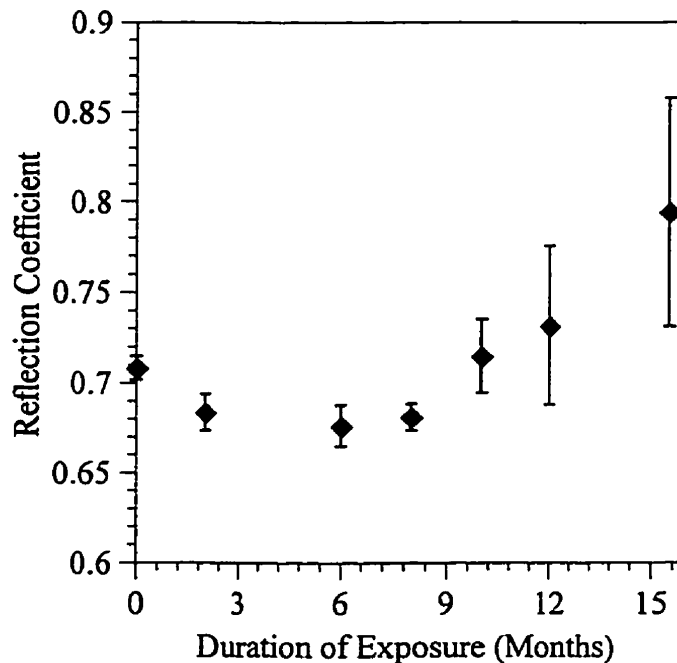


Figure 6.16: Measured reflection coefficients at 15 MHz of normal-incidence shear waves, as a function of duration of exposure for the two-part (Permabond E04) system. The error bars correspond to one standard deviation each on both sides of the mean value.

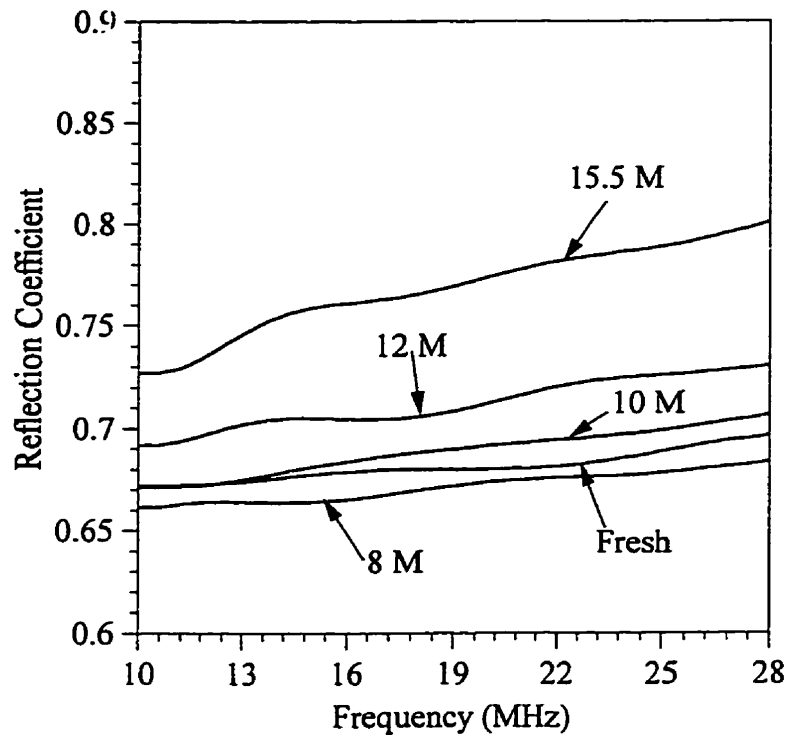


Figure 6.17: Measured normal longitudinal-wave reflection coefficient spectra of the interfacial region, corresponding to various levels of degradation of the two-part (Permabond E04) system; 'M' indicates months of degradation.

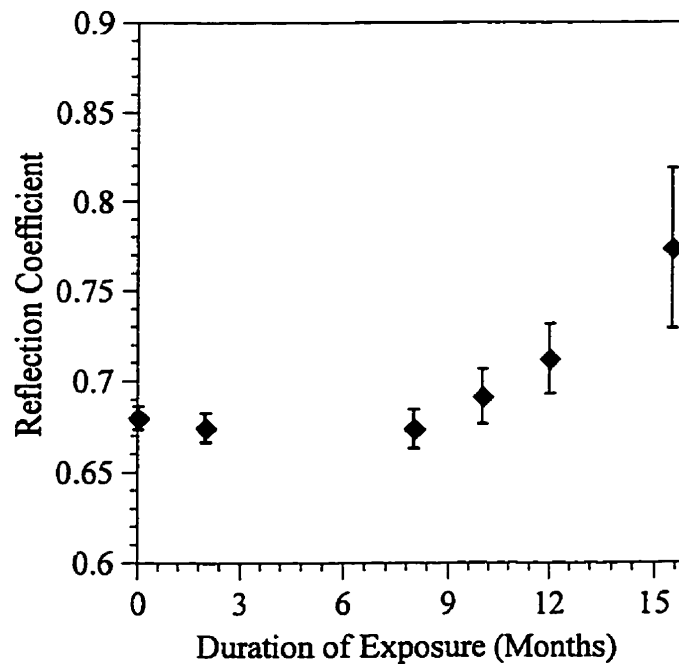


Figure 6.18: Measured reflection coefficients at 20 MHz of normal-incidence longitudinal waves, as a function of duration of exposure for the two-part (Permabond E04) system. The error bars correspond to one standard deviation each on both sides of the mean value.

Table 6.2 Material properties used in the calculations

	$c_t(\text{m/s})$	$c_l(\text{m/s})$	$\rho \text{ (kg/m}^3\text{)}$
Aluminum	3160	6435	2690
E04 adhesive	1175 (fresh)	2530 (fresh)	1360
	1296 (degraded)	2600 (degraded)	

The tangential and normal spring constants, K_t and K_n , were determined from the shear and longitudinal measurements respectively, by a least-square optimization procedure which minimizes the objective function G , given by:

$$O = \int (R_{th}(\omega) - R_{ex}(\omega))^2 d\omega \quad (6.1)$$

where R_{th} is the theoretical spectrum (Eq. 4.1) and R_{ex} is the experimental spectrum. It should be noted that the integrand in Eq. 6.1 is discrete. Table 6.2 gives the material properties used in the calculations. Figure 6.19 compares the experimental reflection coefficient spectra with the theoretical spectra for normally incident shear waves. Figure 6.20 gives a similar comparison for normally incident longitudinal waves. It may be observed from Figs. 6.19 and 6.20 that there is very good agreement between theory and experiments except for relatively large degradation.

Table 6.3 gives the values of the spring constants determined by minimizing the parameter G in Eq. 6.1. An error analysis of the spring constants was carried out based on the reflection coefficient data at the central frequency (15 MHz for shear and 20 MHz for longitudinal wave respectively). The results are given in Table 6.4, showing the 95% confidence intervals of the reflection coefficients at the central frequencies, and the spring constants.

Table 6.3 Spring constants for various levels of degradation for the two-part (Permabond E04) adhesive system

Exposure Level (Months)	0	2	8	10	12	15.5
$K_t \text{ (GPa/}\mu\text{m)}$	0.50	0.53	0.54	0.34	0.29	0.18
$K_n \text{ (GPa/}\mu\text{m)}$	1.98	2.09	2.21	1.38	0.99	0.58

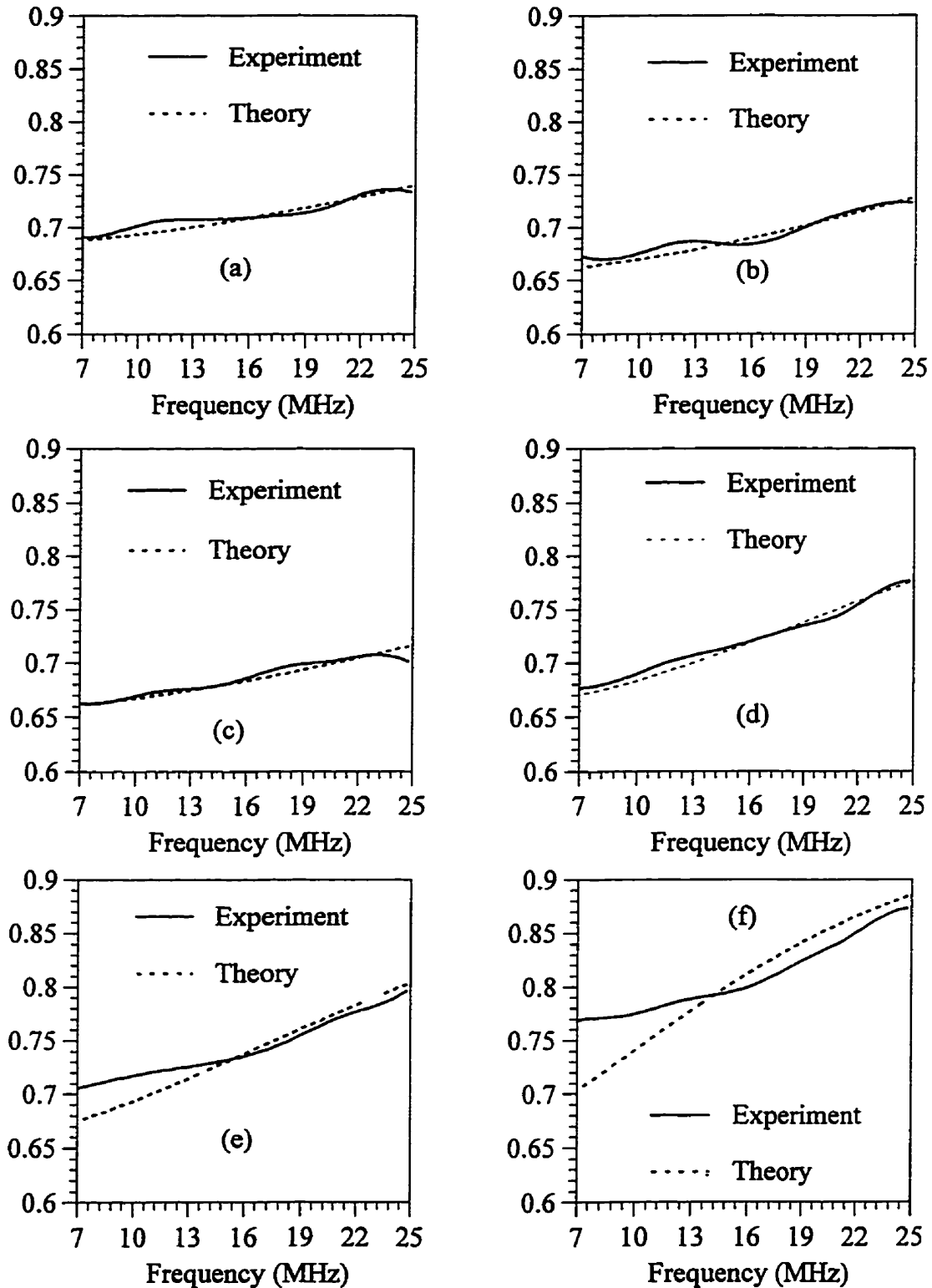


Figure 6.19: Comparison of theoretical and experimental reflection coefficient spectra of normal-incidence shear waves for the two-part (Permabond E04) system; (a) fresh, (b) 2-month, (c) 8-month, (d) 10-month, (e) 12-month and (f) 15.5-month exposure levels.

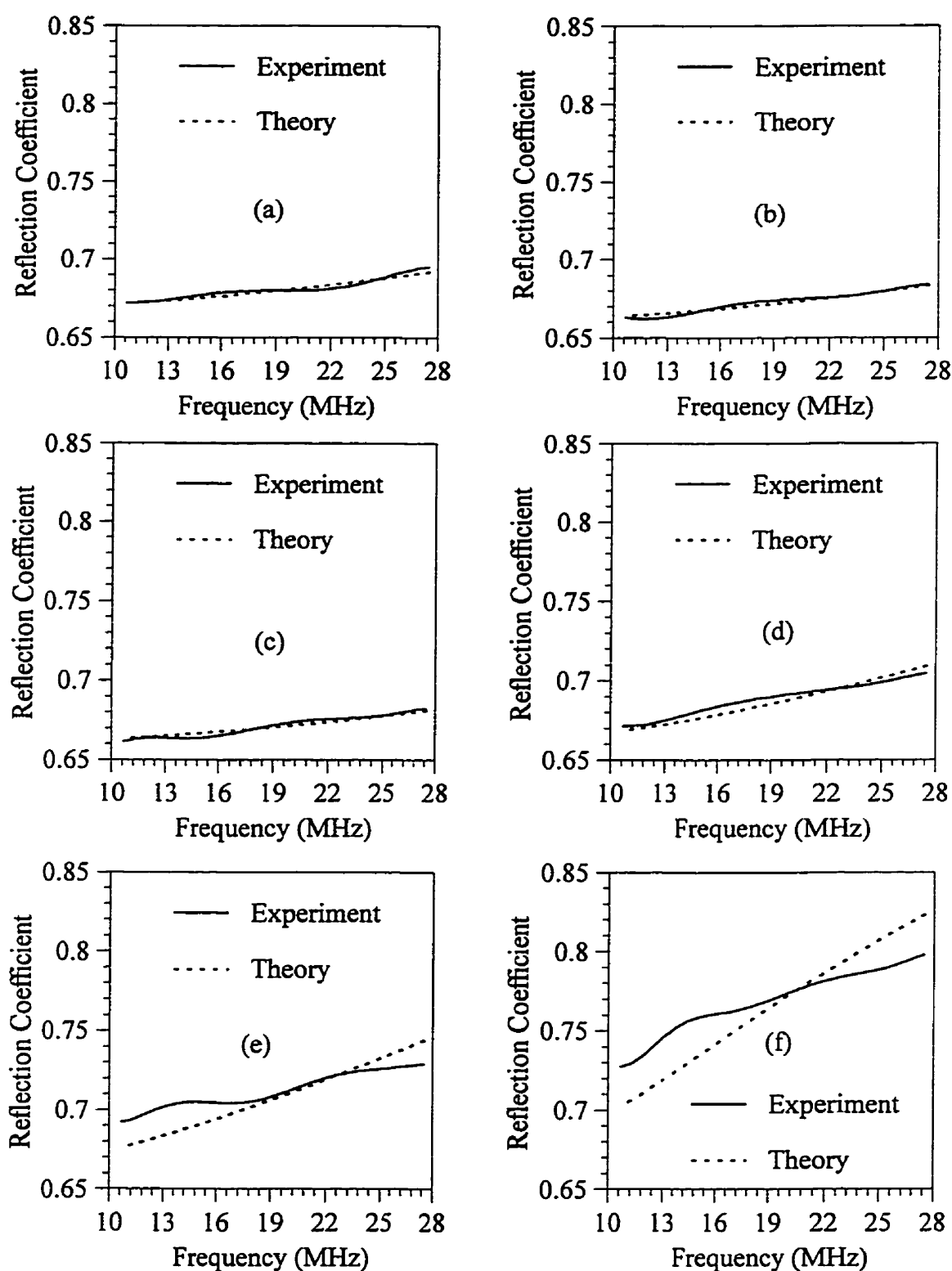


Figure 6.20: Comparison of theoretical and experimental reflection coefficient spectra of normal-incidence longitudinal waves for the two-part (Permabond E04) system; (a) fresh, (b) 2-month, (c) 8-month, (d) 10-month, (e) 12-month and (f) 15.5-month exposure levels.

Table 6.4 95% confidence intervals for the spring constants for the two-part (Permabond E04) adhesive system

Exposure Level (Months)	Shear wave incidence		Longitudinal wave incidence	
	R_{SS} (15 MHz)	K_t (GPa/ μm)	R_{LL} (20 MHz)	K_n (GPa/ μm)
0	0.709 ± 0.0072	$0.42 < K_t < 0.58$	0.682 ± 0.0032	$1.76 < K_n < 2.28$
2	0.684 ± 0.0057	$0.48 < K_t < 0.60$	0.674 ± 0.0038	$1.79 < K_n < 2.41$
8	0.682 ± 0.008	$0.47 < K_t < 0.66$	0.672 ± 0.0045	$1.77 < K_n < 2.57$
10	0.716 ± 0.0175	$0.29 < K_t < 0.41$	0.689 ± 0.0052	$1.25 < K_n < 1.54$
12	0.733 ± 0.0275	$0.23 < K_t < 0.38$	0.711 ± 0.0067	$0.92 < K_n < 1.07$
15.5	0.955 ± 0.0483	$0.14 < K_t < 0.26$	0.774 ± 0.0078	$0.55 < K_n < 0.62$

It may be observed that the spring constants remain approximately the same ($K_n \approx 2.0$ GPa/ μm and $K_t \approx 0.5$ GPa/ μm) until the 8-month exposure level, although the critical fracture energy shows a considerable drop during the same period (Fig. 6.7). The small variabilities in the spring constants during this period (i.e., 0-8 months exposure) are within the experimental uncertainties (Table 6.4).

It should be noted that the reflection coefficient spectra from a perfect interface between two solids is independent of frequency. The sloping reflection coefficient spectra for the fresh joint (Fig. 6.19 and 6.20) is evidence of the presence of a very thin interfacial region with lower mechanical properties compared to the bulk adhesive (Section 2.1.3); this layer is represented by the normal and tangential springs.

After 10 months of exposure, the spring constants are observed to reduce substantially (Table 6.3), and there is excellent agreement between theory and experiment in the reflection spectrum (Fig. 6.19d and 6.20d). From Fig. 6.7, it may be seen that the critical fracture energy

drops by about 30% after ten months of exposure. It should be noted that the formation of micro-defects (Fig. 6.8) was observed consistently at the interface after about 10 months. Since most of these defects were sub-wavelength, they would in effect decrease the local stiffness, resulting in reduced spring constants.

At the 12-month exposure level, the spring model is observed to be approximately valid (Fig. 6.19e and 6.20e), while the 15.5-month data (Fig. 6.19f and 6.20f) shows relatively more discrepancy between theory and experiments. One possible reason for the discrepancy between the theoretical and experimental spectra may be the reduction in the density of the bulk adhesive as a result of significant adhesive leaching at large exposure levels (Fig. 6.1). The theoretical curves in Figs. 6.19 and 6.20 were all calculated assuming the density to be unchanged. Figure 6.21 shows a revised calculation for the 15.5-month, shear-wave data with a reduced density value of 1100 kg/m^3 . It is seen that the theory becomes closer to experiments when the density is reduced. It was not possible to determine the density of the degraded adhesive layer on an aluminum substrate experimentally.

It is also possible that for relatively large degradation levels, the micro-defects grow to become comparable in size to the ultrasonic wavelength. This would cause the defects to act as scatterers of ultrasound. This may contribute to the large spread in the data observed for relatively severe degradation (Fig. 6.16 and Fig. 6.18).

The normal incidence measurements generally showed increased sensitivity of shear waves to degradation compared to longitudinal waves at a given frequency (see Fig. 6.15 and 6.17). For example, the longitudinal-wave reflection coefficient (R_{ll}) at 25 MHz for the 10-month exposure level (Fig. 6.20d) showed an increase of 3% compared to the 2-month exposure level (Fig. 6.20b). The corresponding increase in shear-wave reflection coefficient (R_{ss}) at 25 MHz for the 10-month case was 7% (Fig. 6.19). At 15.5 months of exposure, the increase in R_{ss} was 21% compared to 15% for R_{ll} (Fig. 6.19 and 6.20). This higher sensitivity is due to the shorter wavelength of shear waves compared to longitudinal waves, as explained in Section 4.1.1.

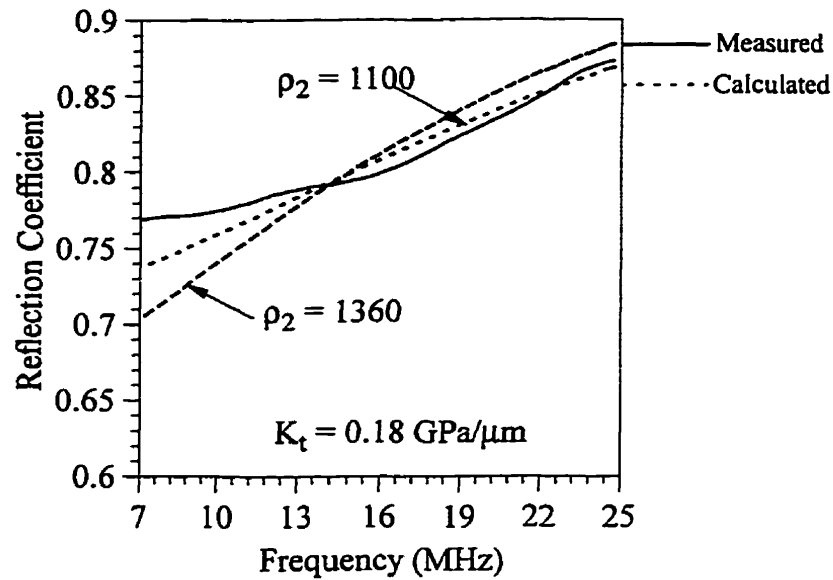


Figure 6.21: Comparison of theory and experiments for the 15.5-month data of the two-part system (Permabond E04). The dashed lines are calculated spectra corresponding to two different values of adhesive density (1360 and 1100 kg/m³), and the solid line is the experimental spectrum.

Although normal-incidence shear wave measurements may be performed under ideal laboratory conditions, they are very difficult to perform in a field environment. This is because normal-incidence shear waves can not be generated via mode conversion at a water/sample interface. However, oblique shear waves may be readily generated in the adherend by this method.

6.3.1.2 Oblique-incidence shear wave measurements

This section deals with the oblique-incidence shear wave reflection measurements from the interfacial region of the two-part adhesive. The measurement system described in Chapter 5 (Section 5.3.3) was used for the experiments. In the case of oblique incidence, both the normal and tangential spring constants (K_n and K_t , respectively) are relevant, and were available from the normal-incidence experiments (Table 6.3). The experimental reflection spectra of obliquely incident shear waves will be compared with those obtained from the angular spectrum model developed for the measurement system (Section 4.2.2).

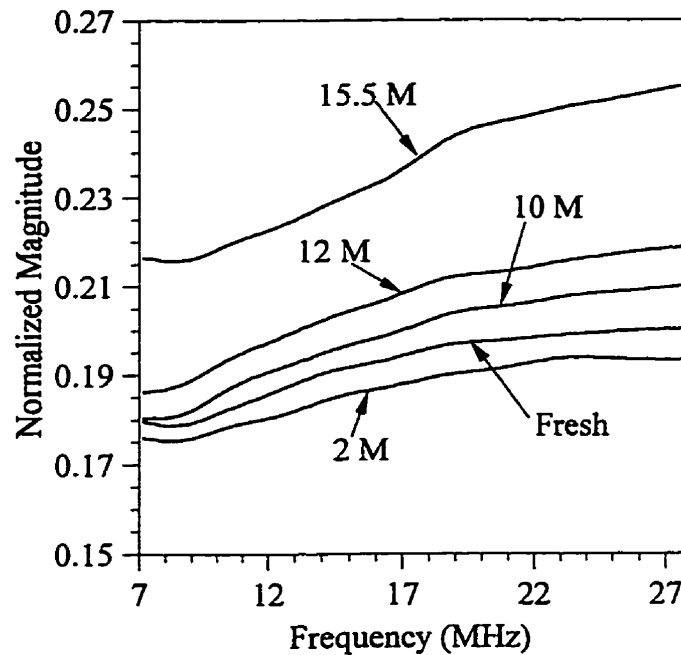


Figure 6.22: Measured oblique-incidence shear-shear (SS) reflection spectra for the two-part (Permabond E04) system at various levels of degradation. The shear wave was focused ($d = 4.5$ mm) at the interfacial region, and normalized with respect to the front-wall signal; 'M' indicates months of exposure.

Focused position: It may be re-called (Section 4.2.4) that the configuration best suited for examining the interfacial region is where the shear wave is focused at the interfacial region. Figure 6.22 shows the measured reflection spectra corresponding to the focused position, for fresh and 2, 10, 12 and 15.5 months exposure levels. The obliquely incident shear waves showed a higher sensitivity to degradation compared to normally incident shear waves, particularly for relatively large exposure levels. For example, the normalized amplitude at 25 MHz for the 12-month exposure level is 12% greater than that for the 2-month exposure level (Fig. 6.22); this compares to a 10% increase in the reflection coefficient at 25 MHz (Fig. 6.19) for normally incident shear waves. For the 15.5-month case the corresponding increase in normalized amplitude was 30%, compared to a 21% increase for normally incident shear waves. This increased sensitivity of obliquely incident shear waves may be attributed to the angular dependency of the plane wave reflection coefficients (Section 4.1.2).

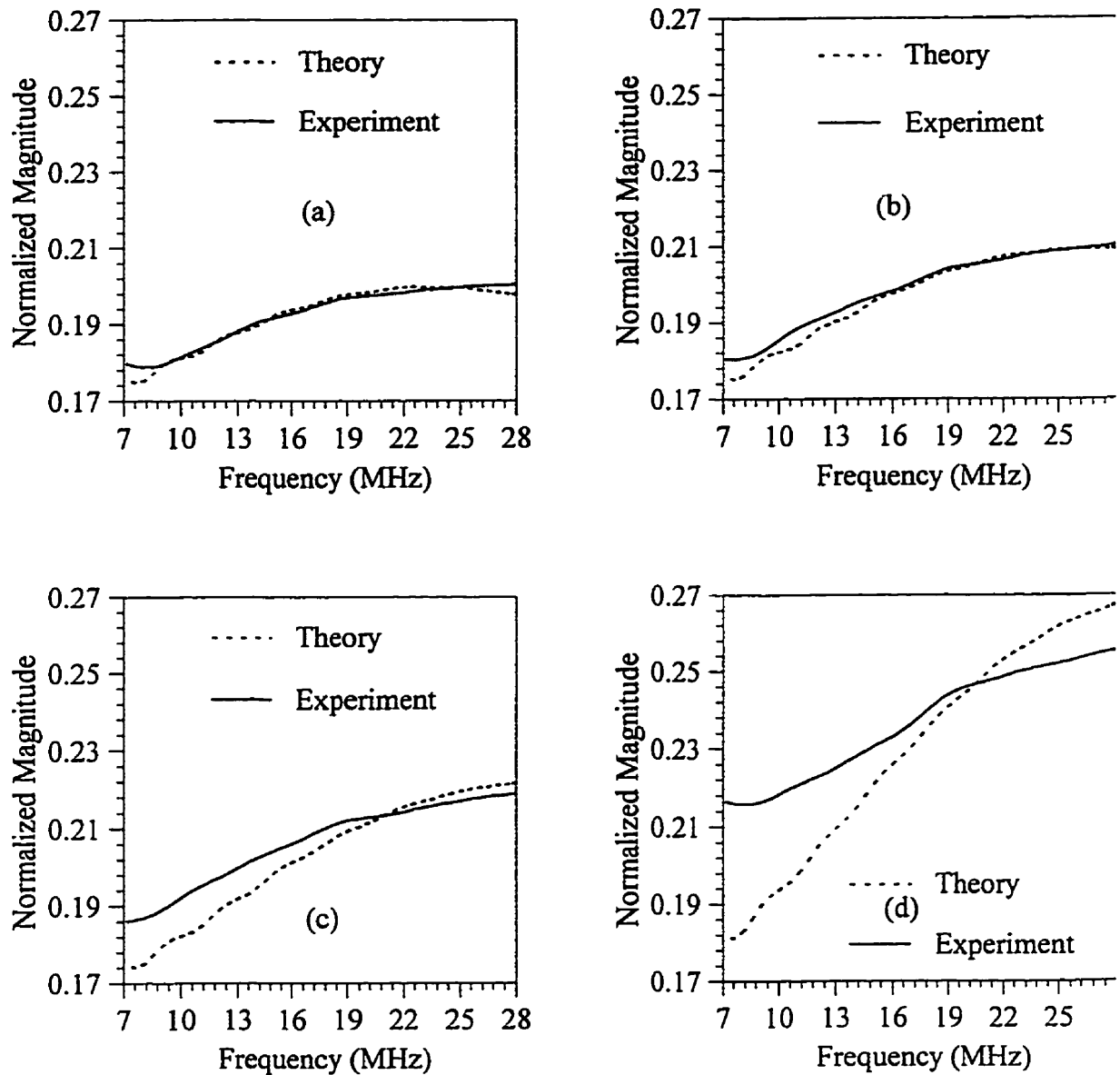


Figure 6.23: Comparison of theory and experiments for obliquely incident shear waves (SS) under focused condition, for different levels of degradation of the two-part (Permabond E04) system; (a) Fresh, (b) 10 months, (c) 12 months, (d) 15.5 months. The solid line is experimental and the dashed line is theoretical.

The geometrical tolerances in the manufacturing of the focused, oblique-incidence transducer (Section 5.3.3) were relatively large; approximately 5-10% of the nominal dimensions. Therefore, in order to compare the theory and experiments, the actual values of the transducer parameters (namely, the nominal incident angle, θ_i , and the aperture angle θ_0) must be determined. This was achieved by matching the experimental shear-shear reflection spectrum of a fresh specimen to that predicted by the angular spectrum theory, using the spring constant values given in Table 6.3 and the material properties given in Table 6.2. The longitudinal wave velocity and attenuation factor of water, required for the predictions, were calculated from the measured temperature [89]. The actual probe parameters were determined to be: $\theta_i = 17.1^\circ$ and $\theta_0 = 15.3^\circ$, compared to the nominal values of $\theta_i = 17.9^\circ$ and $\theta_0 = 14.3^\circ$.

The measured reflection spectra were compared with the predictions of the angular spectrum theory as shown in Fig. 23, from the known values of the spring constants (Table 6.3) and probe parameters. As in the case of normal-incidence measurements, there is good agreement between the theoretical and experimental spectra for the fresh and 10-month cases. For the 12-month case, the agreement is somewhat inferior, while for the 15.5-month case, the agreement between theory and experiment is relatively poor. The significant reduction in the adhesive density at large degradation and the possible scattering of the waves by relatively large micro-defects may account for some of the discrepancy.

De-focused position: As was described in Chapter 4 (Section 4.2.4), by de-focussing the probe towards the specimen, interference effects are produced that can be displayed in the frequency domain. These interference effects for shear waves were shown to be highly sensitive to the spring constants, although it was also found that slight changes in the adherend properties and transducer alignment affect the interference pattern substantially.

Figure 6.24 shows the measured spectra for different levels of degradation when the probe was de-focused to $d = 6.0$ mm (as opposed to $d = 4.5$ mm for focused configuration, Section 4.2.4). For relatively large exposure levels, such as the 15.5-month data, the increase

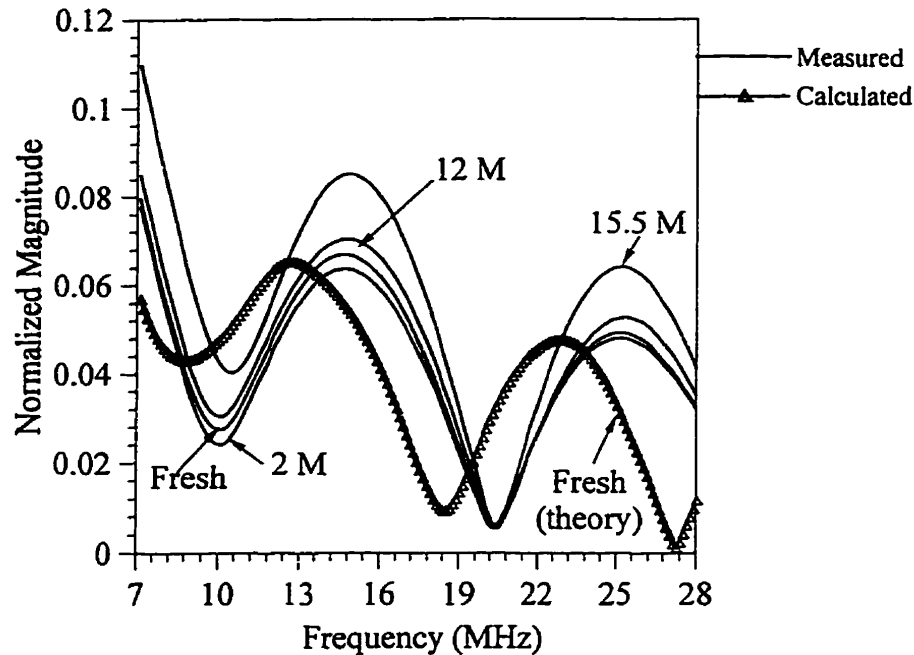


Figure 6.24: Oblique-incidence SS reflection spectra for various levels of degradation under the de-focused ($d = 6.0$ mm) condition; the solid lines are measured spectra and the line with symbol is the predicted spectrum for the fresh case.

in sensitivity of the amplitude spectrum to degradation under the de-focused condition was confirmed experimentally. For example, it may be seen from Fig. 6.24 that the peak amplitude at 15 MHz of the 15.5-month data increases by about 34% relative to the 2-month exposure level, while at the focused position (Fig. 6.19), the increase in amplitude is about 24%. For exposure levels lower than 15.5 months, the increase in sensitivity was ambiguous, possibly due to the generally higher scatter under the de-focused condition.

Figure 6.24 includes the theoretical spectrum for freshly bonded specimens using the material properties in Tables 6.2 and 6.3. It is noted that the positions of the dips and peaks in the theoretical and experimental amplitude spectra do not match. The peak heights of the fresh specimen match well between theory and experiments. It may be re-called (Fig. 4.10) that the peaks and dips are quite sensitive to adherend properties. Therefore, slight errors in the adherend properties or small misalignments during the experiments might be responsible for

the discrepancy between the theoretical and experimental spectra.

6.3.2 One-part system

6.3.2.1 Normal-incidence shear wave measurements

In this section, the results of normal-incidence shear wave reflection coefficient measurements for the one-part adhesive system (Hysol, EA9346) are presented. Figure 6.26 shows the reflection coefficient at 15 MHz as a function of degradation. There is no significant change in the amplitude of the reflection coefficient, although the scatter in the data increases with the duration of exposure. It may be noted that the critical fracture energy decreased by about 70% after 3 months of exposure (Fig. 6.13).

It should be noted that the failure surface analysis of the one-part system did not reveal any significant physical changes in the vicinity of the interfacial region as a result of degradation (Fig. 6.14), unlike the two-part system which showed the formation of micro-defects. The fact that the reflection coefficient remained constant with degradation indicates that the adhesive interphase did not change its properties significantly.

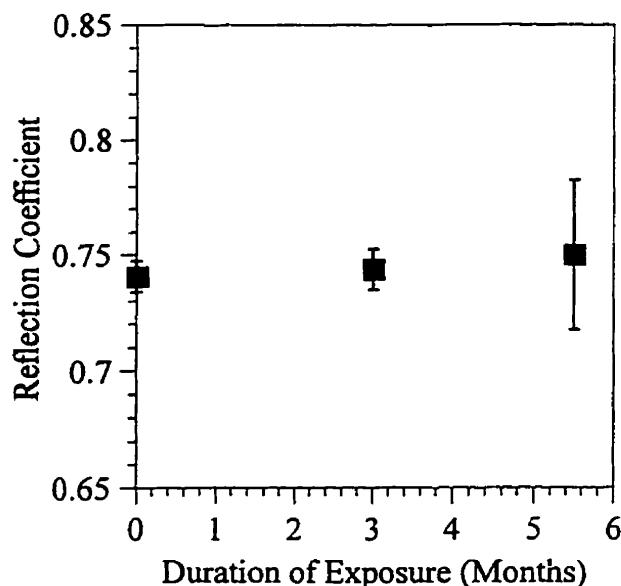


Figure 6.25: Normal-incidence shear wave reflection coefficients at 15 MHz for the one-part (Hysol EA9346) adhesive system as a function of duration of exposure. The error bars correspond to one standard deviation on each side of the mean value.

It is likely that most of the decrease in the critical fracture energy with exposure was due to the rupture inter molecular forces operating across the interface (Section 2.1.2). The potential of using ultrasound in the 5-25 MHz range to monitor environmental degradation of this one-part adhesive system appears to be very low.

Conclusions and Recommendations

7.1 Conclusions

7.1.1 Peel analysis

The present work developed an analytical approach to predict the adherend plastic dissipation in the peel test, allowing the determination of the critical fracture energy, G_c , and the mode ratio from experimental peel data.

It was shown, both theoretically and experimentally, that plastic dissipation can be very sensitive to the adherend yield stress, thickness and peel angle. This has important implications in the design of a peel test in order to minimize the effects of adherend plastic dissipation, thereby maximizing the accuracy in the calculation of G_c . It was demonstrated that for medium to high strength adhesives, the effects of plastic dissipation may be kept relatively small by the use of a low peel angle, and a low yield strength alloy with a thickness much less than a critical thickness at which the plastic dissipation is a maximum. At the other extreme, for relatively low fracture energy systems, the plastic dissipation may be reduced by the use of a relatively low peel angle and a high yield-strength alloy with a thickness much larger than the critical thickness.

The model was employed to determine the critical fracture energy, G_c , and the mode ratio from experimental peel data for several combinations of peel angle and adherend properties, but with the same adhesive and adherend-pretreatment. It was shown that the extracted G_c reduced to about the same value regardless of the peel angle and adherend properties. The relatively small differences in the estimates of G_c were explained by the mode of loading, and possible crack-tip adhesive dissipation effects.

7.1.2 Open-faced specimen for the assessment of durability

A novel, open-faced peel specimen was developed to investigate adhesive joint durability. It was shown that for adhesives which plasticize to a great extent, such as the two-part system Permabond E04, peel testing should be carried out in the dry state to assess interfacial weakening, since the failure was mostly cohesive in the wet condition. For moisture-resistant adhesives, such as the one-part Hysol EA 9346 adhesive, both wet and dry tests revealed interfacial weakening.

The two-part adhesive in the dry state after degradation was found to become relatively stiff and brittle compared to the fresh state. Since the plastic dissipation in the flexible adherend is dependant on the adhesive stiffness, it is necessary to account for this change in the adhesive stiffness when calculating the critical fracture energy.

The peel failure surfaces were analyzed using Scanning Electron Microscopy (SEM) and Energy Dispersive Spectroscopy (EDS). For the two-part system, the fresh specimens failed cohesively, while degraded (dry) specimens revealed micro-defect formation at the interface. For the one-part system, the above analyses did not show any significant difference between fresh and degraded surfaces, although visual evidence suggested cohesive failure for fresh specimens and interfacial failure for degraded specimens.

7.1.3 Ultrasonic NDE of interfacial degradation

Durability of the two adhesive systems was characterized ultrasonically using open-faced specimens. It was found that ultrasound can detect the interfacial degradation of the two-part epoxy system, but did not show any significant change in response with degradation of the one-part system. It should be emphasized that the ultrasonic NDE of interfacial strength degradation is based on the hypothesis that degradation is accompanied by physical changes in the interfacial region, which result in changes in the interfacial spring constants. Destructive studies showed physical changes in the form of micro-defects in the case of the two-part system, but it did not reveal any such physical changes at the interface for the one-part system.

Measured values of normal-incidence longitudinal and shear wave reflection coefficients were in good agreement with the interfacial spring model for the two-part system, except for

relatively large degradation. It was found that both tangential and normal spring constants decrease with degradation for the present two-part system. The normal-incidence measurements showed that shear waves were more sensitive to interfacial properties than were longitudinal waves.

Oblique shear-wave reflection measurements were performed on the two-part adhesive system using a novel transducer. An angular spectrum approach was developed to model the measurement system. It was found that the best practical configuration for the inspection of the interfacial region features a shear wave focused at the interfacial region. The oblique-incidence measurements were in good agreement with the angular spectrum theory except for relatively large degradation values. Oblique shear waves generally showed higher sensitivity to degradation, compared to normal shear waves.

It should be emphasized that the present work confirmed earlier reports of the inherent difficulties in the NDE of the interfacial region [47]. The use of open-faced specimens enabled the nondestructive evaluation of degradation for the two-part system. In the ideal laboratory setting, it was possible to detect the interfacial degradation after 10 months of exposure to water at 67°C , corresponding to a decrease in G_c of about 30%. The corresponding increase in the normalized amplitude of reflected oblique shear waves was about 6% at 15 MHz. It is unlikely that in a rugged industrial environment, such a small change in amplitude could be measured reliably. After 15.5 months of exposure, the increase in amplitude was about 24%, corresponding to a decrease in G_c of about 45%. Therefore, it is reasonable to conclude that, in practice, a drop in G_c of approximately half the initial value may be detected nondestructively for the two-part system by an oblique shear wave reflection technique.

7.2 Contributions

The major contributions of the present work may be summarized as follows:

- An analytical model was developed and experimentally verified [79, 80], to predict the adherend plastic dissipation in the peel test, enabling the determination of the critical fracture energy and mode ratio.

- A novel open-faced peel specimen was developed for the study of the durability of adhesive joints [93]. The use of such a specimen was demonstrated for two typical commercial adhesives, with emphasis on the wet and dry behavior.
- The formation of micro-defects at the interface, as a result of degradation, was discovered for the two-part system [93].
- It was shown that ultrasonic reflection measurements may be used to detect interfacial degradation for the two-part adhesive system. The interfacial spring model was shown to be a good description of the interfacial region for the two-part system. This is the first work which has shown the validity of the spring model for the interfacial region of an adhesive joint.
- An efficient angular spectrum model was developed for an oblique-incidence, focused wave measurement system [86].
- A novel PVDF transducer was developed for oblique-incidence measurements [87]. A reliable method was developed for the measurement of the normal shear-wave reflection coefficient from the adhesive/adherend interfacial region.

7.3 Recommendations for future work

It is recommended that the peel model be generalized to include the effects of plasticity in a general adhesive sandwich. This will be useful in modelling plastic deformation in situations such as the lap shear test with a relatively thin adherend. It is also suggested that the accuracy of the assumptions made in the present analysis be determined by using a finite-element model.

It is recommended that highly sensitive surface analysis methods such as X-ray Photoelectron Spectroscopy (XPS) or high resolution SEM be used to determine the actual mechanism of micro-debonding for the two-part adhesive system. It would be useful to know whether any hydration of the aluminum oxide occurs at the micro-defect sites observed with the two-part system. It is suggested to investigate whether micro-debonding occurs for other high-strength two-part systems. It is also recommended that the actual failure mechanism of

the one-part system be determined using XPS.

It is recommended to investigate the perturbations in the ultrasonic guided modes of the adhesive layer as a result of the observed interfacial changes for the two-part system. The guided-mode technique involves frequency measurements; which tend to be more repeatable than amplitude measurements. It is advised to investigate the use of high frequency ultrasound to detect interfacial degradation for the one-part system.

References

1. Kinloch, A. J., *Adhesion and Adhesives: Science and Technology*, Chapman and Hall Ltd., New York, 1987.
2. Packam, D. E., (Editor), *Handbook of Adhesion*, Longman Scientific & Technical, Harlow, England, 1992.
3. Kinloch, A. J., Chapter 1, in *Durability of Structural Adhesives*, edited by Kinloch, A. J., Applied Science Publishers, 1983.
4. Davis, G. D., and Venables, J. D., Chapter 2, in *Durability of Structural Adhesives*, edited by Kinloch, A. J., Applied Science Publishers, 1983.
5. Crompton, J. S., "Interfacial properties and stability in bonded aluminum", *Journal of Material Science*, Vol. 24, 1989, pp. 1575-1581.
6. Cognard, J., "The metal/polymer interphase in adhesive joints", *International Journal of Adhesion and Adhesives*, Vol. 11, No. 2, April 1991, pp. 114-116.
7. Knollman, G. C., "Variation of shear modulus through an interfacial bond zone of an adhesive", *International Journal of Adhesion and Adhesives*, Vol. 5, No. 3, July 1985, pp. 137-141.
8. Safavi-Ardebili, V., *Micromechanical characterization of the interphase zone in adhesive joints*, Ph.D. thesis, Department of Mechanical and Industrial Engineering, University of Toronto, 1997.
9. Comyn, J., Chapter 3, in *Durability of Structural Adhesives*, edited by Kinloch, A. J., Applied Science Publishers, 1983.
10. Comyn, J., Brewis, D. M., Shalash, R. J. A., and Tegg, J. L., Chapter 2, in *Adhesion 3*, edited by Allen, K. W., Applied Science Publishers, London, 1978.
11. Althof, W., Chapter 2, in *Adhesion 5*, edited by Allen, K. W., Applied Science Publishers, London, 1980.

12. Zanni-Deffarges, M. P., and Shanahan, M. E. R., "Diffusion of water into an epoxy adhesive: Comparison between bulk behavior and adhesive joints", *International Journal of Adhesion and Adhesives*, Vol. 15, No. 3, 1995, pp. 137-142.
13. Lefebvre, D. R., Takahashi, K. M., Muller, A. J., and Raju, V. R., "Degradation of epoxy coatings in humid environments: The critical relative humidity for adhesion loss", *Journal of Adhesion Science and Technology*, Vol. 5, No.3, 1991, pp. 201-227.
14. Bowditch, M. R., Hiscock, D., and Moth, D. A., "The relationship between hydrolytic stability of adhesive joints and equilibrium water content", *International Journal of Adhesion and Adhesives*, Vol. 11, No. 3, 1991, pp. 163-169.
15. Crank, J., *Mathematics of Diffusion*, Oxford University Press, 1975.
16. Brewis, D. M., Comyn, J., and Shalash, R. J. A., "The effect of moisture and temperature on the properties of an epoxide-polyamide adhesive in relation to its performance in single lap joints", *International Journal of Adhesion and Adhesives*, Vol. 2, 1982, pp. 215-222.
17. Hartshorn, S. R., Chapter 8, in *Structural Adhesives: Chemistry and Technology*, edited by Hartshorn, S. R., Plenum Press, New York, 1986.
18. Brewis, D. M., Chapter 5, in *Durability of Structural Adhesives*, edited by Kinloch, A. J., Applied Science Publishers, 1983.
19. Arrowsmith, D. J., and Maddison, A., "The use of perforated lap shear specimens to test the durability of adhesive-bonded aluminum", *International Journal of Adhesion and Adhesives*, Vol. 7, No. 1, January 1987, pp. 15-24.
20. Hand, H. M., Arah, C. O., McNamara, D. K., and Mecklenburg, M. F., "Effects of environmental exposure on adhesively bonded joints", *International Journal of Adhesion and Adhesives*, Vol. 11, No. 1, 1991, pp. 15-23.
21. Stevenson, A., and Priest, A. M., "Durability and life prediction of adhesive bonds in severe environments", *Rubber Chemistry and Technology*, Vol. 64, No. 4, 1991, pp. 545-

558.

22. Spinks, G. M., Isles, N. A., Egan, B. J., and Noakes, A., "Evaluation of adhesive joint performance in hostile environments", *Materials Forum*, Vol. 16, 1992, pp. 253-257.
23. Parker, B. M., "Environmental durability of aluminum joints with different pretreatments", *International Journal of Adhesion and Adhesives*, Vol. 13, No. 1, January 1993, pp. 47-51.
24. Chang, T., Sproat, E. A., Lai, Y-H., Shephard, N. E., and Dillard, D. A., "A test method for accelerated humidity conditioning and estimation of adhesive bond durability", *Journal of Adhesion*, Vol. 60, 1997, pp. 153-162.
25. Jackson, R. S., Kinloch, A. J., Gardhan, L. M., and Bowditch, M. R., "A study of the effects of water concentration on the stability of interfaces in adhesive joints", *Proceedings of the 19th Annual Meeting of the Adhesion Society*, Myrtle Beach, South Carolina, 1996, pp. 147-151.
26. Spies, G. J., "The peeling test on Redux-bonded joints", *Journal of Aircraft Engineering*, Vol. 25, 1953, pp. 64-70.
27. Bickerman, J. J., "Theory of peeling through a Hookean solid", *Journal of Applied Physics*, Vol. 28, No. 12, 1957, pp. 1484-1485.
28. Yurenka, S., "Peel testing of adhesive bonded metal", *Journal of Applied Polymer Science*, Vol. 7, 1962, pp. 136-144.
29. Gardon, J. L., "Peel adhesion II: A theoretical analysis", *Journal of Applied Polymer Science*, Vol. 7, 1963, pp. 643-664.
30. Kendall, K., "The shapes of peeling solid films", *Journal of Adhesion*, Vol. 5, 1973, pp. 105-117.
31. Gent, A. N., and Hamed, G. R., "Peel mechanics", *Journal of Adhesion*, Vol. 7, 1975, pp. 91-95.

32. Nicholson, D. W., "Peel mechanics with large bending", *International Journal of Fracture*, Vol. 13, 1977, pp. 279-287.
33. Bigwood, D. A., and Crocombe, A. D., "Elastic analysis and engineering design formulae for bonded joints", *International Journal of Adhesion and Adhesives*, Vol. 9, 1989, pp. 229-242.
34. Crocombe, A.D., and Adams, R. D., "Peel analysis using the finite-element method", *Journal of Adhesion*, Vol. 12, 1981, pp. 127-139.
35. Thouless, M. D., and Jensen, H. M., "Elastic fracture mechanics of the peel-test geometry", *Journal of Adhesion*, Vol. 38, 1992, pp. 185-197.
36. Gent, A. N., and Hamed, G. R., "Peel mechanics for an elastic-plastic adherend", *Journal of Applied Polymer Science*, Vol. 21, 1977, pp. 2817-2831.
37. Igarashi, T., "Peel strength and energy dissipation", in *Adhesive Joints: Formulation, Characteristics and Testing*, edited by Mittal, K. L., Plenum Press, New York, 1984, pp. 419-432.
38. Crocombe, A.D., and Adams, R. D., "An elasto-plastic investigation of the peel test", *Journal of Adhesion*, Vol. 13, 1982, pp. 241-267.
39. Kim, K-S., and Aravas, N., "Elasto-plastic analysis of the peel test", *International Journal of Solids and Structures*, Vol. 24, No. 4, pp. 417-435, 1988.
40. Kim, K.-S. and Kim, J., "Elasto-plastic analysis of the peel test for thin film adhesion", *Transactions of ASME, Journal of Engineering Materials and Technology*, Vol. 110, 1988, pp. 266-273.
41. Williams, J. G., "Root rotation and plastic work effects in the peel test", *Journal of Adhesion*, Vol. 41, 1993, pp. 225-239.
42. Kanninen, M. F., "An augmented double cantilever beam model for studying crack propagation and arrest", *International Journal of Fracture*, Vol. 9, No. 1, 1973, pp. 83-92.

43. Kinloch, A. J., Lau, C. C., and Williams, J. G., "The peeling of flexible laminates", *International Journal of Fracture*, Vol. 66, 1994, pp. 45-70.
44. Chang, F. H., Flynn, P. L., Gordon, D. E., and Bell, J. R., "Principles and application of ultrasonic spectroscopy in NDE of adhesive bonds", *IEEE Transactions on Sonics and Ultrasonics*, Vol. SU-23, No. 5, 1976, pp. 334-338.
45. Guyott, C. C. H., Cawley, P., and Adams, R. D., "The nondestructive testing of adhesively bonded structure: a review", *Journal of Adhesion*, Vol. 20, 1986, pp. 129-159.
46. Sinclair, A. N., Dickstein, P. A., Spelt, J. K., Segal, E., and Segal, Y., "Acoustic resonance methods for measuring dynamic elastic modulus of adhesive bonds", *Dynamic Elastic Modulus Measurements in Materials, ASTM STP 1045*, Edited by Wolfenden, A., America Society of Testing and Materials, Philadelphia, 1990, pp. 162-179.
47. Cawley, P., "Ultrasonic measurements for the quantitative NDE of adhesive joints - potential and challenges", *Proceedings of the IEEE Ultrasonics Symposium*, Tucson, AZ, October, 1992, pp. 767 - 772.
48. Guy, P., Jungman, A., Nayfeh, A. H., "Assessment of bond quality between metal components", *Review of Progress in Quantitative Nondestructive Evaluation*, edited by Thompson, D. O., and Chimenti, D. E., Vol. 11, Plenum Press, New York, 1991, pp. 1355-1361.
49. Dickstein, P. A., Spelt, J. K., and Sinclair, A. N., "Application of higher order crossing feature to nondestructive evaluation: A sample demonstration of sensitivity to the condition of adhesive joints", *Ultrasonics*, Vol. 29, September, 1991, pp. 355 - 365.
50. Thompson, R. B., and Thompson, D. O., "Past experience in the development of tests for adhesive bond strength", *Journal of Adhesion Science and Technology*, Vol. 5, No. 8, 1991, pp. 583 - 599.
51. Levesque, D., Legros, A., Michel, A., and Piche, L., "High resolution ultrasonic interferometry for quantitative nondestructive characterization of interfacial adhesion in multilayer (metal/polymer/metal) composites", *Journal of Adhesion Science and*

Technology, Vol. 7, No. 7, 1993, pp. 719 - 741.

52. Pilarski, A., "Ultrasonic evaluation of the adhesion degree in layered joints", *Materials Evaluation*, Vol. 43, May, 1985, pp. 765 - 770.

53. Nagy, P. B., Adler, L., "Interface characterization by true guided modes", *Review of Progress in Quantitative Nondestructive Evaluation*, edited by Thompson, D. O., and Chimenti, D. E., Vol. 10B, Plenum Press, New York, 1991, pp. 1295-1302.

54. Singher, L., Segal, Y., and Segal, E., "Considerations in bond strength evaluation by ultrasonic guided waves", *Journal of Acoustic Society of America*, Vol. 96, No. 4, October, 1994, pp. 2497 - 2505.

55. Wang, W., and Rokhlin, S. I., "Evaluation of interfacial properties in adhesive joints of aluminum alloys using angle-beam ultrasonic spectroscopy", *Journal of Adhesion Science and Technology*, Vol. 5, No. 8, 1991, pp. 647 - 666

56. Nagy, P. B., and Adler, L., "Nondestructive evaluation of adhesive joints by guided waves", *Journal of Applied Physics*, Vol. 66, No. 10, November, 1989, pp. 4658 - 4663.

57. Pilarski, A., Rose, J. L., and Balasubramaniam, K., "The angular and frequency characteristics of reflectivity from a solid layer embedded between two solids with imperfect boundary conditions", *Journal of Acoustic Society of America*, Vol. 87, No. 2, February, 1990, pp. 532 - 542.

58. Tattershall, H. G., "The ultrasonic pulse-echo technique applied to adhesion testing", *Journal of Physics D: Applied Physics*, Vol. 6, 1973, pp. 819 - 832.

59. Pilarski, A., and Rose, J. L., "A transverse-wave ultrasonic oblique-incidence technique for interfacial weakness detection in adhesive bonds", *Journal of Applied Physics*, Vol. 63, No. 2, January, 1988, pp. 300 - 307.

60. Jiao, D., and Rose, J. L., "An ultrasonic interface layer model for bond evaluation", *Journal of Adhesion Science and Technology*, Vol. 5, No. 8, 1991, pp. 631 - 646.

61. Pialucha, T., and Cawley, P., "An investigation of the accuracy of oblique incidence

ultrasonic reflection coefficient measurements”, *Journal of Acoustic Society of America*, Vol. 96, No. 3, September, 1994, pp. 1651 - 1660.

62. Lloyd, E. A., and Wadhwani, D. S., “Ultrasonic spectroscopy and the detection of hydrothermal degradation in adhesive bonds”, in *Ultrasonic Materials Characterization*, edited by Berger, H., and Linzer, M., 1980, pp. 395 - 406.

63. Dickstein, P. A., Spelt, J. K., Sinclair, A. N., and Bushlin, Y., “Investigation of nondestructive monitoring of the environmental degradation of structural adhesive joints”, *Materials Evaluation*, December, 1991, pp. 1498 - 1504.

64. Rokhlin, S. I., Lavrentyev, A. I., and Li, B., “Ultrasonic evaluation of environmental durability of adhesive joints”, *Research in Nondestructive Evaluation*, Vol. 5, 1993, pp. 95 - 109.

65. Lavrentyev, A. I., and Rokhlin, S. I., “Models for ultrasonic characterization of environmental interfacial degradation in adhesive joints”, *Review of Progress in Quantitative Nondestructive Evaluation*, edited by Thompson, D. O., and Chimenti, D. E., Vol. 13, Plenum Press, New York, 1994, pp. 1531-1538.

66. Lavrentyev, A. I., and Rokhlin, S. I., “Ultrasonic evaluation of environmental degradation of adhesive joints”, *Review of Progress in Quantitative Nondestructive Evaluation*, edited by Thompson, D. O., and Chimenti, D. E., Vol. 13, Plenum Press, New York, 1994, pp. 1539-1546.

67. Lowe, M. J. S., “Matrix techniques for modelling ultrasonic waves in multilayered media”, *IEEE Transactions on Ultrasonics, Ferroelectrics, and Frequency Control*, Vol. 42, No. 4, 1995, pp. 525-542.

68. Levesque, D. L., and Piche, L., “A robust transfer matrix formulation for the ultrasonic response of multi-layered absorbing media”, *Journal of Acoustic Society of America*, Vol. 92, No. 1, 1992, pp. 452 - 467.

69. Brekhoviskikh, L. M., and Godin, O. A., *Acoustics of Layered Media I*, Springer-Verlag, Berlin-Heidelberg, 1990.

70. Achenbach, J. D., *Wave Propagation in Elastic Solids*, North-Holland Publishing Company, 1975.
71. Goodman, J. W., *Fourier Optics*, McGraw-Hill Book Company, 1968.
72. Rokhlin, S. I., and Wang, Y. J., "Analysis of boundary conditions for elastic wave interaction with an interface between solids", *Journal of Acoustic Society of America*, Vol. 89, No. 2, February, 1991, pp. 503-515.
73. Wang, W., and Rokhlin, S. I., "Ultrasonic characterization of a thin layer of anodized porous aluminum oxide", *Review of Progress in Quantitative Nondestructive Evaluation*, edited by Thompson, D. O., and Chimenti, D. E., Vol. 9, Plenum Press, New York, 1990, pp. 1629 - 1636.
74. Cawley, P., and Pialucha, T., "The quantitative determination of the ultrasonic reflection coefficient from interlayers in adhesive joints", *Review of Progress in Quantitative Nondestructive Evaluation*, edited by Thompson, D. O., and Chimenti, D. E., Vol. 13, Plenum Press, New York, 1994, pp. 1523 - 1529.
75. Schoenberg, M., "Elastic wave behavior across linear slip interfaces", *Journal of Acoustic Society of America*, Vol. 68, No. 5, 1980, pp. 1516 - 1521.
76. Baik, J-M., Thompson, R. B., "Ultrasonic scattering from imperfect interfaces: A Quasi-Static Model", *Journal of Nondestructive Evaluation*, Vol. 4, Nos. 3/4, 1984, pp. 177 - 196.
77. Palmer, D. D., Rehbein, D. K., Smith, J. F., and Buck, O., "Nondestructive characterization of the mechanical strength of diffusion bonds. II. Application of a quasi-static spring model", *Journal of Nondestructive Evaluation*, Vol. 7, Nos. 3/4, 1988, pp. 167 - 174.
78. Margetan, F. J., Thompson, R. B., and Gray, T. A., "Interfacial spring model for ultrasonic interactions with imperfect interfaces: Theory of oblique incidence and application to diffusion-bonded butt joints", *Journal of Nondestructive Evaluation*, Vol. 7, Nos. 3/4, 1988, pp. 131 - 152.

79. Moidu, A. K., Sinclair, A. N., and Spelt, J. K., "Analysis of the peel test: Prediction of adherend plastic dissipation and extraction of fracture energy in metal-to-metal adhesive joints", *Journal of Testing and Evaluation*, Vol. 23, No. 4, July, 1995, pp. 241 - 253.
80. Moidu, A. K., Sinclair, A. N., and Spelt, J. K., "On the determination of fracture energy using the peel test", Accepted, *Journal of Testing and Evaluation*.
81. Hodge, P. G., *Plastic Loading of Structures*, McGraw-Hill, 1957.
82. Penado, F. E., "A closed form solution for the energy release rate of the double cantilever beam specimen with an adhesive layer", *Journal of Composite Material*, Vol. 27, No. 4, 1993, pp. 383 - 407.
83. Fernlund, G., and Spelt, J. K., "Mixed mode energy release rates for adhesively bonded beam specimens", *Journal of Composites Technology and Research*, Vol. 16, No. 3, 1994, pp. 234 - 243.
84. Ugural, A. C., and Fenster, S. K., *Advanced Strength and Applied Elasticity*, PTR Prentice Hall, Englewood Cliffs, New Jersey, 1995.
85. Gent, A. N., and Kaang, S. Y., "Effect of peel angle upon peel force", *Journal of Adhesion*, Vol. 24, 1987, pp. 173 - 181.
86. Moidu, A. K., Sinclair, A. N., and Spelt, J. K., "Use of focused ultrasonic beams to characterize the interfacial region in bonded joints", *Proceedings of the IEEE Ultrasonics Symposium*, Seattle, Washington, November, 1995, pp. 775 - 778.
87. Moidu, A. K., Sinclair, A. N., and Spelt, J. K., "A new ultrasonic method for the interfacial characterization of adhesive joints", *Proceedings of the IEEE Ultrasonics Symposium*, San Antonio, Texas, November, 1996.
88. Tsukahara, Y., Nakaso, N., and Ohira, K., "Angular spectral approach to reflection of focused beams with oblique incidence in spherical-planar-pair lenses", *IEEE Transactions on Ultrasonics, Ferroelectrics, and Frequency Control*, Vol. 38, No. 5, September, 1991, pp. 468 - 480.

89. Krautkraemer, J., and Krautkraemer, H., *Ultrasonic Testing of Materials*, Springer-Verlag, New York, 1990.
90. Papadakis, E. P., Chapter 3, in *Physical Acoustics*, edited by Thurston, R. N., and Pierce, A. D., Academic Press, Inc., 1990.
91. Wang, T. T., Herbert, J. M., and Glass, A. M., *Applications of Ferroelectric Polymers*, Chapman-Hall, New York, 1988.
92. AMP Inc., *Piezo-film Technical Manual*, 1993.
93. Moidu, A. K., Sinclair, A. N., and Spelt, J. K., "Adhesive joint durability assessed using open-faced peel specimens", Accepted, *Journal of Adhesion*.

Governing Equations for the Attached Adherend

By applying the equilibrium equations [84] to the free-body diagram shown in Fig. A.1, the following equations may be obtained:

$$\frac{dV}{dx} = \sigma_{yy} \quad (\text{A.1})$$

$$\frac{dT}{dx} = \tau_{xy} \quad (\text{A.2})$$

$$\frac{dM}{dx} = \tau_{xy}h/2 - V \quad (\text{A.3})$$

where V is the shear force, T is the axial force, M is the bending moment, h is the adherend thickness, and σ_{yy} and τ_{xy} are the foundation normal and shear stresses, respectively.

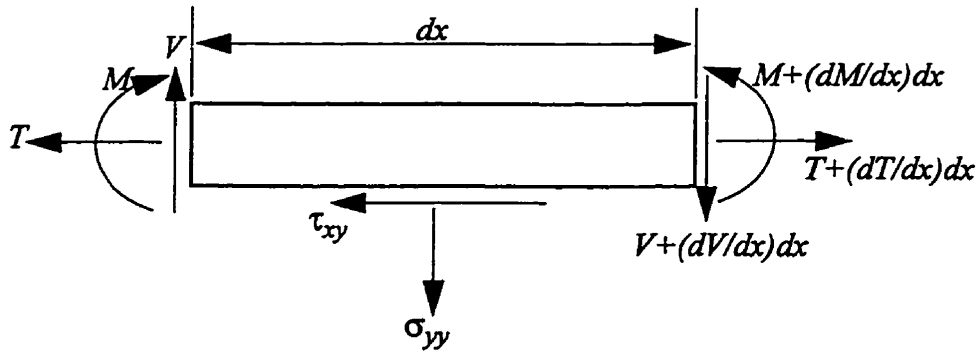


Figure A.1 Free body diagram of a differential element on the attached part of the flexible adherend

According to the theory of beam on elastic foundation, the foundation stresses and displacements may be related as (Section 3.5):

$$\sigma_{yy} = \lambda_{\sigma} v \quad (\text{A.4})$$

$$\tau_{xy} = \lambda_{\tau} u \quad (\text{A.5})$$

Assuming that the displacements are small for the attached part of the adherend, the following equation relates the curvature, K , and the vertical deflection, v :

$$K = \frac{d^2 v}{dx^2} \quad (\text{A.6})$$

The approximate M-K relation for the attached part is given by (Section 3.5):

$$M = M_1 + \frac{\zeta M_p}{K_e} (K - K_1) \quad (\text{A.7})$$

The axial strain at the interface between the adhesive and the adherend is given by:

$$\frac{du}{dx} = Kh/2 + \frac{T}{Eh} \quad (\text{A.8})$$

Combining Eqs A2 - A.8, the following equation may be derived relating the foundation normal and shear stresses:

$$\sigma_{yy} = \frac{Q_1 d\tau_{xy}}{Q_2 dx} - \frac{1}{Q_2} \frac{d^3 \tau_{xy}}{dx^3} \quad (\text{A.9})$$

where

$$Q_1 = \frac{\lambda_{\tau}}{Eh} \left(1 + \frac{2}{\zeta} \right); \quad Q_2 = \frac{4\lambda_{\tau}}{\zeta Eh^2} \quad (\text{A.10})$$

From Eqs. A.1, A.3, A.4, A.6 and A.7, the following expression may be obtained:

$$\frac{d^4 \sigma_{yy}}{dx^4} + Q_3 \sigma_{yy} = Q_4 \frac{d\tau_{xy}}{dx} \quad (\text{A.11})$$

where

$$Q_3 = \frac{8\lambda_\sigma}{\zeta E h^3}; \quad Q_4 = \frac{4\lambda_\sigma}{\zeta E h^2} \quad (\text{A.12})$$

Combining Eq. A.9 and A.10, we get the following equation governing the foundation shear stress:

$$\frac{d^7 \tau_{xy}}{dx^7} - Q_1 \frac{d^5 \tau_{xy}}{dx^5} + Q_3 \frac{d^3 \tau_{xy}}{dx^3} - Q_5 \frac{d\tau_{xy}}{dx} = 0 \quad (\text{A.13})$$

where $Q_5 = Q_1 Q_3 - Q_2 Q_4$. The foundation normal stress may be found from Eq. A.9.

Oblique Reflection and Transmission Coefficients

B.1 Reflection and transmission coefficients of the interfacial region

In this section expressions are derived for the oblique reflection coefficients from an adhesive/adherend interfacial region using the wave potential theory (Section 2.4.1) and the spring boundary conditions. Considering obliquely incident shear waves (Fig. B.1), the following expressions may be derived for the wave potentials in the top and bottom half spaces [69]:

$$\phi_1 = R_{sl} e^{i(\xi x - \alpha_1 z - \omega t)}, \quad \psi_1 = [e^{i\beta_1 z} + R_{ss} e^{-i\beta_1 z}] e^{i(\xi x - \omega t)} \quad (\text{B.1})$$

$$\phi_2 = D_{sl} e^{i(\xi x + \alpha_2 z - \omega t)}, \quad \psi_2 = D_{ss} e^{i(\xi x + \beta_2 z - \omega t)} \quad (\text{B.2})$$

where ϕ and ψ are the wave potentials, R_{sl} is the shear-longitudinal reflection coefficient, R_{ss} is the shear-shear reflection coefficient, D_{sl} is the shear-longitudinal transmission coefficient, D_{ss} is the shear-shear transmission coefficient, ξ is the horizontal wave number, ω is the circular frequency, and α and β are the vertical wave numbers of longitudinal and shear waves respectively, given by:

$$\alpha = \sqrt{k_l^2 - \xi^2}, \quad \beta = \sqrt{k_s^2 - \xi^2} \quad (\text{B.3})$$

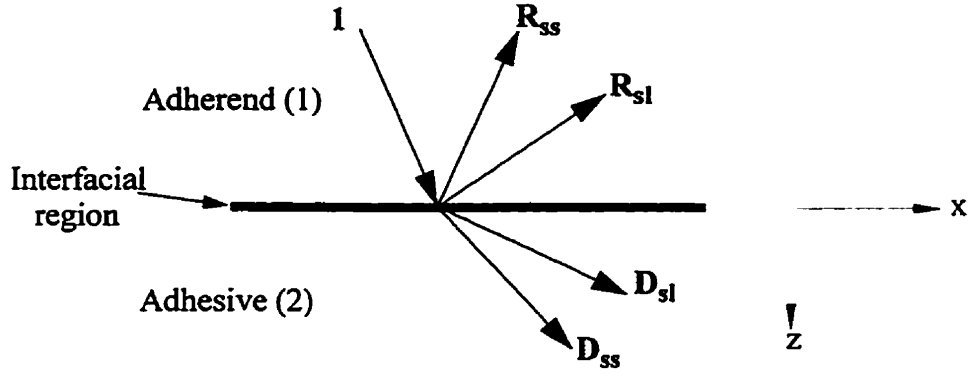


Figure B.2: Schematic of oblique-incidence shear wave reflection from the interfacial region.

where $k_l = \omega/c_l$ and $k_s = \omega/c_s$ are the longitudinal and shear wave numbers respectively, c_l and c_s being the longitudinal and shear wave velocities. In the above equations, subscripts '1' and '2' denote the top and bottom half spaces, respectively (Fig. B.1).

The following expressions may be derived for the displacements and stresses in terms of the wave potentials, ϕ and ψ_y [69]:

$$u = i\xi\phi - \frac{\partial\psi_y}{\partial z}, \quad w = \frac{\partial\phi}{\partial z} + i\xi\psi_y \quad (\text{B.4})$$

$$\sigma_{xz} = -2\mu\xi\left[\chi\psi_y - i\frac{\partial\phi}{\partial z}\right], \quad \sigma_{zz} = 2\mu\xi\left[\chi\phi + i\frac{\partial\psi_y}{\partial z}\right] \quad (\text{B.5})$$

where u and σ_{xz} are the tangential displacement and stress respectively, w and σ_{zz} are the normal displacement and stress respectively, μ is the modulus of rigidity, and χ is given by:

$$\chi = \xi - \frac{k_s^2}{2\xi} \quad (\text{B.6})$$

The four boundary conditions are, using the spring model:

$$(\tau_{xz})_1 = (\tau_{xz})_2, \quad (\sigma_{zz})_1 = (\sigma_{zz})_2 \quad (B.7)$$

$$(\sigma_{xz})_2 = K_t(u_2 - u_1), \quad (\sigma_{zz})_2 = K_n(w_2 - w_1) \quad (B.8)$$

By combining Eqs. B.1, B.3 and B.5, and rearranging the terms, the following matrix relation may be obtained for the reflection and transmission coefficients for incident shear waves:

$$\begin{bmatrix} \mu_1 \chi_1 & -\mu_1 \alpha_1 & -\mu_2 \chi_2 & -\mu_2 \alpha_2 \\ \mu_1 \beta_1 & \mu_1 \chi_1 & \mu_2 \beta_2 & -\mu_2 \chi_2 \\ \beta_1 & \xi & \left(\beta_2 + \frac{2i\mu_2 \chi_2 \xi}{K_t} \right) & \left(-\xi + \frac{2i\mu_2 \alpha_2 \xi}{K_t} \right) \\ \xi & -\alpha_1 & \left(-\xi + \frac{2i\mu_2 \beta_2 \xi}{K_n} \right) & \left(-\alpha_2 - \frac{2i\mu_2 \chi_2 \xi}{K_n} \right) \end{bmatrix} \begin{bmatrix} R_{ss} \\ R_{sl} \\ D_{ss} \\ D_{sl} \end{bmatrix} = \begin{bmatrix} -\mu_1 \chi_1 \\ \mu_1 \beta_1 \\ \beta_1 \\ -\xi \end{bmatrix} \quad (B.9)$$

For incident longitudinal wave, the following matrix equation may be derived in a similar manner:

$$\begin{bmatrix} \mu_1 \chi_1 & -\mu_1 \alpha_1 & -\mu_2 \chi_2 & -\mu_2 \alpha_2 \\ \mu_1 \beta_1 & \mu_1 \chi_1 & \mu_2 \beta_2 & -\mu_2 \chi_2 \\ \beta_1 & \xi & \left(\beta_2 + \frac{2i\mu_2 \chi_2 \xi}{K_t} \right) & \left(-\xi + \frac{2i\mu_2 \alpha_2 \xi}{K_t} \right) \\ \xi & -\alpha_1 & \left(-\xi + \frac{2i\mu_2 \beta_2 \xi}{K_n} \right) & \left(-\alpha_2 - \frac{2i\mu_2 \chi_2 \xi}{K_n} \right) \end{bmatrix} \begin{bmatrix} R_{ls} \\ R_{ll} \\ D_{ls} \\ D_{ll} \end{bmatrix} = \begin{bmatrix} -\mu_1 \alpha_1 \\ -\mu_1 \chi_1 \\ -\xi \\ -\alpha_1 \end{bmatrix} \quad (B.10)$$

B.2 Transmission coefficients at the front-wall

The new formulation for the angular spectrum model requires the transmission coefficients at the water/aluminum and aluminum/water interfaces. For the water/aluminum interface the following expressions for the longitudinal-longitudinal (T_{ll}) and longitudinal-shear (T_{ls}) transmission coefficients may be derived by using the above wave-potential approach:

$$T_{ll} = \frac{-2\rho_w \omega^2 \alpha_w \chi_l}{2\mu_l \xi \alpha_w [\chi_l^2 + \alpha_l \beta_l] + \alpha_l \rho_w \omega^2 (\xi - \chi_l)} \quad (\text{B.11})$$

$$T_{ls} = \frac{2\rho_w \omega^2 \alpha_w \alpha_l}{2\mu_l \xi \alpha_w [\chi_l^2 + \alpha_l \beta_l] + \alpha_l \rho_w \omega^2 (\xi - \chi_l)} \quad (\text{B.12})$$

where ρ_w is the water density and α_w is the vertical wave number in water.

For the aluminum/water interface the following expressions may be derived for the transmission coefficients of incident longitudinal and shear waves:

$$T_{ll}' = \frac{4\mu_l \alpha_l \chi_l \xi (\chi_l - \xi)}{2\mu_l \xi \alpha_w [\chi_l^2 + \alpha_l \beta_l] + \alpha_l \rho_w \omega^2 (\xi - \chi_l)} \quad (\text{B.13})$$

$$T_{sl}' = \frac{4\mu_l \alpha_l \beta_l \xi (\chi_l - \xi)}{2\mu_l \xi \alpha_w [\chi_l^2 + \alpha_l \beta_l] + \alpha_l \rho_w \omega^2 (\xi - \chi_l)} \quad (\text{B.14})$$

Water Diffusion Equations

This appendix deals with the diffusion equations used for predicting water diffusion into cast adhesive films and the open-faced specimens. Consider the cast adhesive sheet of Fig. C.1a. The water diffusion is governed by the one-dimensional form of Fick's second law given by [15]:

$$\frac{\partial C}{\partial t} = D \frac{\partial^2 C}{\partial z^2} \quad (\text{C.1})$$

where C is the concentration of water and D is the diffusion coefficient. The above equation may be readily solved for a plane sheet with zero initial concentration and equal surface concentrations of C_0 on both faces. The solution is given by [15]:

$$\frac{C}{C_0} = 1 - \frac{4}{\pi} \sum_{n=0}^{\infty} \frac{(-1)^n}{2n+1} \exp \left[\frac{-D (2n+1)^2 \pi^2 t}{h^2} \right] \cos \left[\frac{(2n+1) \pi z}{h} \right] \quad (\text{C.2})$$

If M_t denotes the total amount of water which has entered the sheet at time t and M_{∞} the corresponding quantity after infinite time (i.e. equilibrium water content), then the following expression for the fractional mass uptake by the sheet may be derived from Eq. C.2:

$$\frac{M_t}{M_{\infty}} = 1 - \sum_{n=0}^{\infty} \frac{8}{(2n+1)^2 \pi^2} \exp \left[\frac{-D (2n+1)^2 \pi^2 t}{h^2} \right] \quad (\text{C.3})$$

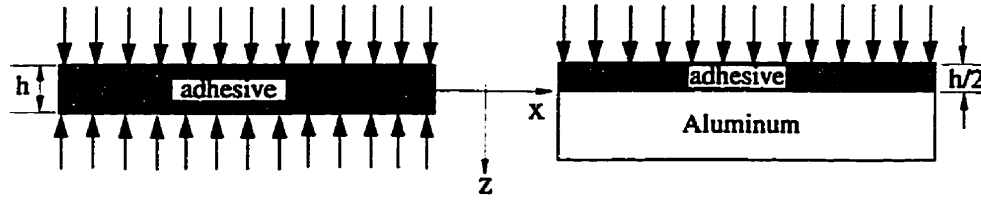


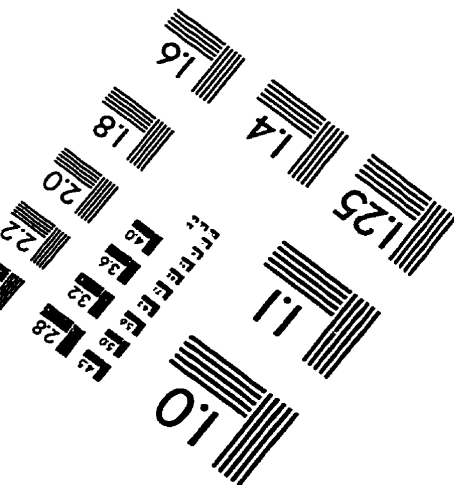
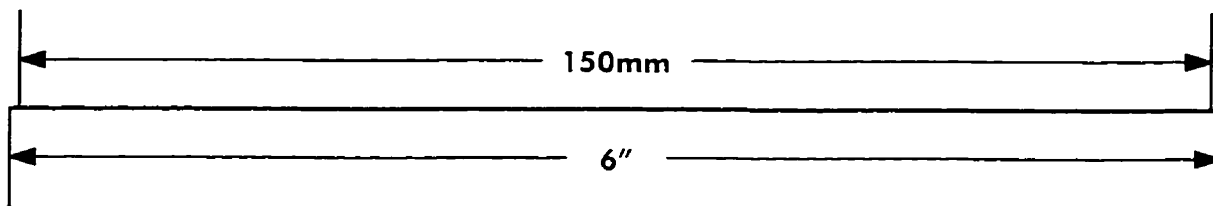
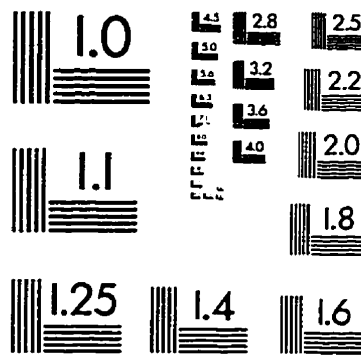
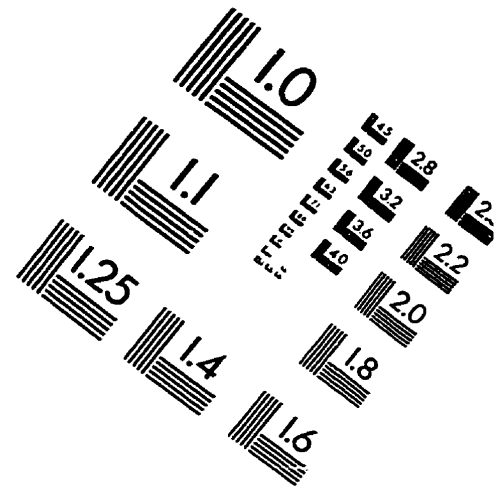
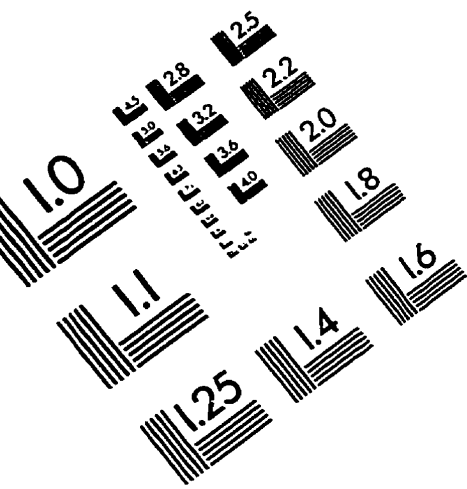
Figure C.3: Schematic of water diffusion into, (a) cast adhesive sample, (b) open-faced specimen.

For small values of time t , the above may be approximated by:

$$\frac{M_t}{M_\infty} = \frac{8}{h} \sqrt{\frac{Dt}{\pi}} \quad (\text{C.4})$$

It should be noted that diffusion into an open-faced geometry (Fig. C.1b) of a given adhesive thickness is equivalent to diffusion into a cast adhesive sheet of twice the thickness. This can be seen by noting that in Fig. C.1b, the interface between the adhesive and the adherend is impermeable and the concentration gradient is zero. This condition holds at the central plane of a cast sheet provided that the initial and boundary conditions are symmetrical about that plane. It follows therefore, that the solutions for the plane sheet occupying the region $-h/2 < z < h/2$ also apply to the sheet $0 < z < h/2$ when the face $z = 0$ is impermeable. Therefore, to predict water diffusion into an open-faced joint with an adhesive thickness h , Eqs. C.2-C.4 may be used by replacing h with $2h$. From Eq. C.4, it may be readily seen that the saturation time of an open-faced joint is approximately four times that of a cast sheet with the same adhesive thickness.

IMAGE EVALUATION TEST TARGET (QA-3)



APPLIED IMAGE, Inc.
1653 East Main Street
Rochester, NY 14609 USA
Phone: 716/482-0300
Fax: 716/288-5989

© 1993, Applied Image, Inc., All Rights Reserved

